Neutron-Proton Interactions in Heavy Self-Conjugate Nuclei

Adam Benjamin Garnsworthy

Department of Physics,
School of Electronics and Physical Sciences,
University of Surrey
Guildford, Surrey, GU2 7XH

Submitted for the degree of Doctor of Philosophy

September 2007

Abstract

Neutron-deficient nuclei along the proton drip line in the mass region 80-90 have been populated in relativistic projectile fragmentation reactions at GSI, Germany. A 750 MeV per nucleon beam of $^{107}_{47}\mathrm{Ag}_{60}$ provided by the SIS-18 synchrotron was fragmented on a 4 g/cm^2 target of beryllium. The reaction products were separated and unambiguously identified using the FRagment Separator (FRS) with its ancillary detectors. The ions produced were slowed down by means of a variable thickness aluminium degrader and implanted in a 7 mm multilayer perspex block located at the centre of the high-efficiency Stopped RISING array. Gamma rays emitted from the decay of nano-to-millisecond isomeric states were detected in the array and correlated with the arrival of the associated ion. This allowed the observation of previously unreported excited states in the odd-odd $N = Z$ nuclei, $^{82}_{41}\mathrm{Nb}_{41}$ and $^{86}_{43}\mathrm{Tc}_{43}$. The new data suggest the low-lying structures of these proton drip line nuclei are dominated by a $T = 1$, np pairing condensate. Experimental results are compared to theoretical interpretations from TRS calculations and the Projected Shell Model. The isomeric state in ^{82}Nb is interpreted as an isospin-changing K isomer with a reduced hindrance of $f_\nu \approx 18$. This is the first case of such an isomeric state along the $N = Z$ line and indeed in this mass region. Previously unreported isomeric states have been identified in ^{87,88}Tc and ^{84}Nb. Isomeric ratios which provide insight into the reaction mechanism and nuclear structure are calculated for all the isomers observed, including the previously identified isomeric states in ^{94,96}Pd, ^{93}Ru and ^{84}Nb.

Treading the boards and walking the roads,
Watching my feet but stepping on toes,
Study your smile, count your tears,
Haven't felt this alive in years ...

Penfold Gate - Alive In Years

Acknowledgements

In the acknowledgements of my PhD thesis the most important person to thank has to be my supervisor Paddy Regan. A fantastic supervisor. From our first meeting he has been a vital source of knowledge, advice and guidance in every aspect of this undertaking. In addition to this he has provided me with wonderful opportunities to travel so often, meet so many new people and get a feel for what nuclear physics is really all about in a very fun and exciting environment. Above all he has been a good friend who I hope to know for many years to come. Paddy's sheer audacity and lust for life is a true inspiration to us all.

Without Nick Thompson I am not sure I could have made it through these last three years. He has been a steady constant in my life, never too far away. There have been some really great times, with a perpetual flow of the somewhat bizarre that Nick does so well. But in the less enjoyable times the fact that there were two of us is what has got us through. I am very grateful that we had the chance to do our PhDs together.

I must thank everyone at Surrey for making the department such a great place to work. Everyone is always helpful and competent, friendly and fun. A few people I have worked closely with deserve a specific mention. Phil Walker has been a great second supervisor. Phil has always provided me with a useful grounding with his calming and thoughtful perspective on things. I have learnt a lot from Phil and have enjoyed our many discussions which have always been enlightening. I would like to thank Gareth Jones, Steven Steer and Scott Williams. They have been a vital part of the time spent doing my PhD. I appreciate and admire their professionalism at work and their ability to have fun. We have had many highly enjoyable nights out and trips away from which I have great memories. I would like to thank Bill Gelletly for taking the time to provide me with very useful advice and guidance.

I was privileged to have the opportunity to spend a year of my studies at Yale University working in the Wright Nuclear Structure laboratory. I am very grateful to Professor Rick Casten for this wonderful chance to live in another country and learn such a huge amount from being part of the lab. I am also indebted to Andreas Heinz whose personal experience of working at both Argonne and GSI was an essential part of my early learnings.

My PhD was in part sponsored by Nexia Solutions Ltd, a subsiduary of BNFL.

I would like to acknowledge and thank both the EPSRC and Nexia Solutions Ltd for the financial support provided during my studies.

I could not ask for better parents. The enormous amount of love and support they give me is amazing. I am so grateful to them for everything and I hope I continue to make them proud. Thank you to my wonderful sister for some great times during my PhD, partying in London and hanging out in New York.

Finally I would like to thank my closest friends. My friends are the people who are most important to me. Peter Smith, Stephen Smith, Gemma Wright, Laura Clarke, John Foulkes-Williams, Alexandra Sheffield, Laura Gulliver, Peter Flood, Chris Smith, Robbie Jones, Adam Murray, Alan Foulkes-Williams, Jon Jarram and certainly not least Phil Smith, Namrata Singh and Dan Southwell. These are the people I love the most and who have been the most important people throughout everything I have done. Without them I would not be so happy and would not have achieved so much. Thank you for being there for me, helping me to keep my sanity and for showing me the true meaning of friendship.

Contents

List of Figures **iv**

List of Tables **viii**

1 Introduction **1**

1.1 Isospin, Pairing and $N = Z$ Nuclei 2

1.2 Isomeric States 6

1.3 The Neutron-Deficient $N \approx Z \sim 40$ Nuclides 7

2 Theory **12**

2.1 Radioactive Decay 12

2.1.1 Lifetimes of Nuclear States 12

2.1.2 Beta Decay 13

2.1.3 Gamma Decay 14

2.1.4 Internal Conversion 17

2.1.5 Proton Decay 19

2.2 Theoretical Nuclear Models and Calculations 20

2.3 The Independent Single-Particle Model 20

2.4 The Shell Model 23

2.4.1 The Coupling of Angular Momenta 23

2.4.2 The Pairing Interaction 24

2.4.3 The δ Interaction 24

2.4.4 Two-State Mixing 25

2.5 Deformation and Nuclear Shapes 27

2.5.1 Angular Momentum Quantum Numbers 28

2.6 The Nilsson Model 29

2.7 BCS Calculations . . . 32
2.7.1 Projected Shell Model . . . 32
2.7.2 Potential-Energy-Surface Calculations . . . 34
2.8 Isomeric Nuclear States . . . 35
2.8.1 The Seniority Scheme . . . 35
2.8.2 Shape Isomers . . . 36
2.8.3 Spin Traps . . . 36
2.8.4 K Isomers . . . 36

3 Experimental Techniques 38
3.1 Nuclear Reaction Mechanisms . . . 38
3.1.1 Experimental Access to N=Z Nuclei . . . 39
3.1.2 Projectile Fragmentation Reactions . . . 40
3.2 RISING at GSI . . . 43
3.3 The GSI Accelerator System . . . 43
3.4 The FRagment Separator . . . 44
3.4.1 Beam line Detectors of the FRS . . . 45
3.5 Gamma-ray Spectroscopy . . . 50
3.5.1 Germanium Detectors . . . 50
3.5.2 Gamma-ray Interactions in Ge . . . 52
3.5.3 The Stopped RISING Array . . . 55

4 Data Analysis 60
4.1 Experimental Details . . . 60
4.2 Improving the Cleanliness of the Particle Identification . . . 61
4.2.1 MultiWire Proportional Counters . . . 63
4.2.2 Scintillator 21 Charge Collection . . . 64
4.2.3 Energy Loss in the Degrader . . . 65
4.3 Z vs A/q Identification Plot . . . 67
4.4 LISE++ Simulations . . . 67
4.5 Identification of Isomeric States . . . 70
4.6 Previously Reported Isomeric States . . . 72
4.7 Reducing Background in Gamma-ray Spectra . . . 74
4.7.1 Nuclear Reactions Before the Stopper . . . 74

4.7.2 Scintillator 43 - Veto Detector 75
4.7.3 Germanium Signal Fold 76
4.7.4 Addback for the RISING Stopped-Beam Array 79

5 Results and Discussion **84**
5.1 Previously Unobserved States in ^{82}Nb 84
5.2 Isomeric States in ^{84}Nb 89
5.3 Results for ^{86}Tc 97
5.4 Results for ^{87}Tc 102
5.5 Results for ^{88}Tc 106
5.6 Hindered E1 Transitions in the $A \sim$80 Region 109
5.7 Neutron-Proton Interactions 109
5.8 Determination of Isomeric Ratios 113

6 Conclusions **116**

A Calculation of Internal Conversion Coefficients **117**

B Publications **120**
B.1 First Author Peer-Reviewed Publications 120
B.2 Other Publications in Peer-Reviewed Journals 120
B.3 Other Publications 122

Bibliography **123**

List of Figures

1.1 The chart of the nuclides showing nuclear half-lives 3
1.2 Allowed intrinsic angular momentum couplings of the A=2 isobaric triplet 4
1.3 The $A = 14$ isobaric triplet 5
1.4 Energy difference between the lowest observed $T = 0$ and $T = 1$ states in odd-odd $N = Z$ nuclei 6
1.5 Part of the chart of the nuclides showing the stable isotopes and location of the proton drip line for elements between $_{28}$Ni and $_{50}$Sn and $N \leq 62$ 8
1.6 Atomic masses of the $A = 82$ and $A = 86$ isobars 9
1.7 Calculated ground-state deformations of nuclei in the fpg shell 10
1.8 Previous evidence for the isomeric state in ^{86}Tc 11

2.1 Weisskopf estimates for decay half-lives of transitions in ^{86}Tc 17
2.2 Total internal conversion coefficients for transitions in Tc 19
2.3 Single-particle energy levels in the shell model from different potentials 22
2.4 Effect of the pairing and δ residual interactions 25
2.5 Schematic representation of axially symmetric nuclear shapes 27
2.6 Schematic representation of the quantum numbers associated with an axially symmetric deformed nucleus 29
2.7 The angular splitting of a $g_{9/2}$ state into its individual magnetic substates in a deformed potential 30
2.8 Nilsson diagram for protons or neutrons, Z, $N \leq 50$ ($\epsilon_4 = 0$) 31

3.1 Schematic view of the projectile fragmentation reaction process 41
3.2 Cross sections of the Pd, Rh, Ru, Tc, Mo and Nb isotopes predicted by the EPAX program for a ^{107}Ag primary beam 42
3.3 Schematic outline of the FRagment Separator (FRS) at GSI 45

3.4 Schematic showing the relative positions of the beam line detectors located at the final focal plane of the FRS (S4). 46
3.5 Schematic outline of a MultiWire Proportional Counter (MWPC) . . . 48
3.6 Schematic outline of a MUltiple-Sampling Ionization Chamber (MUSIC) 49
3.7 The changing dominance of the main interaction processes of gamma rays in matter as a function of gamma-ray energy and atomic number, Z 53
3.8 Photograph of the Stopped RISING array coupled to the RISING beam line at the focal plane of the FRS. 56
3.9 Photograph of one hemisphere of the Stopped RISING array. 57
3.10 Photograph of the Stopped RISING array with a source at the centre. . 57
3.11 Photograph of the Stopped RISING array with the 7 mm perspex stopper mounted in the centre 58
3.12 The gamma-ray photopeak efficiency response of the Stopped RISING array determined using ^{133}Ba and ^{60}Co source data 59

4.1 Chart of the nuclides indicating the regions of nuclei populated and transmitted to the FRS focal plane in the ^{96}Pd and ^{86}Tc settings. . . . 62
4.2 Chart of the nuclides indicating the regions of nuclei populated and transmitted to the FRS focal plane in the ^{90}Rh and ^{82}Nb settings. . . . 62
4.3 Plot of the sum of the charges collected in the left and right photomultiplier tubes of MW41 63
4.4 Charge vs position plots for the left photomultipler tube of Sci21 64
4.5 Charge vs position plots for the right photomultipler tube of Sci21 . . . 65
4.6 Effect of Sci21 gating on the Z vs ToF plot 66
4.7 Effect of Sci21 gating on the S2 position vs ToF plot 66
4.8 Final, calibrated Z vs A/q identification plot for the combined ^{90}Rh, ^{86}Tc and ^{82}Nb settings. 67
4.9 Simulated and experimental Z vs A/q plot for the ^{96}Pd setting 68
4.10 Simulated and experimental Z vs A/q plot for the ^{90}Rh setting 68
4.11 Simulated and experimental Z vs A/q plot for the ^{86}Tc setting 69
4.12 Simulated and experimental Z vs A/q plot for the ^{82}Nb setting 69
4.13 Particle ID projections gated on delayed gamma rays with various time conditions 70

4.14 Energy vs DGF time matrices and Ge energy and time projections to show the effect of ion species selection, time and background reduction gating techniques 71
4.15 Gamma-ray and DGF time spectra of delayed events associated with ions identified as ^{96}Pd and ^{94}Pd 73
4.16 Gamma-ray and DGF time spectrum of delayed events associated with ions identified as ^{93}Ru 74
4.17 Energy loss in MUSIC 41 plotted against the energy loss in MUSIC 42 75
4.18 Energy loss in Sci42 plotted against the energy loss in MUSIC 41 . . . 76
4.19 Energy loss in Scintillator 43 77
4.20 Comparison of the Ge fold with different timing gates 78
4.21 Hit patterns produced for crystal 11 using ^{60}Co source data 80
4.22 The numbering of the crystals in the RISING Stopped Array. 80
4.23 Effect of addback on gamma-ray spectra of ^{60}Co and ^{152}Eu source data 82

5.1 Energy vs DGF time plot gated on ions identified as ^{82}Nb 85
5.2 Gamma-ray spectrum gated on ions identified as ^{82}Nb 85
5.3 Coincidence gamma-ray spectrum gated on ions identified as ^{82}Nb . . . 86
5.4 Experimental and theoretical level schemes of ^{82}Nb 87
5.5 TRS calculation for the ground state and an excited state of ^{82}Nb . . . 88
5.6 Level scheme for ^{84}Nb reported by Mărginean *et al.* 90
5.7 Energy vs DGF time plot gated on ions identified as ^{84}Nb 90
5.8 Singles and coincidence gamma-ray spectra of ions identified as ^{84}Nb . 91
5.9 Proposed level scheme for ^{84}Nb observed in the current work 93
5.10 Mean lifetime fits to the gamma rays associated with the decay of the isomeric states in ^{84}Nb. The decay from the 47 keV isomeric state has been fitted using a two-component least-squares fit due to feeding from the 109 (5) ns isomeric state. 93
5.11 Time difference spectra between the 65 and 140 keV transitions (Upper panel) and the 47 and 114 keV transitions (Lower panel) in ^{84}Nb 96
5.12 Energy vs DGF time plot gated on ions identified as ^{86}Tc 97
5.13 Singles and coincidence gamma-ray spectra gated on ions identified as ^{86}Tc 98

5.14 DGF-timing spectrum with energy gates on the 593 and 849 keV gamma rays in the isomeric decay of ^{86}Tc. 99
5.15 Experimental and theoretical level schemes for ^{86}Tc 101
5.16 TRS calculation for the ground state and an excited state of ^{86}Tc . . . 102
5.17 Energy vs DGF time plot gated on ions identified as ^{87}Tc 103
5.18 Gamma-ray spectrum gated on ions identified as ^{87}Tc 103
5.19 Mean lifetime fits on the individual gamma rays observed in the decay of an isomeric state in ^{87}Tc and on the sum of the two. 104
5.20 Energy vs DGF time plot gated on ions identified as ^{88}Tc 106
5.21 Gamma-ray and DGF time spectrum for ^{88}Tc 107
5.22 Strengths of E1 transitions in the fpg shell 108
5.23 Structural evolution of the $N = Z$ nuclei across the fpg shell 110
5.24 Energy difference between the lowest observed $T = 0$ and $T = 1$ states in odd-odd $N = Z$ nuclei plotted against mass number 111
5.25 Energy difference between the lowest observed $T = 0$ and $T = 1$ states in odd-odd $N = Z$ nuclei plotted against valence product 111
5.26 Experimentally identified energy levels below 1 MeV in the $T_z = 0, 1$ and 2 isotopes of Y, Nb, Tc and Rh. 112

List of Tables

2.1 Beta decay selection rules 15

3.1 Cross sections predicted by EPAX for the fragmentation of a ^{107}Ag primary beam for nuclei of interest to this thesis 42

4.1 Spill structures of the various FRS settings. 61
4.2 Magnetic field settings of the Dipole magnets of the FRS used in the different settings of the experiment. 61
4.3 The effect of addback routines on the peak to total ratio of the 1173 and 1332 keV gamma rays emitted from a ^{60}Co source. 83
4.4 The effect of addback routines on the peak to total ratios of gamma rays emitted from a ^{152}Eu source. 83

5.1 Partial half-lives and calculated total conversion coefficients of transitions in ^{82}Nb 88
5.2 Calculated partial half-lives of transitions in ^{84}Nb 94
5.3 Calculated total conversion coefficients for transitions observed in ^{84}Nb 95
5.4 Calculated partial half-lives of transitions in ^{86}Tc 100
5.5 Calculated total conversion coefficients for transitions observed in ^{86}Tc 100
5.6 Calculated partial half-lives for transitions in ^{87,88}Tc 105
5.7 Calculated total conversion coefficients for transitions in ^{87,88}Tc. 105
5.8 Summary of E1 transitions identified in the current work 107
5.9 Isomeric ratios measured in the current experiment 115

A.1 Gamma-ray intensities observed in the decay of ^{82}Nb. 118
A.2 Gamma-ray intensities observed in the decay of ^{86}Tc. 118

Chapter 1

Introduction

Atoms consist of a cloud of electrons surrounding a central, very small, very dense nucleus. The diameter of the atom is around 1 Angstrom ($\sim 10^{-10}$ m) but the nucleus, which contains almost all of the mass of the atom, is of the order of fermis ($\sim 10^{-15}$ m) in diameter. The atomic nucleus is made up of positively charged protons and neutral neutrons which move independently of each other and interact via the strong and coulomb forces. It is the aim of nuclear physics to understand how protons and neutrons interact.

Elements are characterised by the number of protons, Z, which they possess and the heaviest element to have been discovered to date is element 118 [1]. In chemistry, the elements are commonly displayed in the well known periodic table, grouped by similarities in their chemical properties. Each element has several different isotopes which differ from each other by the number of neutrons, N, in the nucleus. The atomic mass number, A, is the sum of protons, Z, and neutrons, N, which an isotope comprises. As an example, ^{16}O is made of 8 protons and 8 neutrons whereas ^{18}O has again 8 protons but 10 neutrons. Both of these isotopes are stable to radioactive decay and are found in nature but there are other isotopes of oxygen with other neutron numbers ranging from 5 (^{13}O) [2] to the heaviest known to date, ^{24}O [3] with 16 neutrons. Each element has many different isotopes either already discovered or predicted to exist. Current mass predictions estimate around 7000 different isotopes to exist [4], determined by the proton and neutron separation energies (S_p, S_n) being greater than zero. The known isotopes are displayed on the chart of the nuclides (also known as the Segre chart) where the x and y axes show the number of neutrons and protons respectively.

An example is displayed in figure 1.1, taken from reference [5].

This thesis focuses on a special subset of nuclei which contain an equal number of protons and neutrons. These nuclei are commonly referred to as $N = Z$, or self-conjugate nuclei. To date 50 self-conjugate nuclei have been synthesised and 46 of these nuclei have at least some information known about their excited states. Below $^{40}_{20}\mathrm{Ca}_{20}$ the valley of beta stability lies along the same path as the $N = Z$ line and there are 13 radioactively stable $N = Z$ nuclei with $A \leq 40$. Above this point the increasing Coulomb potential created by the protons becomes too large for a stable system and the valley of stability moves to more neutron-rich isotopes (i.e. nuclides in which $N > Z$). As we move up the $N = Z$ line the nuclei move further and further from stability and approach the proton drip line (the point at which the proton separation energy, S_p, is negative and the nuclei become unbound against proton emission [6]). On the way, between N=Z=28→50, the $N = Z$ line traverses a region of ferocious shape competition [7, 8, 9, 10, 11] where changes between spherical, prolate and oblate nuclear shapes can occur with a change of only two or three nucleons or an MeV of excitation energy.

1.1 Isospin, Pairing and $N = Z$ Nuclei

The fundamental principle underlying the concept of nuclear isospin is that the proton and the neutron are two states of the same particle, the nucleon. These two states can be described by wavefunctions, ψ_p and ψ_n, and can be labelled using the isospin quantum number, T [12, 13]. The projection of the total isospin of a nucleus onto an arbitrary axis in isospin space, T_z, is equal to $\frac{1}{2}(N-Z)$, where N and Z are the number of neutrons and protons respectively. It follows that the proton and neutron have projection quantum numbers of T_z = -$\frac{1}{2}$ and +$\frac{1}{2}$ respectively (note that this is the convention in nuclear physics but the assignments are reversed in particle physics). The total nuclear isospin is a vector sum of the form,

$$\boldsymbol{T} = \sum_{i=1}^{A} \boldsymbol{T_i} \tag{1.1}$$

Extra stability can be achieved in the nucleus when nucleons pair up with their intrinsic spins, s, coupled anti-parallel. There is a great deal of evidence for this effect,

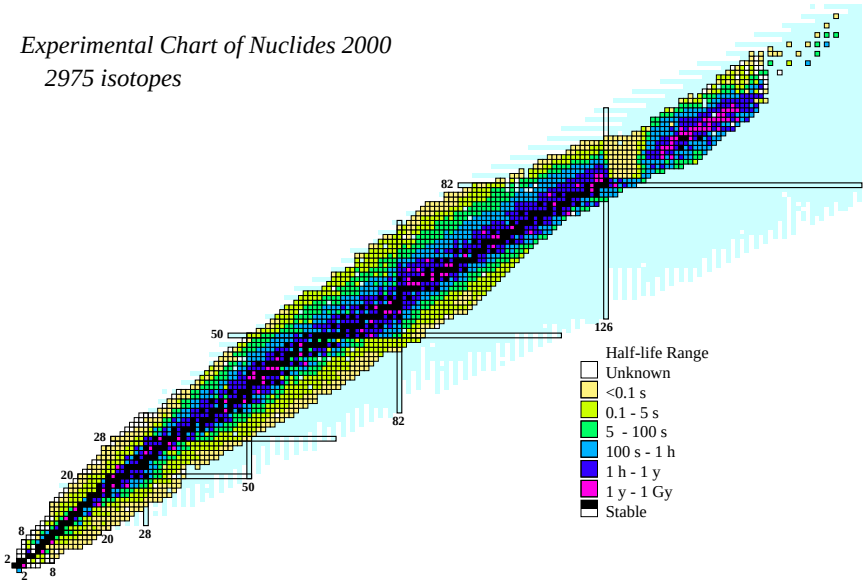

Figure 1.1: *The chart of the nuclides showing nuclear half-lives. Taken from reference [5]. Pale blue squares indicate nuclides which are predicted to exist but which have not yet been observed experimentally.*

for example a simple inspection of binding energies [4] or single-nucleon separation energies [14] shows that even-even nuclei have extra stability, compared to the average of the odd-A neighbouring nuclei, due to pairing effects. Further evidence comes from the fact that the low-lying stucture of the majority of odd-even nuclei can be well described by assuming an inert core of paired-up protons and neutrons coupled to one single odd nucleon. This lone nucleon is responsible for the low-lying excitations observed in that nucleus.

Pairs of protons and pairs of neutrons in identical orbits can only couple their spins in an anti-parallel configuration where $T = 1$ and $s = 0$. This is the requirement for a totally anti-symmetric wavefunction. When a neutron-proton pair (np pair) is formed the proton and neutron have different values of isospin and the intrinsic spins of the two particles can couple in a parallel fashion. This is only possible because of the fact that the proton and neutron are not the same particle and thus have a different value of T_z, thereby satisfying the requirement for a fully anti-symmetric wavefunction. Note that np pairs can also align their spins anti-parallel to form $T = 1$, $s = 0$ pairs,

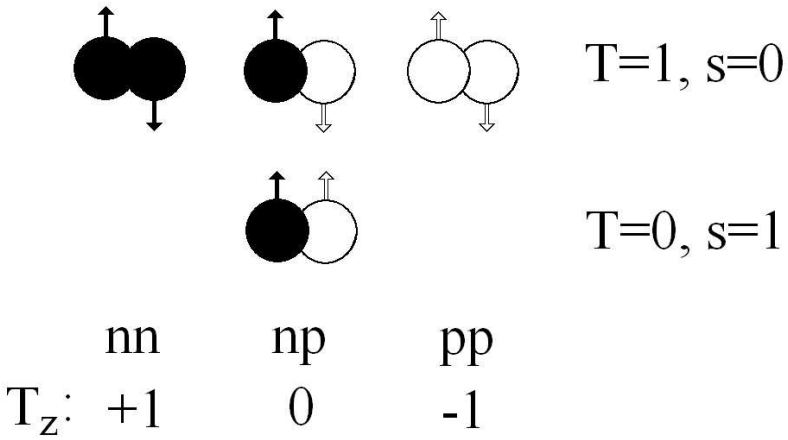

Figure 1.2: *Schematic of the allowed intrinsic angular momentum couplings in the A=2 isobaric triplet. Only a neutron-proton pair is capable of coupling to $T = 0$, $s = 1$. Adapted from figure 3.12 in reference [15]*

as in the analogous *nn* and *pp* pairs with $T = 1$ (see figure 1.2).

A unique situation emerges in nuclei with an equal number of both protons and neutrons. It is possible to form low-lying $T = 0$ states and, unlike nuclei in other regions of the nuclear chart, it is only here in $N \approx Z$ nuclei that the proton and neutron forming the pair are in identical single-particle orbitals.

In light odd-odd, $N = Z$ nuclei the state of lowest energy (the ground state) corresponds to the $T = 0$ configuration. If the *np* pair is exchanged for a *pp* or a *nn* pair then only $T = 1$ states can be formed. The $T = 0$ configurations also exist in the nucleus with the *np* pair but as excited states. These states are known as Isobaric Analogue States (IAS) (see figure 1.3) and appear at similar energies (usually within a few tens of keV) in all isobaric partners, only changing energy due to Coulomb effects and the fact that protons and neutrons have slightly differing masses.

The energy difference between the lowest observed $T = 0$ and $T = 1$ states in odd-odd $N = Z$ nuclei can be plotted against mass for the $N = Z$ nuclei, as shown in figure 1.4. The data for this plot are taken from references [9, 17, 18, 19, 20, 21, 22, 23, 24, 25, 26, 27, 28]. At low mass the $T = 0$ state is the most stable configuration, as in the deuteron, and forms the ground state. However as the mass increases the energy difference decreases and at A=34 the first case of isospin inversion occurs. This is seen experimentally by the fact that $^{34}_{17}\mathrm{Cl}_{17}$ has a ground state with spin and parity of $I^{\pi} = 0^{+}$ [19]. The $N = Z = 29$ system, $^{58}_{29}\mathrm{Cu}_{29}$ [17], is the only odd-odd $N = Z$

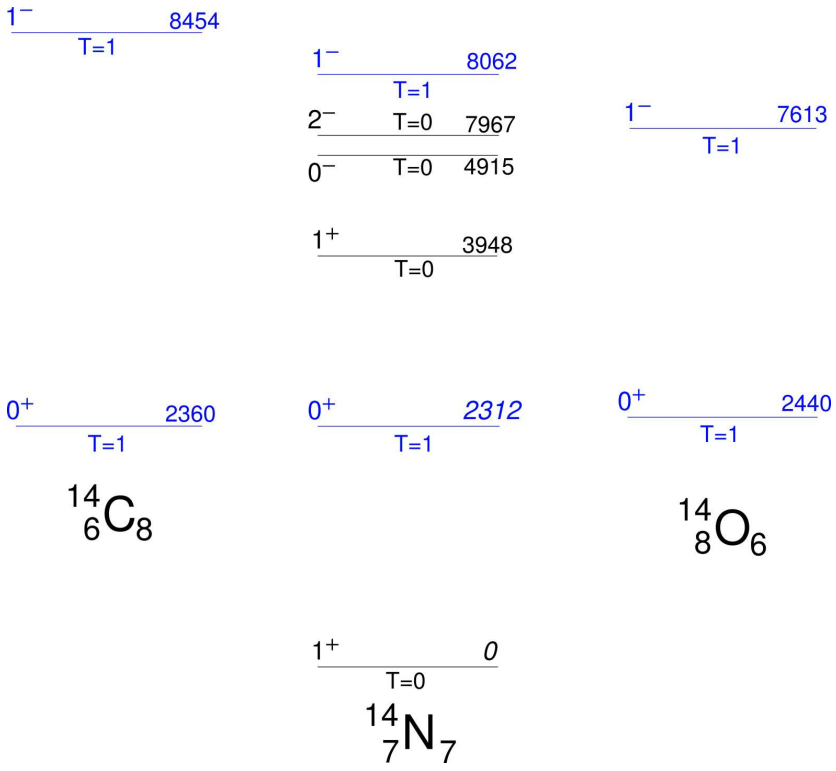

Figure 1.3: *An example of an isobaric triplet. $T = 1$, Isobaric Analogue States (shown in blue) exist in each nuclide. The states in carbon and oxygen have been shifted by the difference in the proton-neutron masses and the Coulomb energy. This figure is adapted from reference [16].*

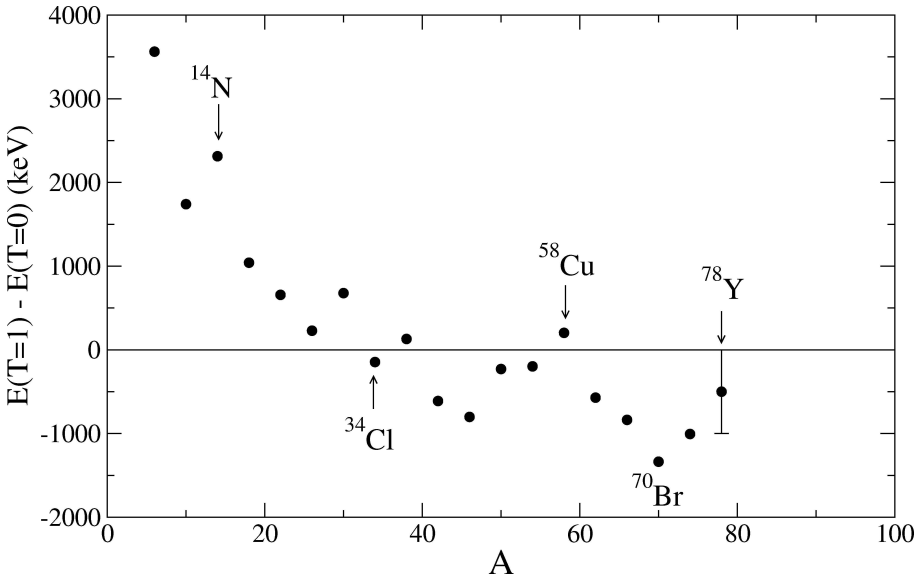

Figure 1.4: *Energy difference between the lowest observed $T = 0$ and $T = 1$ states in odd-odd $N = Z$ nuclei. Nuclei with positive energy differences have $T = 0$ ground states, those with negative energy differences have $T = 1$.*

nucleus with $34 < A \leq 100$ that has a confirmed $T = 0$ ground state [29].

It is for these reasons that $N = Z$ nuclei are the ideal laboratory in which to study interactions between protons and neutrons.

1.2 Isomeric States

Metastable states, isomeric states or isomers are excited nuclear levels which exist for an extended period of time [30]. There is no formal condition on the length of the half-life for an excited state to be considered as isomeric. The shortest possible mean lifetime for an excited state to be classed as a bound nuclear state is around 0.1 zeptoseconds (10^{-22} s), equivalent to the period of time it takes a single nucleon to orbit the nucleus. The longest know excited states in nuclei can live for many years. The isomeric state in ^{180}Ta has a half-life greater than 1.2×10^{15} years [31]. Excited states which exist for this amount of time are considered to be very long-lived isomers.

Lifetimes of excited states can be measured using a large variety of techniques and experimental equipment. The shortest mean lifetimes which can be measured today are in the 10^{-22} s range. This is done by examining the intrinsic energy width, Γ, of the state which is related to the mean lifetime, τ, by the Heisenberg Uncertainty principle

where $\Gamma\tau = \hbar$.

Sub-picosecond lifetimes of excited states can be measured using the recoil distance method [32]. This technique takes advantage of the fact that the nucleus of interest is formed whilst travelling at high speed and therefore gamma rays emitted in the decay of excited states have a different energy to the same gamma ray emitted from a nucleus at rest. In other words the gamma-rays emitted whilst travelling at high speed are doppler-shifted. The nucleus of interest can be stopped at various distances from the formation point and, by using the ratio of the intensities of the stopped and shifted components of the peak, the mean lifetime of the state can be extracted. Scintillator detectors made from materials such as BaF_2 [33] coupled to fast photomultiplier tubes can be used to measure lifetimes down to a few hundred picoseconds. Isomeric states with mean lifetimes of 10 nanoseconds to ∼1 millisecond can be measured using timing relative to a germanium detector gamma-ray decay signal with standard NIM logical electronics.

1.3 The Neutron-Deficient $N \approx Z \sim 40$ Nuclides

The proton drip line between $_{28}$Ni and $_{50}$Sn has been carefully mapped in fragmentation studies [34, 35]. Above $A \geq 70$ the odd-odd $N = Z$ nuclei lie on the proton drip line, with the exception of ^{78}Y because ^{76,77}Y are particle bound [35, 36, 37]. The proton drip line at this point lies 10 or 11 neutrons away from the stable isotopes as is seen in figure 1.5. The proton drip line, the point at which the proton separation energy (S_p) becomes negative, as determined in the atomic mass evaluation of 2003 [4] is indicated in this plot by the red line. Nuclei which lie to the left of this line can decay by proton emission from the ground state. The odd-even staggering effect of the proton drip line can also been seen here, indicating the extra binding energy availible in the pairing of nucleons. The nuclei studied in the work presented in this thesis are indicated in blue.

The mass parabolas for the $A = 82$ and 86 isotopic chains are plotted in figure 1.6. In both cases the $T_z = 0$ nucleus is the last bound isotope on the neutron deficient side. Note in these plots that the even-even isobars possess extra binding compared to the neighbouring odd-odd isobars.

As neutron and proton numbers move away from closed shells, where nuclei are

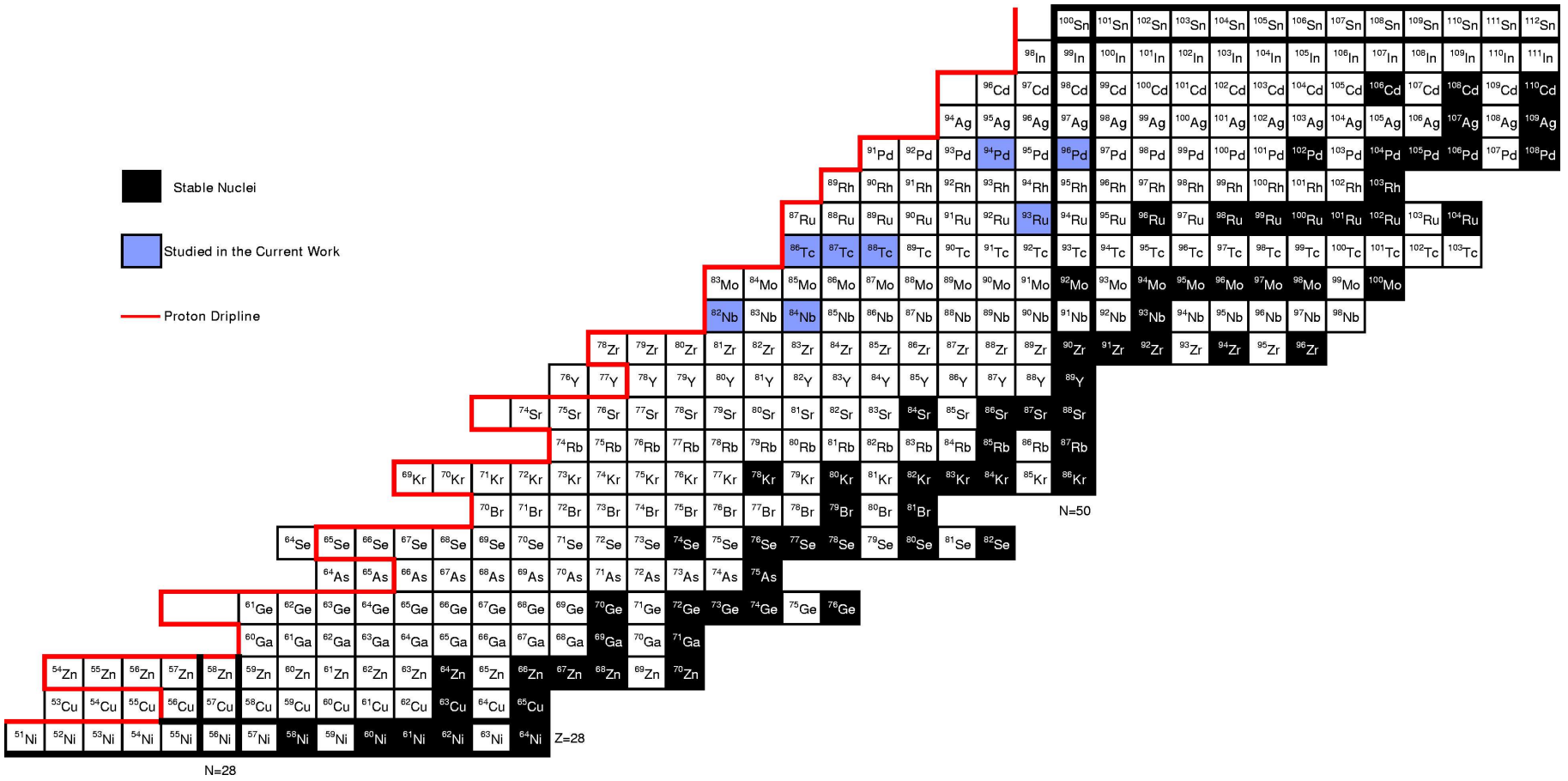

Figure 1.5: *Part of the chart of the nuclides showing the stable isotopes and location of the proton drip line [4] for elements between* $_{28}Ni$ *and* $_{50}Sn$ *and* $N \leq 62$*. There are no stable isotopes of Tc. Indium has two stable isotopes,* ^{113}In *and* ^{115}In *which are not shown.* $_{46}Pd$*,* $_{48}Cd$ *and* $_{50}Sn$ *also have other stable isotopes with* $N > 62$ *which are not shown.*

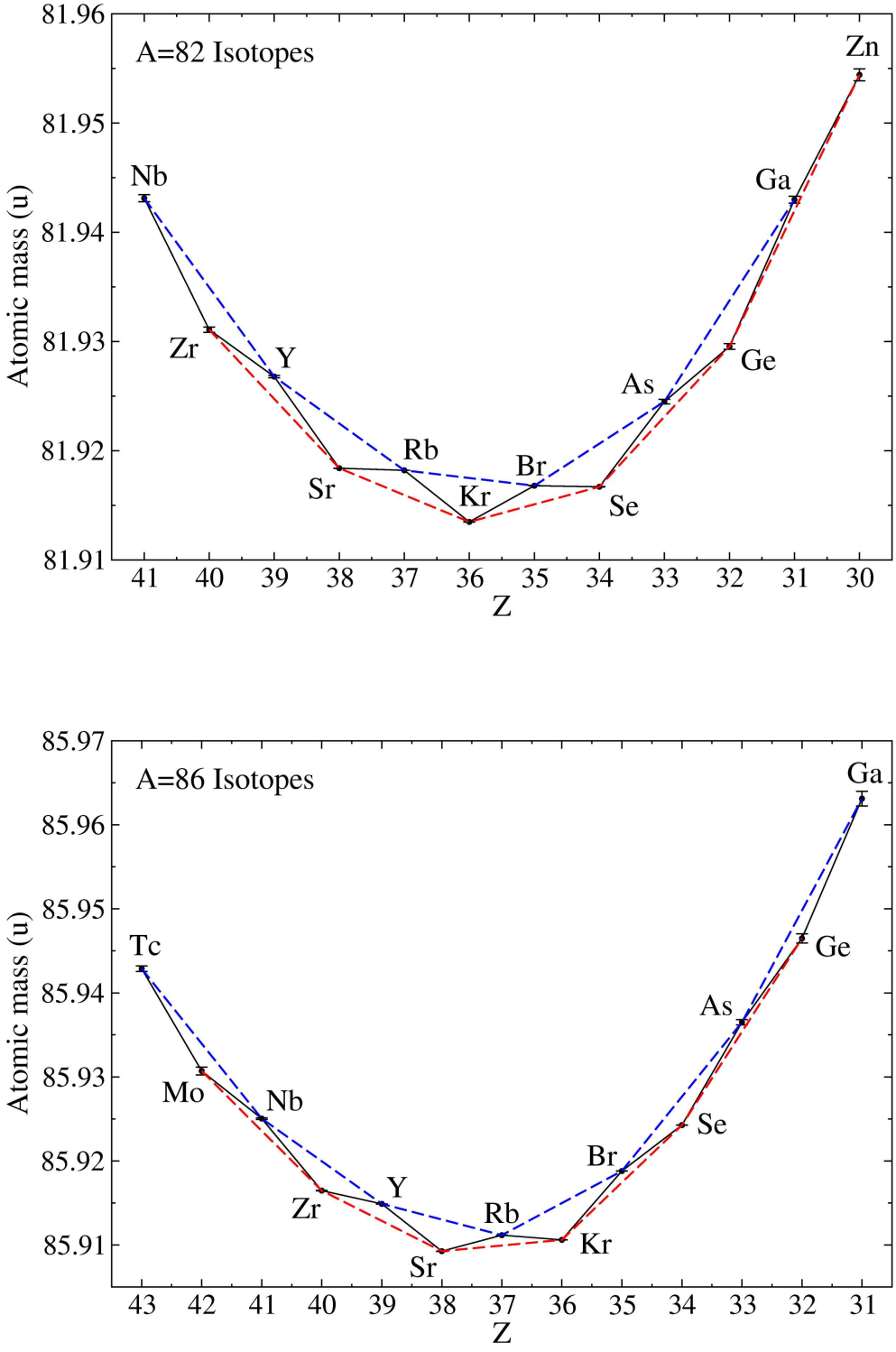

Figure 1.6: *Atomic masses of the $A = 82$ and $A = 86$ isobars. The stable isobars are ^{82}Kr, ^{82}Se, ^{86}Sr and ^{86}Kr. ^{82}Nb and ^{86}Tc are also the lightest bound $Z = 41, 43$ isotope respectively. The blue and red lines show the odd-odd and even-even mass parabolas respectively.*

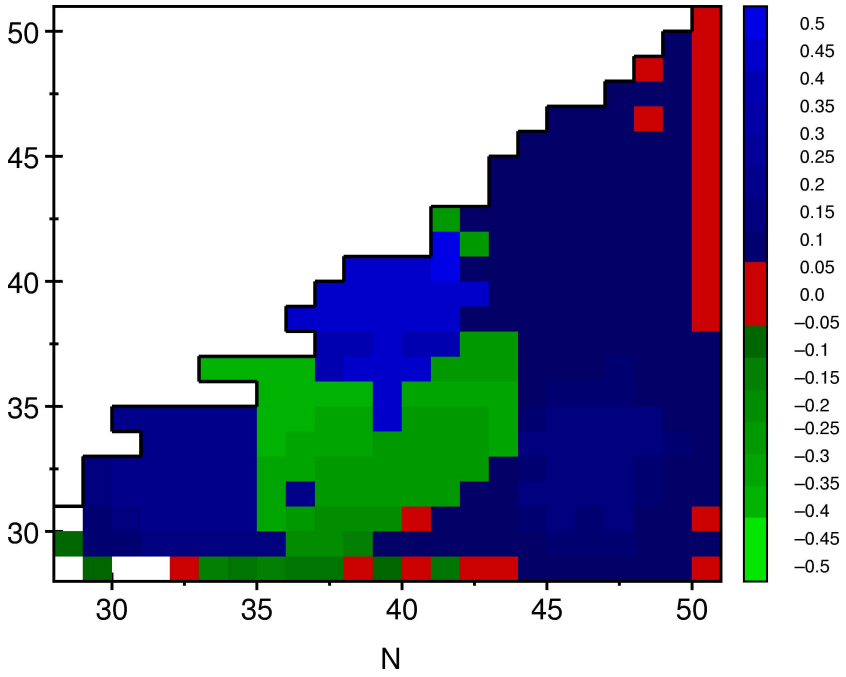

Figure 1.7: *Predictions of ground-state deformations of nuclei in the fpg shell calculated with a finite-range droplet macroscopic model and the folded-Yukawa single-particle microscopic model, taken from reference [38].*

mostly spherical, deformed shapes can become more favourable. In the fpg shell there is a low density of single-particle orbitals near the Fermi surface which nucleons can occupy. These orbitals also have similar energies for both the neutrons and protons. If a deformed shape becomes favourable the effect is magnified by the similarity between the neutron and proton orbitals. This can lead to dramatic differences in the shape of nuclei with very similar proton and neutron numbers. Predictions of the ground state deformations of nuclei between ^{56}Ni and ^{100}Sn calculated with a finite-range droplet macroscopic model and the folded-Yukawa single-particle microscopic model [38] are shown in figure 1.7. A sharp transition from prolate to oblate and back to prolate shapes can be seen along the $N = Z$ line in the centre of the plot.

The nucleus $^{86}_{43}\mathrm{Tc}_{43}$ is currently the heaviest odd-odd, $N = Z$ system in which internal de-excitations have been identified. During an experiment at GANIL in 1999 [39], an isomer was identified in this nucleus with the observation of two gamma rays (figure 1.8) and a measured mean lifetime of 1.6 ± 0.3 μs.

The two observed transitions were interpreted as being isobaric analogue states of the even-even neighbour, $^{86}_{42}\mathrm{Mo}_{44}$. From inspection of the single-particle energy levels

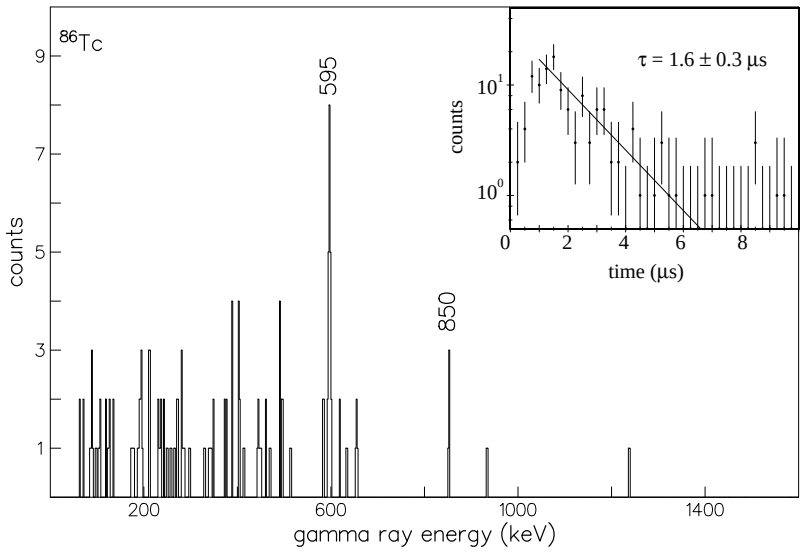

Figure 1.8: *Spectrum of delayed gamma-rays from ^{86}Tc produced in an experiment at GANIL in 1999. The inset is the associated time spectrum. Taken from reference [39].*

available in this region, it was suggested that the isomer had a spin of 5 and was of a $T = 0$ character. Therefore the gamma-ray decay of the isomeric state was thought to be feeding, via an unobserved M1 or E1 transition, the I^{π}=4^{+}, $T = 1$ state of the ground-state band.

Evidence was also provided in the same experiment for an isomeric state in $^{82}_{41}\mathrm{Nb}_{41}$. Low statistics prevented the identification of any descrete gamma rays in that work.

The purpose of this thesis is to present new experimental results for these heavy self-conjugate nuclei. The recent results come from an experiment performed in February 2006 as part of the RISING Stopped Beam campaign at GSI. Evidence is presented for the $T = 1$ neutron-proton pairing interaction to be dominant over its $T = 0$ counterpart. In addition the experiment has allowed the identification of three previously unreported isomeric states in ^{87,88}Tc and ^{84}Nb.

A theoretical background is presented in Chapter 2 followed by a summary of the relevant experimental techniques in Chapter 3. Chapter 4 outlines the data analysis procedures employed to obtain the final results which are presented and discussed in Chapter 5.

Chapter 2

Theory

2.1 Radioactive Decay

Many nuclei can gain stability by changing their configuration in some way through the process of radioactive decay. Radioactive decay can take place either within a nucleus, that is, de-exciting a nuclear state by emission of a gamma ray or an internal conversion electron, or between different nuclei by either changing the nature of one or more of its constituent parts (beta decay) or by ejecting one or more nucleons (proton emission, alpha decay etc.). The processes relevant to the work presented in this thesis are described in more detail in the following sections.

2.1.1 Lifetimes of Nuclear States

The mean lifetime, τ, of an excited state is related to the intrinsic energy width, Γ, by the Heisenberg Uncertainty principle [40] so that

$$\Gamma\tau = \hbar \tag{2.1}$$

where $\hbar$ is Planck's constant divided by 2π, $\frac{h}{2\pi} = 1.05 \times 10^{-34}$ Js. The mean lifetime is related to the half-life, $t_{\frac{1}{2}}$, by the decay constant, λ so that

$$\tau = \frac{1}{\lambda} \tag{2.2}$$

and

$$t_{\frac{1}{2}} = \frac{\ln(2)}{\lambda} \tag{2.3}$$

therefore

$$t_{\frac{1}{2}} = \ln(2)\tau \tag{2.4}$$

where λ is the sum of all decay constants for all possible modes of decay.

2.1.2 Beta Decay

Beta decay is the process by which a nucleon changes from a proton to a neutron, or vice versa. Charge conservation laws necessitate the creation of an electron or positron at the same time and this leads to the requirement for the creation of an anti-neutrino or neutrino to satisfy lepton conservation rules. The two allowed processes are [16, 41],

$$n \rightarrow p + e^- + \overline{\nu_e} \tag{2.5}$$

$$p \rightarrow n + e^+ + \nu_e \tag{2.6}$$

The former is β^- decay and the latter β^+ decay. β^+ decay competes with a second process in which an atomic electron, usually from the lowest electron orbital (K shell), and a proton are transformed into a neutron. This is known as electron capture and can be summarised by,

$$p + e^- \rightarrow n + \nu_e \tag{2.7}$$

There are several different classes of beta decay dependent on the amount of angular momentum transferred and the parity of the initial and final states. Each of these classes have different half-lives due to the degree of overlap between the wave functions of the initial and final states. Table 2.1 shows the different classifications of

beta decay with their corresponding selection rules [16]. Note that the titles of *allowed* and *forbidden* are used for describing beta decay, however *forbidden* is misleading as the decay is not actually forbidden but is simply less likely (and therefore slower) than *allowed* decays. The difference between *allowed* and *forbidden* decays is that *forbidden* decays require an amount of orbital angular momentum to be transferred in addition to the intrinsic spins of the particles involved. If the intrinsic spins of the electron and neutrino are coupled in an anti-parallel fashion the decay is known as Fermi decay, if the spins are parallel then the decay is Gamow-Teller in nature.

Beta-decay probabilities can be compared by $\log ft$ values. The value, ft is the comparative half-life [16],

$$ft_{\frac{1}{2}} = 0.693 \frac{2\pi^3\hbar^7}{g^2 m_e^5 c^4 |M_{fi}|^2} \tag{2.8}$$

where g is the beta-decay strength ($0.88 \times 10^{-4} MeV fm^3$ [16]) and $|M_{fi}|$ is the nuclear matrix element. The dependence of the decay probability on the maximum electron energy, E_0, and the atomic number, Z', of the daughter nucleus is incorporated into the Fermi integral, $f(Z', E_0)$, so the $\log ft$ value changes only with the nuclear matrix element, $|M_{fi}|$. Small $\log ft$ values indicate a large overlap in the nuclear wave functions of the initial and final states and correspond to fast transitions. Typical $\log ft$ values for the different classifications of beta decay are shown in the right-hand column of table 2.1 (these values are taken from [16]).

2.1.3 Gamma Decay

Gamma decay is the mechanism by which a nucleus in an excited state loses energy and angular momentum by emitting a photon. The restriction of conservation laws create selection rules for the permissible values of energy (E), angular momentum (L) and parity ($\Delta\pi$) which a gamma-ray transition may possess. The energy of a gamma-ray transition between states of energy E_i and E_f is approximately equal to,

$$E_\gamma \cong E_i - E_f \tag{2.9}$$

the emitting nucleus experiences a small amount of recoil due to the conservation of momentum therefore the gamma ray has slightly less energy than the full value of

Table 2.1: *Beta decay selection rules for the change in angular momentum, ΔI, and parity, $\Delta\pi$ [16]. Note that second, third and fourth forbidden process can also change the spin by less then stated below but those transitions would favour lower order decay processes, such as first forbidden.*

Class	ΔI	$\Delta\pi$	$\log ft$
(Super)Allowed, Fermi	0	no	2.9-3.7
Allowed, Gamow-Teller	0,1	no	4.4-6.0
First Forbidden, Fermi	0,1	yes	6-10
First Forbidden, Gamow-Teller	0,1,2	yes	6-10
Second Forbidden	2,3	no	10-13
Third Forbidden	3,4	yes	13-21
Fourth Forbidden	4,5	no	22-24

$E_i - E_f$. The angular momentum of the transition can take several different values but is restricted to the range of

$$|I_i - I_f| \leq L \leq I_i + I_f \tag{2.10}$$

and the parity change of the transition is dependent on the polarity of the transition so that decays that are electric in nature have a parity change of

$$\Delta\pi(EL) = (-1)^L \tag{2.11}$$

and those of a magnetic nature have parity

$$\Delta\pi(ML) = (-1)^{L+1} \tag{2.12}$$

where L is again the angular momentum of the transition. It is usual that more than one multipole of transition will satisfy these selection rules. In these cases it will be the lowest order multipole which dominates the transition and has the largest transition probability [16, 42],

$$T_{fi}(\lambda L) = \frac{8\pi(L+1)}{\hbar L((2L+1)!!)^2}\left(\frac{E_\gamma}{\hbar c}\right)^{2L+1} B(\lambda L : J_i \rightarrow J_f) \tag{2.13}$$

where $B(\lambda L)$ is the reduced transition probability for a transition of multipolarity, λ, which carries L units of angular momentum and E_γ in MeV of energy. These reduced transition probabilities are given by the reduced matrix elements

$$B(E\lambda : I_i - I_f) = \frac{1}{2I_i+1}\left|\langle f|Q_L|i\rangle\right|^2 \tag{2.14}$$

for transitions of an electric nature and

$$B(M\lambda : I_i - I_f) = \frac{1}{2I_i+1}\left|\langle f|M_L|i\rangle\right|^2 \tag{2.15}$$

for magnetic transitions where Q_L and M_L are the electric and magnetic multipole operators respectively. Transition probabilities are often stated in Weisskopf units to give a feeling for the approximate and relative magnitude of the transition rate. The transition strengths in terms of the Weisskopf estimates [42] are given by

$$B(Wu : EL) = \frac{1.2^{2L}}{4\pi}\left(\frac{3}{L+3}\right)^2 A^{\frac{2L}{3}} e^2 fm^{2L} \tag{2.16}$$

for electric transitions and

$$B(Wu : ML) = \frac{10}{\pi}1.2^{2L-2}\left(\frac{3}{L+3}\right)^2 A^{\frac{2L-2}{3}}\left(\frac{e\hbar}{2Mc}\right)^2 fm^{2L-2} \tag{2.17}$$

for magnetic transitions where A is the atomic mass and M is the single nucleon mass. Figure 2.1 shows the Weisskopf estimates for different multipolarity transitions in ^{86}Tc for energies between 50 and 1000 keV.

Isospin Selection Rules

Additional selection rules which consider isospin exist for electromagnetic transitions [12]. The isospin of the initial, T_i, and final, T_f, states must be considered.

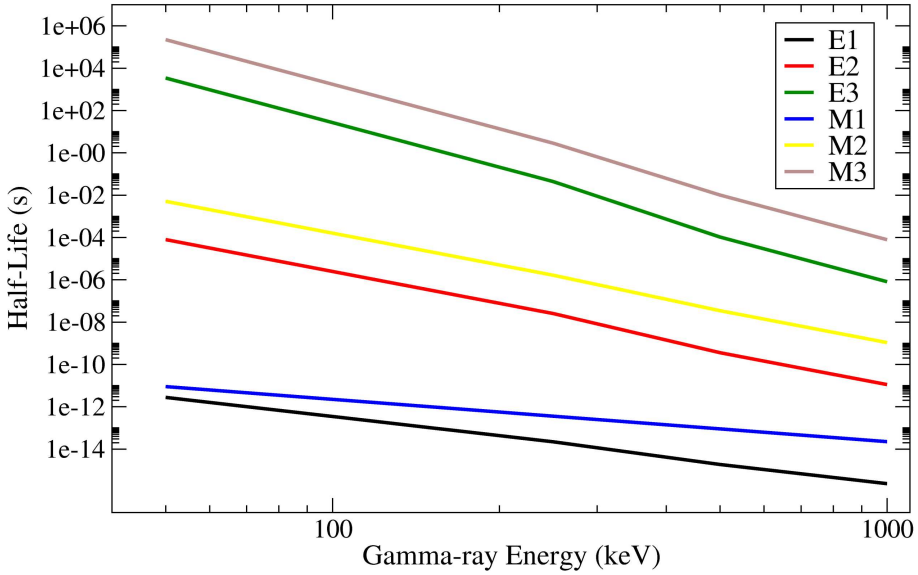

Figure 2.1: *Weisskopf estimates for decay half-lives of different multipolarity transitions in* ^{86}Tc *of energies between 50 and 1000 keV.*

Electromagnetic transitions which change the isospin between initial and final states ($\Delta T = T_f - T_i \neq 0$) are known as *isovector* transitions. Transitions which do not change isospin ($\Delta T = 0$) are *isoscalar*. A selection rule for any gamma-ray transition in any nucleus is that the isospin cannot change by more than 1 unit so that, $\Delta T = 0$ or ± 1. The only exception to this rule is for electric dipole (E1) transitions in T_z=0 nuclei where there must be a change in isospin, $\Delta T = \pm 1$.

2.1.4 Internal Conversion

A decay process which competes with the gamma-ray emission of excited nuclear states is the mechanism of internal conversion. The transition energy (the difference between the inital and final states, $E_t = E_i - E_f$, minus a small amount for the recoiling nucleus) is passed directly to an atomic electron. The kinetic energy, E_k, of the electron following its emission from the atom is equal to the energy difference between the transition energy and the binding energy of that electron so that

$$E_k \cong E_t - B_i \tag{2.18}$$

where B_i is the binding energy for an electron in the i^{th} electron shell. Following internal conversion there is a vacancy in the electron orbital from which the electron

was removed. This vacancy is filled by an electron from a higher orbital and as such an X ray or Auger electron is emitted.

The Internal Conversion Coefficient (ICC) [16], α_i, of a transition is the probability of an electron from the i^{th} electron shell competing with gamma-ray emission and is equal to

$$\alpha_i = \frac{I_{e_i^-}}{I_\gamma} \tag{2.19}$$

where $I_{e_i^-}$ and I_γ are the intensities of the competing processes. It follows that the total internal conversion coefficient, α_{TOT}, is the sum of the probabilities of internal conversion from all occupied electron shells so

$$\alpha_{TOT} = \alpha_K + \alpha_L + \alpha_M + ... \tag{2.20}$$

and the total decay probability is

$$I_{TOT} = I_\gamma(1 + \alpha_{TOT}) \tag{2.21}$$

The values of internal conversion coefficients change with Z, the transition energy, E_t, and the multipolarity, λL of the transition so that the internal conversion coefficients for transitions of an electric and magnetic nature [16] are

$$\alpha(EL) \approx \frac{Z^3}{n^3}\left(\frac{L}{L+1}\right)\left(\frac{e^2}{4\pi\epsilon_0\hbar c}\right)^4\left(\frac{2m_ec^2}{E_t}\right)^{L+\frac{5}{2}} \tag{2.22}$$

and

$$\alpha(ML) \approx \frac{Z^3}{n^3}\left(\frac{e^2}{4\pi\epsilon_0\hbar c}\right)^4\left(\frac{2m_ec^2}{E_t}\right)^{L+\frac{3}{2}} \tag{2.23}$$

where Z is the atomic number, n is the principle quantum number of the electron shell and L is the multipolarity of the transition of energy, E_t [16]. The total conversion coefficients for technetium ($Z = 43$) for various multipolarity transitions of energies ranging between 40 and 1000 keV are shown in figure 2.2.

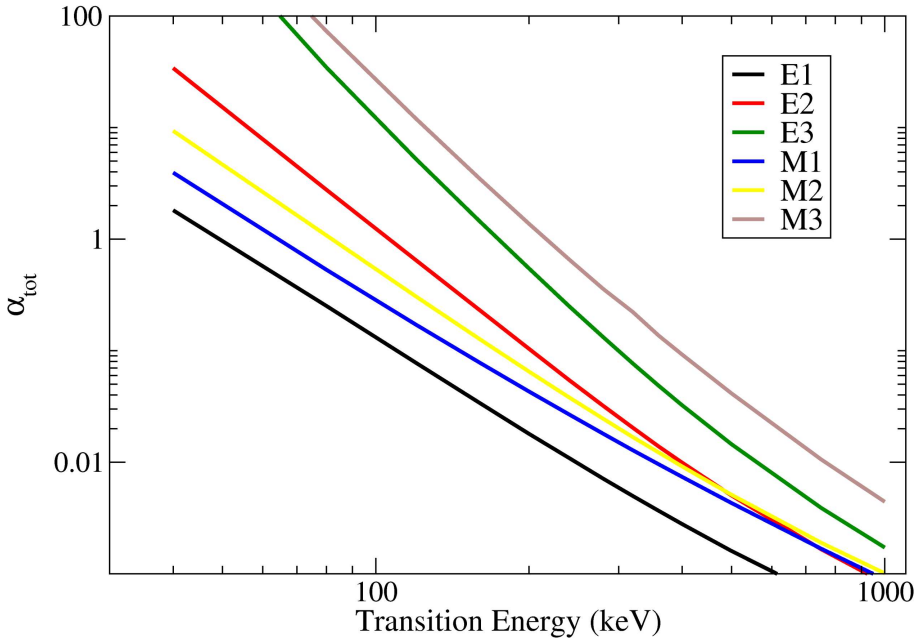

Figure 2.2: *Total internal conversion coefficients for various multipolarity transitions in Tc of energies between 40 and 1000 keV.*

2.1.5 Proton Decay

Direct proton emission is the de-excitation of a nuclear state by the ejection of a proton [6]. In some cases this state can be the ground state of a nucleus and in others an excited state which lies above the proton separation energy, S_p. The theory of proton emission is a simple quantum tunnelling problem through a potential barrier which is comprised of a coulomb and a centrifugal contribution. The situation is a little more complex for alpha decay in which the alpha particle must first be formed inside the nucleus, requiring the inclusion of a preformation factor.

The potential barrier can be modelled with a nuclear potential [43]. The addition of a centrifugal part then comes from the orbital angular momentum, l, of the orbital from which the proton is emitted. With this information WKB calculations can be performed to accurately predict the proton partial half-life in the decay. Conversely a measurement of the half-life and proton energy of a proton decay can give accurate information on the occupancy and position of single-particle orbitals.

2.2 Theoretical Nuclear Models and Calculations

Many theoretical models exist to describe nuclear systems, their behaviour and properties. The aim of any nuclear model is to accurately predict the structure and evolution of structure in a large range of nuclei. Some models approach this problem by describing the behaviour of the individual constituents of the nucleus, the protons and neutrons, and examining how their interactions effect the properties of the nucleus as a whole. Other models take a rather different approach and assume the nucleus is a single entity, such as a liquid drop, and use collective excitations and behaviour to describe observed nuclear properties. These two approaches are known as microscopic and macroscopic approaches respectively [15, 42, 44, 45]. Both have shown great success at describing many aspects of nuclear behaviour and properties. Some specific theoretical models are described in further detail below.

2.3 The Independent Single-Particle Model

The nuclear shell model is based on the concept that neutrons and protons in the nucleus fill shells in sequential order and, when full, these shells form an inert core. Any nucleons which occupy an unfilled shell ('valence' nucleons) are then responsible for the behaviour of excitations in the nucleus. This idea is analogous to the atomic shell model which shows excellent agreement with observed atomic data. The nuclear shell model also has many successes such as predicting the stable magic numbers (2, 8, 20, 28, 40, 50, 82, 126) [46]. Around these shell closures, where there are only a few valence nucleons, the observed level structures of nuclei can be very well described by the shell model.

In order to recreate the level structure seen in nuclei using the shell model the nucleons are described as occupying discrete orbits in a spherically symmetric potential, $V(r)$. The form of the potential and the degree of degeneracy is extremely important if the empirically observed structure is to be reproduced accurately. The potential $V(r)$ is created by the nucleons themselves and has a range of around 1 fm (the approximate range of the nucleon-nucleon force). A simple potential that can be used initially is the Simple Harmonic Oscillator (SHO) potential of the form

$$V(r) = \frac{1}{2}m\omega^2 r^2 \tag{2.24}$$

where m is the mass of the particle in the potential, ω is the rotational frequency of that particle and r is the orbital radius from the centre of mass. If we solve the time independent Schrödinger equation

$$\left(-\frac{\hbar^2}{2m}\nabla^2 + V(r)\right)|\phi\rangle = E|\phi\rangle \tag{2.25}$$

for nucleons in the SHO potential we can extract the eigenvalues of energy E. If the results are for a three dimensional oscillator then the eigenvalues E_{nl} can be written as $(2n + l - \frac{1}{2})\hbar\omega$ where the lowest value of n is 1. The levels produced are shown on the left side of figure 2.3 (taken from [47]). The levels are split only by the principal quantum number, N, but the magic numbers up to 40 are reproduced correctly. Above this point there is disagreement. It is clear the SHO is a good approximation to the potential at low values of r, i.e. close to the centre of the potental, but the SHO tends to infinity for larger r. The real nuclear potential is short range and therefore additional degeneracy and some modification is required.

The Woods-Saxon potential [48] takes the form

$$V(r) = \frac{V_0}{1 + e^{\frac{r-R_0}{a}}} \tag{2.26}$$

where r is the radial distance from the centre of the potential, a is the surface diffuseness term (an indication of how quickly the potential reduces to zero), and $R_0 = 1.2A^{\frac{1}{3}}$fm (R_0 is the distance at which the potential drops to half that of V_0). Using this potential in calculating single-particle energy levels has the effect of splitting the degeneracy of the SHO levels and lowering the state of largest orbital angular momentum, l, in each N group. These results are displayed in the centre of figure 2.3.

To reproduce the complete set of observed magic numbers a spin-orbit term is needed. As suggested independently by Mayer [46] and Haxel, Jensen and Suess [49], this term is of the form,

$$V_{l\bullet s} = -V_{ls}\frac{\delta V(r)}{\delta r}\, l_\bullet s \tag{2.27}$$

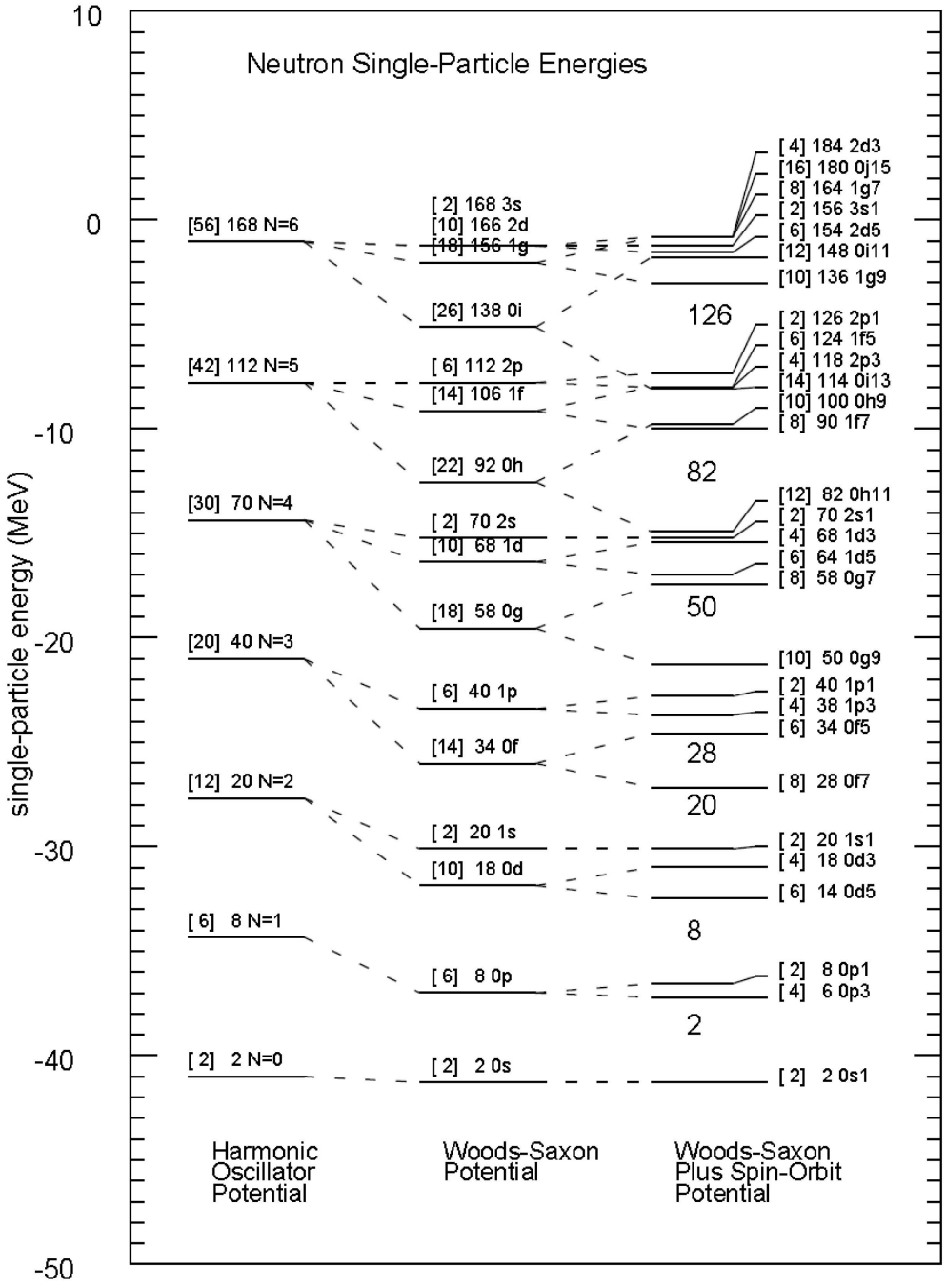

Figure 2.3: *The single-particle energy levels of the shell model derived from* **Left:** *A Simple Harmonic Oscillator (SHO) potential,* **Centre:** *Woods-Saxon potential and,* **Right:** *A Woods-Saxon potential plus spin-orbit ($l \bullet s$) term. The level labels are of the following form: In square brackets is the maximum occupancy of that level, the number of particles if all levels up to and including that level are fully occupied, and the name of the level in the form $Nl(j\times 2)$ where N is the major oscillator shell, l the orbital angular momentum, and j the total angular momentum. This figure is taken from reference [47].*

where l and s are the orbital angular momentum and intrinsic spin vectors respectively. V_{ls} is a strength constant. The introduction of this term splits the degeneracy further and again lowers the state of largest total angular momentum (j), this time from each l group. As already mentioned, and demonstrated on the right side of figure 2.3, the magic numbers close to stability are now reproduced correctly.

The nuclear shell model tends to have more difficulty describing the structure of nuclei away from closed shells where collective modes of excitation become more important. Another area in which the shell model often fails is in describing high-spin structures which are often collective in nature. These shortcomings are due to the fact that, to describe these structures, nucleons must be promoted out of the inert core. Once more valence nucleons are available to couple to higher angular momenta, more states are available to mix and produce collective structures. To describe these nuclei macroscopic models are often used which describe the global properties of the nuclear matter instead of the behaviour of individual constituents.

2.4 The Shell Model

The shell model is essentially the independent single-particle model plus some residual interactions. These residual interactions are included as a perturbation but can often have very dramatic effects on the level schemes calculated for nuclei.

2.4.1 The Coupling of Angular Momenta

A single nucleon has an intrinsic spin, s, of $\frac{1}{2}$ and an orbital angular momentum, l. These quantities couple to a total angular momentum, j, such that $\boldsymbol{j} = \boldsymbol{l} + \boldsymbol{s}$.

Each nuclear orbital of angular momentum, j, has $2j+1$ magnetic substates of angular momentum, m_j, where m_j can take the values $-j \leq m_j \leq j$. The permissible values of total angular momentum, J, to which nucleons can couple in a multiparticle configuration of n particles in an orbital of angular momentum, j, can be derived using the m-scheme. The Pauli principle prevents identical particles from occupying the same m_j substate and therefore the maximum possible coupling of angular momentum is

$$J_{max} = nj - \frac{n(n-1)}{2} \tag{2.28}$$

for a $|j^n J\rangle$ configuration. The approach of the m-scheme is to systematically couple all combinations of M (where $M = m_1 + m_2 ... m_n$) for all particles in all substates. When all combinations are determined it is only those values of J for which a complete set of M substates (i.e. $M = J, J-1, ... -(J-1), -J$) exist that are the permissible total angular momentum couplings.

The angular momenta for the ground states of odd-odd nuclei are determined by the coupling of the angular momentum of the last two valence nucleons. All other nucleons form S=0 pairs and therefore do not contribute any angular momentum. The allowed couplings of the last proton and neutron are given by the Gallagher and Moszkowski selection rules [50] where

$$\begin{aligned} J &= j_p + j_n \text{ if } j_p = l_p \pm \frac{1}{2} \text{ and } j_n = l_n \pm \frac{1}{2} \\ J &= |j_p - j_n| \text{ if } j_p = l_p \pm \frac{1}{2} \text{ and } j_n = l_n \mp \frac{1}{2} \end{aligned} \tag{2.29}$$

2.4.2 The Pairing Interaction

The pairing interaction was introduced to recreate the observed nuclear data on properties such as binding energies [4], neutron and proton separation energies [14], angular momentum of nuclear ground states and the low density of states at low excitation energy in even-even nuclei when compared to odd-odd nuclei. All these data show a lowering of the first 0^+ state in even-even nuclei. The pairing interaction recreates this effect without affecting any other states. So if a pairing interaction is the only residual interaction that is applied to a configuration which is formed by a pair of nucleons in equivalent orbits of total angular momentum j then the spectrum will consist of a low-lying 0^+ state and a degenerate multiplet of states up to spin $2j-1$. At the centre of figure 2.4 is an example of this for a $j = (7/2)^2$ configuration.

2.4.3 The δ Interaction

The δ interaction is a residual interaction which acts on the angular part of the wave function of a multi-particle configuration. The greatest effect is seen when the angular momentum coupling is at a minimum or maximum. If no residual interaction were present then all J values of a particular configuration would have the same energy value, i.e. they would be degenerate (shown to the left of figure 2.4). The δ interaction

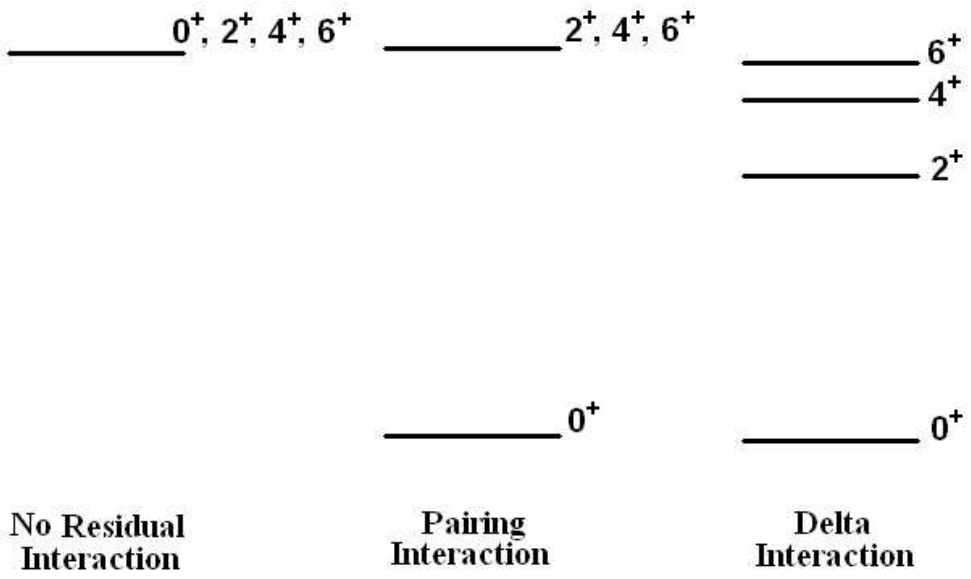

Figure 2.4: *The level structure of a $j=(7/2)^2$ configuration with, from left to right, no residual interaction, a pairing interaction, and a δ function interaction applied.*

applies an energy shift to each J value and can recreate the observed relative energy spacings in even-even nuclei close to doubly-magic nuclei. An example can be seen on the right-hand side of figure 2.4 for a $j = (7/2)^2$ configuration.

2.4.4 Two-State Mixing

The configurations of two states which possess the same spin and parity can become mixed. If the initial, unperturbed levels have energies E_1 and E_2 respectively and they can be described by the wave functions ϕ_1 and ϕ_2 then an interaction between them of V will result in a mixing matrix element of $\langle\phi_1|V|\phi_2\rangle$. The amount of wavefunction mixing depends on the initial energy separation of the two unperturbed states, $\Delta E_u = (E_2 - E_1)$, and on the magnitude of the mixing matrix element. Small mixing matrix elements can still result in large changes to the energies of the states if the initial separation of the levels is also small. As described by Casten [15], great simplification of the relationship between the unperturbed and perturbed states can be achieved by defining the ratio,

$$R = \frac{\Delta E_u}{V} \tag{2.30}$$

between the unperturbed energy difference and the strength of the mixing matrix element (here, and from this point onwards, V has been used to represent $\langle\phi_1|V|\phi_2\rangle$). In this way the perturbed energies, E_I and E_{II}, of the two states can be represented as,

$$E_I = \frac{1}{2}(E_1 + E_2) - \frac{\Delta E_u}{2}\sqrt{1 + \frac{4}{R^2}} \tag{2.31}$$

and,

$$E_{II} = \frac{1}{2}(E_1 + E_2) + \frac{\Delta E_u}{2}\sqrt{1 + \frac{4}{R^2}} \tag{2.32}$$

The perturbed wave functions of the two states are,

$$\epsilon_I = \alpha\phi_1 + \beta\phi_2 \tag{2.33}$$

and,

$$\epsilon_{II} = -\beta\phi_1 + \alpha\phi_2 \tag{2.34}$$

where

$$\beta = \frac{1}{\left[1 + \left[\frac{R}{2} + \sqrt{1 + \frac{R^2}{4}}\right]^2\right]} \tag{2.35}$$

and, $\alpha^2 + \beta^2 = 1$.

Two states which can mix and approach each other as a function of some structure effect (i.e. deformation) will never actually cross. They will repel each other and never get closer than twice the mixing matrix element. The point at which the states are the

Figure 2.5: *Schematic representation of axially symmetric nuclear shapes [51].*

closest is known as the *inflection point* and after this point the states move away from each other again. The wave functions following the inflection point will be dominated by the unperterbed wave function of the other state. This *non-crossing* of the states is so called because states which do not mix would have maintained their trajectories and crossed each other at the inflection point.

The situation of multistate mixing can be treated as a series of two-state mixings. If there are N degenerate states which can all mix with equal matrix elements then the net result will be a lowering of one state by $(N-1)V$, and a raising of each other state by V. The wave function of the lowered state will be completely mixed so that

$$\epsilon_{lowered} = \sum_{i=1}^{N} \frac{1}{\sqrt{N}} \phi_i \tag{2.36}$$

2.5 Deformation and Nuclear Shapes

At and around closed shells, nuclei in their ground states assume a spherical shape. As we move away from these regions, interactions and mixing between single-particle orbitals lead to shell gaps appearing away from sphericity. This leads to many nuclei having a non-spherical ground state [52, 53]. The volume of a sphere of radius, R_0, is

$$V = \frac{4}{3}\pi R_0^3 \tag{2.37}$$

The surface of a deformed shape of the same volume, V, can be described by the radius pointing vector, R, from the origin to the surface [42] as

$$R = R(\theta, \phi) = R_0 \left(1 + \alpha_{00} + \sum_{\lambda=1}^{\infty} \sum_{\mu=-\lambda}^{\lambda} \alpha^*_{\lambda\mu} Y_{\lambda\mu}(\theta, \phi) \right) \tag{2.38}$$

where α_{00} is a constant describing the changes in the nuclear volume [42],

$$\alpha_{00} = -\frac{1}{4\pi} \sum_{\lambda \geq 1, \mu} |\alpha_{\lambda\mu}|^2, \tag{2.39}$$

and $\alpha_{\lambda\mu}$ are the expansion coefficients for the spherical harmonics, $Y_{\lambda\mu}$, of order λ. The expansion coefficients for quadrupole deformation ($\lambda = 2$) can be written in Hill-Wheeler [54] coordinates as

$$\alpha_{20} = \beta_2 \cos\gamma \tag{2.40}$$

$$\alpha_{22} = \frac{1}{\sqrt{2}} \beta_2 \sin\gamma \tag{2.41}$$

Higher order shapes are also possible such as octupole ($\lambda = 3$) and hexadecapole ($\lambda = 4$).

Deformed nuclei are often described as oblate (flattened sphere) or prolate (rugby ball) depending on whether the value of β is negative or positive (see figure 2.5). Nuclei of an intermediate shape with three principal axes having different radii can be described as triaxial.

2.5.1 Angular Momentum Quantum Numbers

The total angular momentum, j, of a nucleon is equal to the vector sum of its orbital angular momentum, l, and the intrinsic spin, s. When the nucleon is orbiting in an axially symmetric deformed potential it is possible to describe these quanta in terms of their projections onto the symmetry axis. The projections of a single nucleon's orbital angular momentum and intrinsic spin are labelled Λ and Σ respectively and the sum of these two values gives the projection of the total angular momentum, Ω. The K quantum number is the projection of the total angular momentum along the symmetry axis of all single particle angular momenta plus the rotational angular momentum of the nucleus as a whole, R. Figure 2.6 illustrates these relationships.

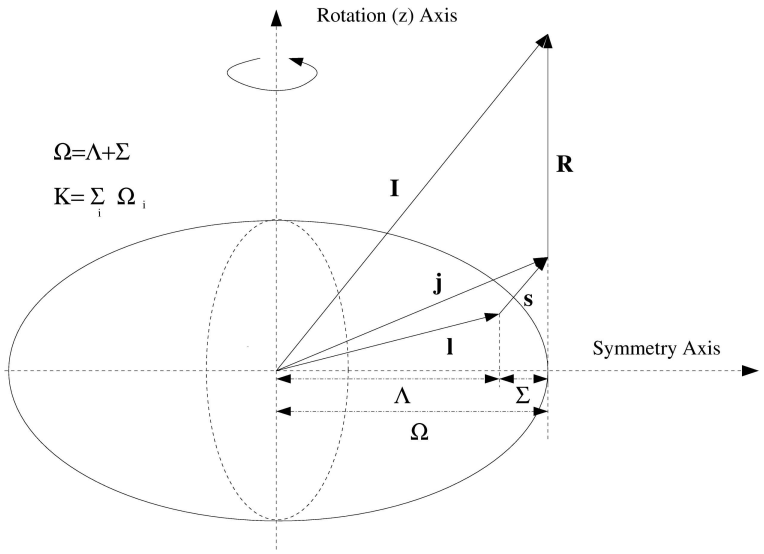

Figure 2.6: *Schematic representation of the quantum numbers associated with an axially symmetric deformed nucleus. Taken from reference [55].*

2.6 The Nilsson Model

The Nilsson model [56] is a shell model based in a deformed potential. The introduction of a deformed potential changes the picture of the nucleus profoundly. The potential is no longer symmetric about all axes therefore each orbital can be described according to its orientation with respect to the symmetry axis. In fact each j orbital also undergoes a splitting of its magnetic substates so that each individual substate has an orbital plane at a different angle to the symmetry axis (figure 2.7). These magnetic substates can be labelled by the value of their angular momentum projections along the symmetry axis, K. The energy of a nucleon in one of these orbitals will in part depend on the angle of that orbital, θ, which is approximatly equal to $\sin^{-1}(K/\boldsymbol{j})$. If the orbital motion is close to the bulk of the nuclear matter, with a small value of Ω, then the energy of the nucleon will be much lower than when in an orbital with a large angular momentum projection so that the nucleon is orbiting further away from the rest of the nucleons. The difference in energy between each magnetic substate orbital will increase as a function of the deformation, β. The energy of each magnetic substate will be affected by any orbitals in the vicinity which have the same value of K (recall section 2.4.4 on two-state mixing). It is with these considerations that the Nilsson diagram may be constructed to plot the evolution in energy of the nuclear orbitals with respect to deformation, figure 2.8 (taken from reference [57]).

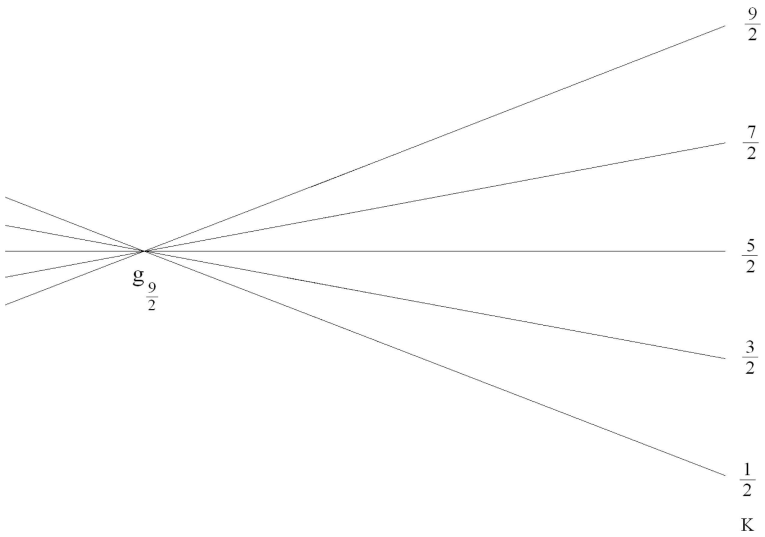

Figure 2.7: *The angular splitting of a $g_{9/2}$ state into its individual magnetic substates in a deformed potential. Adapted from reference [15].*

Each of the Nilsson orbitals can be labelled with a unique set of quantum numbers. The naming system takes the form of,

$$K^{\pi}[Nn_z\Lambda] \tag{2.42}$$

where K is the projection of the angular momentum onto the symmetry axis, π is the parity of the orbital, N is the principal quantum number indicating which major oscillator shell the orbital originates from, n_z is the number of nodes in the wave function in the direction of the symmetry axis, and Λ is the orbital angular momentum projection along the symmetry axis. The value of K equals $\Lambda \pm \Sigma$ (where $\Sigma = \frac{1}{2}$) depending on the alignment of the intrinsic angular momentum.

In the axially deformed picture it would be expected that a rotational band be built on each of these intrinsic states. The energies of the excited states in a rotational band built on a state of angular momentum K relative to the energy of the band head can be described as [15],

$$E_{rot}(J) = \frac{\hbar^2}{2\jmath}[J(J+1) - K(K+1)] \tag{2.43}$$

where J is the angular momentum of the state, and $\jmath$ is the moment of inertia.

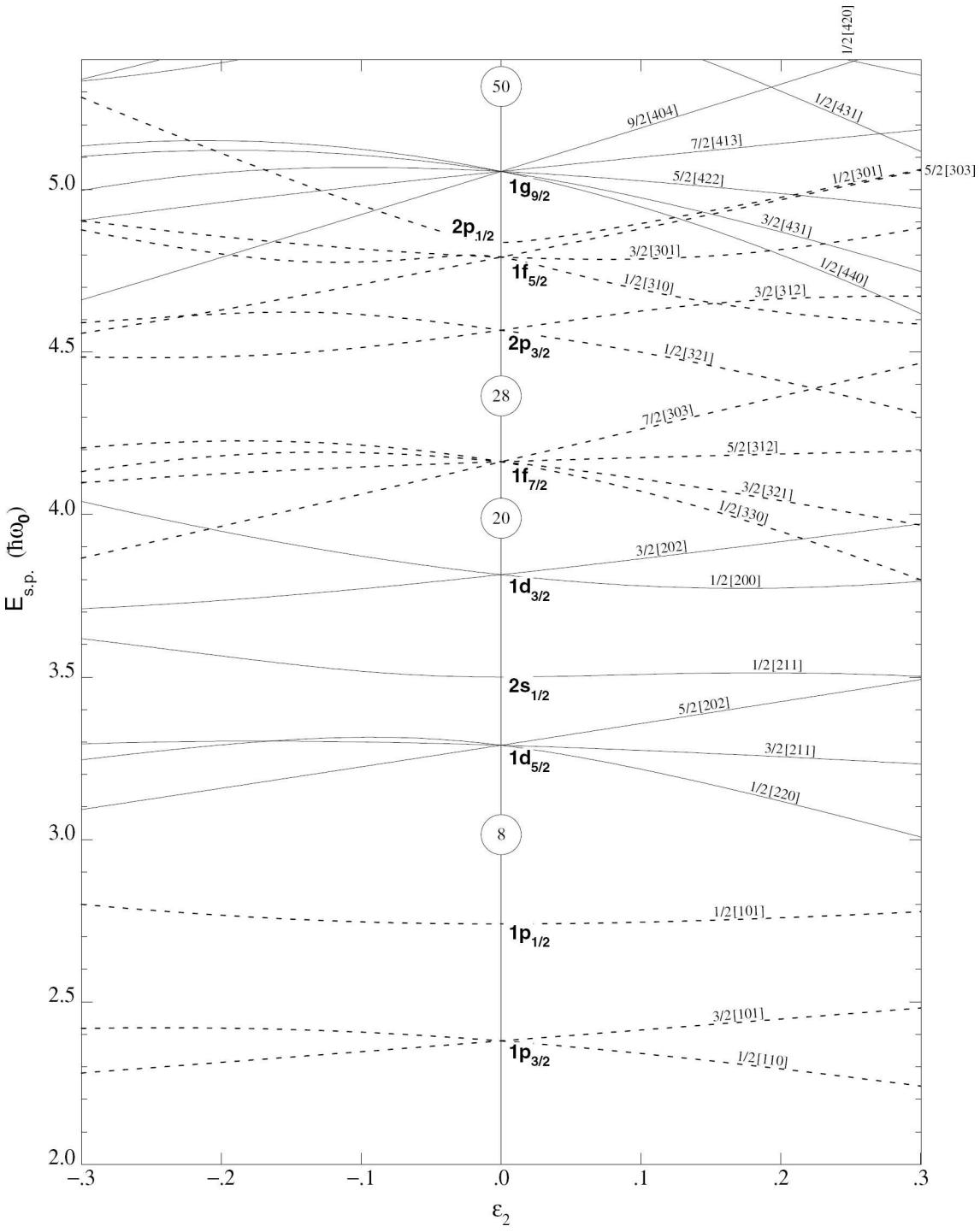

Figure 2.8: *Nilsson diagram for protons or neutrons, Z, $N \leq 50$ ($\epsilon_4 = 0$). Taken from reference [57].*

2.7 BCS Calculations

In 1957 a method of explaining superconductivity in metals as a macroscopic quantum effect was worked out by J. Bardeen, L. Cooper and R. Schrieffer. The theory was named BCS theory [58, 59] and proposes that conduction band electrons of opposite spins in the metal are forced, by interactions with the highly polarized ion lattice, to form Cooper pairs. The Pauli exclusion principle prevents fermions (electrons) from occupying the same quantum state so at low temperature all the states are filled to the Fermi surface. If the fermions form Cooper pairs they may act as bosons and, instead of being bound by the Pauli principle, can form a Bose-Einstein condensate allowing the system to achieve a much lower energy.

Protons and neutrons are also fermions and it has been found that BCS theory can be used to describe multi-quasiparticle configurations in nuclei [60]. The moment of inertia, $\jmath$, of a nuclear ground state is lower than would be expected for a rigid rotor where all the nucleons act independently of each other. This lower moment of inertia is explained by the superfluid nature of the nucleus. As in superconducting metals, the superfluidity is lost as the pairing of fermions breaks down. This occurs in nuclei with an increase in the internal energy or as the rotational frequency is increased [61]. In the case of rotation, as the pairs are broken the angular momenta of the individual nucleons align with the rotation vector, $\mathbf{I}$, and increase the moment of inertia towards that of a rigid body.

2.7.1 Projected Shell Model

The Projected Shell Model (PSM) [62, 63, 64] is a shell model calculation in which the model space is built in a deformed basis. This allows large truncations of the model space by only selecting the important quasi-particle states near the Fermi surface. Such large truncations mean the PSM can be used for nuclei which, in standard shell model calculations, would require an impossibly large valence space.

The approach taken by the PSM is to calculate quasi-particle states using a BCS approach in a deformed Nilsson + BCS vacuum $|\phi\rangle$. Projections are then applied to restore rotational symmetry by forming a spherical basis in the laboratory frame. The final step is a diagonalization of the Hamiltonian in this spherical basis.

The quasiparticle configurations for various systems in the PSM are [62, 65]

$$\begin{aligned} &\text{Doubly even nucleus} \quad : \quad |0\rangle,\ a^\dagger_{\nu_1} a^\dagger_{\nu_2}|0\rangle,\ a^\dagger_{\pi_1} a^\dagger_{\pi_2}|0\rangle,\ a^\dagger_{\nu_1} a^\dagger_{\nu_2} a^\dagger_{\pi_1} a^\dagger_{\pi_2}|0\rangle \\ &\text{Doubly odd nucleus} \quad : \quad a^\dagger_\nu a^\dagger_\pi |0\rangle \end{aligned}$$

where $a^\dagger$ are quasiparticle creation operators, ν and π refer to the Nilsson quantum numbers which represent the quasiparticle states near the Fermi surface and $|0\rangle$ is the Nilsson + BCS vacuum or 0-quasiparticle state. The quantum number K is a valid quantum number for these states as axial symmetry is maintained from the Nilsson states. K can therefore be used to label the basis states. The Hamiltonian used in PSM calculations is of separable forces [62]

$$\hat{H} = \hat{H}_0 - \frac{1}{2}\chi \sum_\mu \hat{Q}^\dagger_\mu \hat{Q}_\mu - G_M \hat{P}^\dagger \hat{P} - G_Q \sum_\mu \hat{P}^\dagger_\mu \hat{P}_\mu, \tag{2.44}$$

where $\hat{H}_0$ is the spherical single-particle Hamiltonian including a spin-orbit force, the second term is the quadrupole-quadrupole (Q-Q) interaction, the third and fourth terms are the monopole and quadrupole pairing interactions respectively. Residual neutron-proton interactions have been shown [66] to be essential in PSM calculations for all types of nuclei and is included in the Q-Q term.

The eigenvalue equation for a given spin I is of the form

$$\sum_{\kappa'} \{H^I_{\kappa\kappa'} - E^I N^I_{\kappa\kappa'}\} F^I_{\kappa'} = 0, \tag{2.45}$$

where the Hamiltonian and norm matrix elements are defined by

$$H^I_{\kappa\kappa'} = \langle \Phi_\kappa | \hat{H} \hat{P}^I_{KK'} | \Phi_{\kappa'} \rangle, \ \ N^I_{\kappa\kappa'} = \langle \Phi_\kappa | \hat{P}^I_{KK'} | \Phi_{\kappa'} \rangle \tag{2.46}$$

and $\hat{P}^I_{KK'}$ is the angular-momentum projection operator. The expectation values of the Hamiltonian with respect to a "rotational band κ" $H^I_{\kappa\kappa'}/N^I_{\kappa\kappa'}$ are called the band energies. PSM results are usually interpreted with the aid of a band diagram [62] where the band energies are plotted as a function of spin.

PSM calculations have been peformed for the odd-odd, $N = Z$ nuclei ^{82}Nb and ^{86}Tc. The results are shown and discussed in sections 5.1 and 5.3 respectively.

2.7.2 Potential-Energy-Surface Calculations

A knowledge of the shape of a nucleus is of vital importance to understanding the structural features present. The degree of deformation is essential in determining observable quantities such as quadrupole moments, moments of inertia, band-crossing frequencies and decay properties. The shape and amount of deformation of a nucleus can change with angular momentum and excitation energy so it is important to have a method of calculating the shape for a specific multiquasiparticle configuration. It is for this reason that F.R. Xu [67] has developed configuration-constrained potential-energy-surface calculations which account for the γ degree of freedom.

The calculation proceeds as an iteration for all coordinates of the deformation parameters, β_2 and γ, to find the minimum total energy with respect to the hexadecapole deformation, β_4, for each individual point. The calculation is constrained for a specific multi-quasiparticle configuration in a given nucleus so that the total energy [67] is given by,

$$E_{tot}(\beta_2, \gamma, \beta_4) = E_{LDM} + E_S + E_{LN} \tag{2.47}$$

where there are contributions from a macroscopic term, E_{LDM}, a microscopic term, E_S, and a pairing energy term, E_{LN}. The contribution from the macroscopic term is found using the Liquid-Drop Model (LDM) with the parameters described in reference [68].

A Strutinski shell correction [69, 70] is included as the microscopic term to correct for the increased stability of nuclides observed around magic numbers. In the calculations of F.R. Xu *et al.* the single-particle energy levels are calculated using a non-axially deformed Woods-Saxon potential. The deviation of binding energy around shell boundaries is related to the level density, $\tilde{g}(\varepsilon)$, so that the microscopic term is given by,

$$E_S = -2 \int_{-\infty}^{\mu} \tilde{g}(\varepsilon)\, \varepsilon \, d\varepsilon \tag{2.48}$$

where μ is the Fermi energy and $\tilde{g}(\varepsilon)$ is the mean energy density of single-particle states at energy ϵ.

The pairing term is configuration dependent and uses a process of diabatic blocking to follow specific quasiparticles occupying specific orbitals as the deformation is changed. If an orbital is occupied then it is blocked to other quasiparticles. Orbitals are tracked by examining the expectation values of the approximate quantum numbers $\langle N \rangle$, $\langle n_z \rangle$, $\langle \Lambda \rangle$ and $\langle |\Omega| \rangle$ (see sections 2.5.1 and 2.6), so even if orbitals cross one another the blocking is still handled in the correct manner. In this Lipkin-Nogami treatment of pairing [7, 70] the pairing contribution is given by

$$E_{LN} = \sum_{j=1}^{S} \varepsilon_{k_j} + \sum_{k \neq k_j} 2\upsilon_k^2 \varepsilon_k - \frac{\Delta^2}{G} - G \sum_{k \neq k_j} \upsilon_k^4 + G\frac{(N-S)}{2} - 4\lambda_2 \sum_{k \neq k_j} (u_k \upsilon_k)^2 \quad (2.49)$$

where S is the seniority of the proton and neutron configurations corresponding to the number of orbitals blocked by single particles with index k_j, N is the proton or neutron number and λ_2 is the Lagrange multiplier. This multiplier is a function of u_k and υ_k, and on the monopole pairing strength, G, calculated from the odd-even nuclear mass difference. u_k and υ_k are the probability amplitudes for the k^{th} orbital being occupied or unoccupied by a *pair* of particles respectively so that

$$|\upsilon_k|^2 + |u_k|^2 = 1 \quad (2.50)$$

2.8 Isomeric Nuclear States

Isomeric states are long-lived excited nuclear states (see section 1.2). They can decay by a variety of mechanisms. The most common decay modes of isomeric states in nuclei are gamma-ray emission or beta decay. Several examples of direct proton emission from isomeric states have been observed in neutron-deficient nuclei [6], and there are many cases in the actinide nuclei of isomeric states which undergo spontaneous fission [71].

2.8.1 The Seniority Scheme

The seniority scheme [72, 73] is a method of classifying excited nuclear states by the number of unpaired nucleons involved in the configuration. For example if a $J^\pi = 8^+$ state were formed by the coupling of two $g_{9/2}$ protons then that state would

have a seniority of two (ν=2) as all nucleons are paired to $J^{\pi} = 0^{+}$ except for two. To form states of higher spin it is necessary to break an additional pair of nucleons and increase the seniority. The state with the highest angular momentum of a given seniority is often found to be isomeric due to the de-excitation of the state being via a low-energy transition.

It is worth remembering that the labelling of this class of isomeric states as seniority isomers is perhaps misleading as the value of seniority is not changed in the decay of the isomer. Whereas in the case of most isomers the name indicates the property which is changing.

2.8.2 Shape Isomers

Shape isomers occur when states in a second minimum of the nuclear potential surface are populated. This second mimimum has a different deformation to that of the ground-state mimimum and therefore there is a potential barrier between the two. Decay from these states can take the form of electromagnetic decays to the ground-state band (though hindered by the necessity of tunnelling through the potential barrier); by decaying to a different nucleus via alpha or beta decay; or by fissioning into two or more lighter nuclides. For a detailed review of isomeric states of this type see references [71, 74].

2.8.3 Spin Traps

Spin trap isomeric states occur because of the need to conserve angular momentum. An excited state of high spin can sometimes be formed with a low excitation energy and the only states available for it to decay to have much lower angular momentum. When a nuclear state decays via an electromagnetic transition the amount of nuclear spin removed from the system depends on the selection rules given in section 2.1.3. As a general trend, the larger the change in angular momentum required in a decay, the smaller the probability, and longer the half-life of that transition.

2.8.4 K Isomers

In deformed nuclei intrinsic excited states, and the bands built upon them, can be described by their projection quantum number of angular momentum onto the axis

of symmetry, their value of K (see section 2.5.1). An isomeric state can be formed when the decay from one of these band-head states to a state of lower energy has to accommodate a large change in the angular momentum orientation (large change of K) [75, 76]. This *degree of forbiddenness* can be characterised as $\nu = \Delta K - \lambda$, where λ is the multipole order of the transition and ΔK is the difference in K between in initial and final states.

K-hindrance can be easily destroyed in the presence of K-mixing caused by Coriolis mixing, γ-deformation tunnelling or level density effects. The amount of K-mixing can be quantitativly understood from the *reduced hindrance* [30],

$$f_\nu = (T_{1/2}/T^W_{1/2})^{1/\nu} \tag{2.51}$$

where $T_{1/2}$ is the experimentally measured half-life and $T^W_{1/2}$ is the Weisskopf single-particle estimate. Typical values of f_ν for K-isomers range between $f_\nu = 10$ and 100.

Chapter 3

Experimental Techniques

3.1 Nuclear Reaction Mechanisms

In order to determine if a model of the nucleus is correct requires that we investigate that nucleus experimentally. There are a limited number of nuclear properties that can be measured but each one gives some insight into the behaviour of nuclei. The majority of these properties are measured by observing nuclear decays.

There are two main ways of investigating nuclear decays: studying the decay of naturally occurring radioisotopes, or to produce nuclei in nuclear reactions and measure their decay. The former method greatly limits the number of different nuclei which can be studied as it relies on naturally occurring nuclei. Due to most radioactive decay being via beta or alpha emission these studies are also limited to relatively low-spin states.

Nuclear reactions such as fusion-evaporation [20, 22, 23, 24, 27, 77, 78, 79], projectile fragmentation [80, 81, 82, 83], deep-inelastic collisions [84, 85, 86] and induced-fission can produce many unstable nuclei including very exotic nuclei at the limits of stability [35] and/or to very high angular momentum [79, 87, 88]. Other reactions such as coulomb excitation [89] and pick-up/knock-out reactions [90, 91] can be used in a very controlled manner to extract precise information about the configuration of nuclear states.

3.1.1 Experimental Access to N=Z Nuclei

The odd-odd N=Z nuclei are stable nuclei up to and including $^{14}_{7}N_{7}$, the even-even N=Z nuclei are stable up to $^{40}_{20}Ca_{20}$. Several different types of reactions can be considered to study the N=Z nuclei. These include Fusion-Evaporation [20, 22, 23, 24, 27, 77, 78], Projectile Fragmentation [35, 39, 80, 81, 82, 83, 92, 93, 94] and Single-Particle Transfer [95]. Although the latter is not possible with stable beams and targets for the unstable N=Z nuclei, this mechanism is possible with radioactive beams in inverse kinematics [91]. Fusion-evaporation reactions have been used to study the even-even N=Z nuclei up to $^{88}_{44}Ru_{44}$ [78] and the odd-odd N=Z nuclei up to $^{78}_{39}Y_{39}$ [26]. Experimental access to the odd-odd N=Z nuclei above ^{78}Y is much more difficult due to the N=Z line lying along the proton drip line. It has however been possible to use fusion-evaporation reactions to study $^{94}_{47}Ag_{47}$ and identify beta-decaying, beta-delayed proton emitting and proton-decaying isomeric states [96, 97, 98]. In this case the beta particle and/or proton were used as a tag to identify the extremely weakly populated $p3n$ evaporation reaction channel.

A restriction to just stable beams and targets means the only available fusion-evaporation reaction channel to populate $^{82}_{41}Nb_{41}$, $^{86}_{43}Tc_{43}$, $^{90}_{45}Rh_{45}$ or $^{94}_{47}Ag_{47}$ is the $p3n$ channel. If we take ^{86}Tc as an example, the populating reaction would be ^{58}Ni(^{32}S,$p3n$) and the compound nucleus formed is $^{90}_{44}Ru_{46}$. The single neutron and proton separation energies, S_n and S_p, for ^{90}Ru are 13.870 (590) and 4.750 (360) MeV respectively [4]. Therefore it is much more probable that a proton, rather than a neutron, will be ejected from the compound nucleus. In the situation that the proton and neutron separation energies are similar, neutron evaporation is favoured over proton evaporation due to the effect of the coulomb barrier hindering the emission of protons. The even-even N=Z nuclei on the other hand can be populated via the $2n$ channel which, although the cross sections are small ($\sim 5-10\mu b$ [78]), requires less excitation energy above the coulomb barrier meaning less reaction channels being available and the total fusion cross section being smaller.

An alternative reaction mechanism for studying the heavier N=Z nuclei is projectile fragmentation. Beams of ^{92}Mo [39], ^{106}Cd [92, 93], ^{107}Ag (current work) and ^{112}Sn [35] have been used to study this region. However, the cross sections for the heaviest N=Z nuclei approaching ^{100}Sn fall off dramatically (see experimental cross sections

in Table I of reference [35] or calculated cross sections in section 3.1.2) when many neutrons and few protons have to be removed simultaneously (hot fragmentation).

Many of the heavier N=Z nuclei have no information on their excited states so unambiguous particle identification, consisting of both isobaric *and* isotopic discrimination, is essential for studying these nuclei. One method by which this can be achieved is through the combination of a fragment separator, such as the Fragment Mass Analyzer (FMA) [99], for isobaric identification, and an ionization chamber for element (and therefore isotopic) identification through E, ΔE measurements ($\sim Z$). Alternatively for fusion-evaporation reactions, charged-particle detectors (for example CsI [100] or Si-strip [101] detectors) and neutron detectors [102] can be used to identify what reaction channel has been populated thus identifying the reaction product.

Another identification method could involve a previously identified isomeric state which exists in the nucleus of interest. The gamma decay from this isomeric state can be used as an identification tool [18].

In the current work projectile fragmentation techniques have been used to investigate the internal structure of the heavy odd-odd N=Z nuclei, $^{82}_{41}\mathrm{Nb}_{41}$ and $^{86}_{43}\mathrm{Tc}_{43}$.

3.1.2 Projectile Fragmentation Reactions

Projectile fragmentation reactions happen at large beam energies (tens to hundreds of MeV per nucleon) which means the nuclei are together for the shortest time possible ($\sim 10^{-22}$ s). This length of time is comparable to or less than the orbital period of a single nucleon in the nucleus (the Fermi velocity) so all nucleons are effectively stationary with respect to the incident projectile. It is therefore not unreasonable to describe the first part of the reaction process, known as abrasion, as having no collective component. It is a nucleon-nucleon interaction and the mean field does not play a role. The amount of nuclear matter which interacts (the *participants*) depends only on the overlap of the two nuclei. The other nucleons, those which do not take part in the collision, are known as the *spectators*.

Following the abrasion part of the reaction the beam-like fragment (formed by the spectator nucleons of the beam nucleus) is still travelling at high energy with a velocity similar to that of the primary beam. The spectator nucleons of the target-like fragment remain nearly at rest. These two groups of nucleons are the *pre-fragments* of

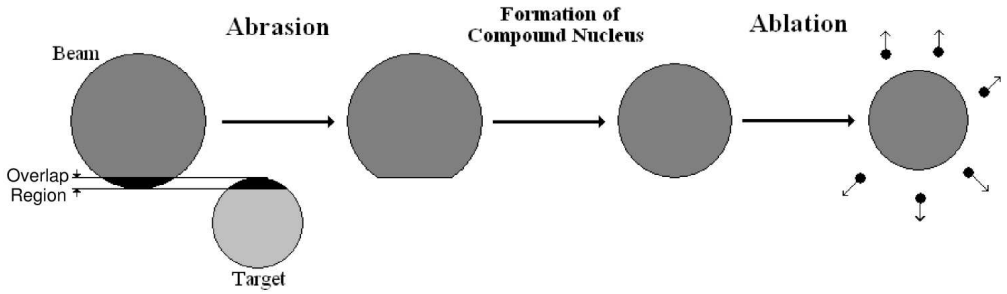

Figure 3.1: *Schematic view of the projectile fragmentation reaction process.*

the reaction and the participant nucleons are removed as a *pre-equilibrium emission*.

The beam-like pre-fragment rearranges its constituent parts in an attempt to compensate for the loss of nucleons. Once a 'compound nucleus' is formed it is in a very hot excited state where particle-evaporation is possible. This second phase of the reaction mechanism is referred to as ablation.

In this fragmentation process it is possible to populate many different nuclear species therefore making it a useful tool with which to investigate the properties of highly exotic nuclei. This geometrical description is shown schematically in figure 3.1 and discussed in further detail in references [103, 104].

EPAX calculations

EPAX is a universal empirical parametrization of fragmentation cross sections developed by Sümmerer and Blank [105]. It is important to remember that these are only calculated total production cross sections and that in considering an actual production rate one must also account for the beam optics and interactions with beam line materials. Such factors are included in simulation programs such as LISE++, described in the following section. Cross sections predicted by the EPAX program for the nuclei of interest in this thesis are displayed in table 3.1.

Fragmentation cross sections fall rapidly as the proton drip line is approached. The removal of each additional neutron reduces the cross section by roughly an order of magnitude as is demonstrated in figure 3.2.

Table 3.1: *Cross sections predicted by EPAX [105] for the fragmentation of a ^{107}Ag primary beam for nuclei of interest to this thesis.*

Nucleus	Cross section (b)
^{94}Pd	1.62×10^{-7}
^{96}Pd	1.98×10^{-5}
^{90}Rh	1.04×10^{-9}
^{93}Ru	1.12×10^{-3}
^{86}Tc	7.28×10^{-9}
^{87}Tc	2.69×10^{-7}
^{88}Tc	5.52×10^{-6}
^{82}Nb	3.03×10^{-8}
^{84}Nb	1.70×10^{-5}

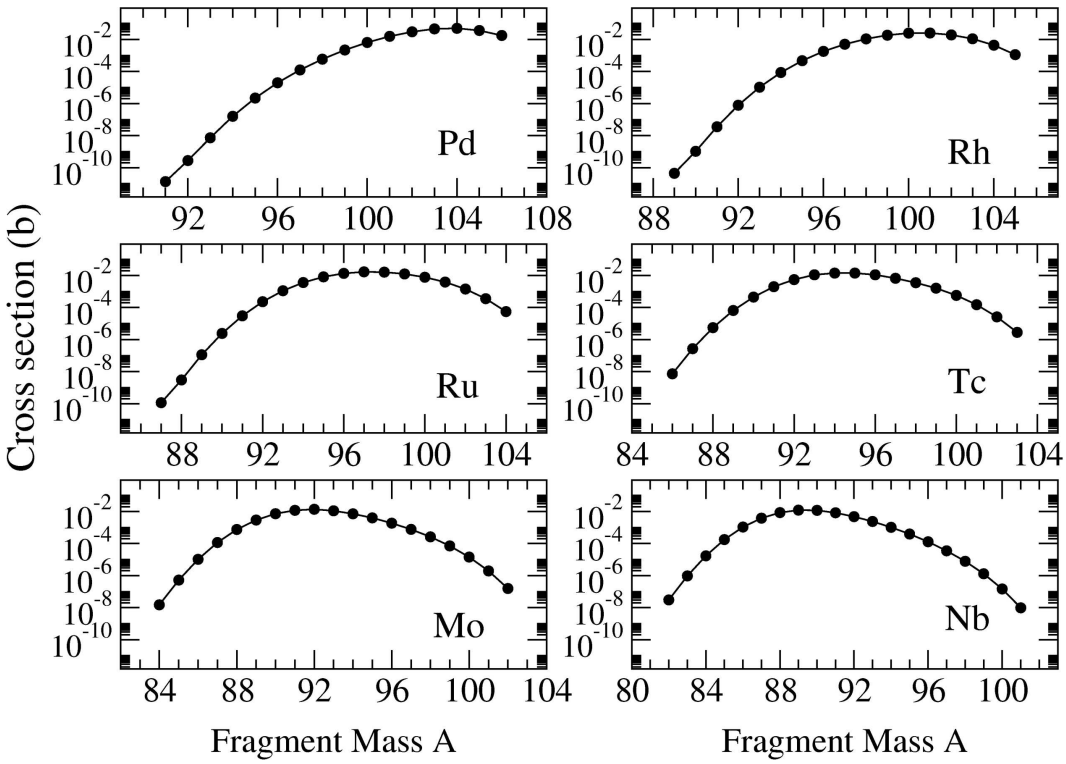

Figure 3.2: *Cross sections of the Pd, Rh, Ru, Tc, Mo and Nb isotopes predicted by the EPAX program [105] for a ^{107}Ag primary beam.*

LISE++ Simulations

The program LISE++ [106, 107] can be used to simulate an experiment involving fragmentation reactions and an electromagnetic spectrometer. The program considers a wide range of phenomena such as nuclear cross sections, ion-optics, energy losses in material, charge-state distributions and separator acceptance effects. Simulations are performed using a Monte Carlo approach to produce plots similar to those of real experimental data for direct comparison. Some examples of simulated data are compared with the current experimental data in section 4.4.

3.2 RISING at GSI

The Rare ISotope INvestigation at GSI (RISING) [108] is a collaboration involving physicists from over 30 institutions and more than 10 countries. The collaboration has run three distinct experimental campaigns between 2004 and 2007. Each campaign utilised relativistic projectile fragmentation (or fission) to produce exotic nuclei and the GSI FRagment Separator (FRS) [109] to identify the reaction products. The Fast Beam RISING campaign [110, 111, 112] focused on identifying prompt gamma-ray decay in exotic nuclei; g-RISING [113] aimed to measure g-factors in exotic nuclei and the Stopped-Beam RISING campaign [114, 115] studied the gamma-ray decay from isomeric states populated in exotic nuclei.

3.3 The GSI Accelerator System

The accelerator system at GSI is comprised of a two step accelerating process. Ions are first accelerated to energies of around 11.5 MeV per nucleon by a linear accelerator, UNILAC. On the way through the UNILAC ions are sequentially stripped of more and more of their electrons by passing through carbon foils. The stripping of atomic electrons from the ions increases the ionic charge and makes the high beam energies possible. Following the UNILAC the beams are then injected into the SIS-18 synchrotron, with a circumference of 216 metres, and further accelerated to relativistic energies. Extracted beams from the SIS-18 synchrotron have a momentum spread ($\delta p = \Delta p/p$) of less than 10^{-3} [109] and can be delivered to many different experimental halls around the GSI complex for numerous types of experiments.

Since 1992 this accelerating system at GSI has been able to provide heavy stable-ion beams from hydrogen to uranium at maximum energies ranging from 1 to 4.5 GeV per nucleon, depending on the mass of the ion. The maximum beam energies are limited by the maximum magnetic rigidity of the SIS-18 synchrotron of 18 Tm. Beam intensities are measured by the number of particles per spill and range from $\sim 10^{11}$ for Ne, to $\sim 10^{9}$ for ^{208}Pb or ^{238}U. Intensities are mainly dependent on the performance of the ion source for a particular nuclear species.

Each beam delivered by this system has an inherent time structure (*spill* structure) which is a result of multiple injections into the SIS-18 synchrotron from the UNILAC accelerator. The extraction time of the beam from the synchrotron can be adjusted to limit the counting rates in sensitive beam-line detectors in an experimental set up. In the current experiment typical spill structures consisted of a 5 second extraction period in a total cycle time of 30 seconds.

3.4 The FRagment Separator

The GSI FRagment Separator (FRS) [109] is a high-resolution magnetic spectrometer designed to separate in mass and nuclear charge the final residue nuclei of the full mass range produced in projectile fragmentation reactions. The spectrometer is a symmetric two-stage device with a dispersive image plane (S2) between the two halves. A schematic diagram of the FRS is shown in figure 3.3. Each stage comprises of two similar magnetic groups of quadrupole and sextupole magnetic groups around a 30° dipole magnet. The dipole magnets provide a magnetic rigidity range from 5 to 18 Tm with a stability of $\sim 10^{-4}$ T. A quadrupole doublet at the entrance or exit to each dipole illuminates the magnetic volume and a triplet set provides the correct optics for the focal planes. Sextupole magnets are also positioned to enable finer adjustments to the optics. The total orbital length of the FRS is $\sim$ 70 m.

The inverse kinematics of this set up means the reaction products enter the FRS with relativistic energies, close to that of the primary beam. The motion of the ions in the magnetic fields of the separator is governed by the Lorentz force so ion trajectories are defined as,

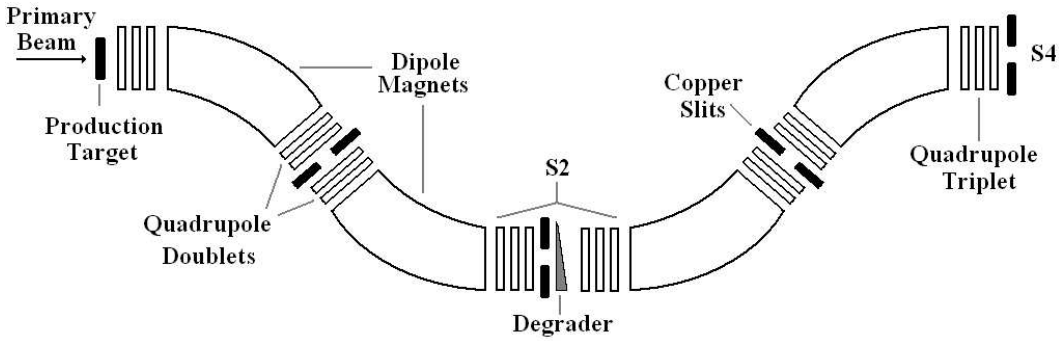

Figure 3.3: *Schematic outline of the FRagment Separator (FRS) at GSI, adapted from figure 7 of reference [109].*

$$B\rho = \frac{p}{qe} = \beta\gamma\frac{m_0}{qe} \approx \beta\gamma c\frac{uA}{qe} \tag{3.1}$$

where B is the magnetic field of the dipole magnets, ρ is the bending radius, p is the momentum of the ion, u is the nuclear mass unit, q is the ionic charge state of the fragment and e is the electric charge (1.6×10^{-19} C). In this experiment the majority of the ions are fully stripped of their electrons therefore $q = Z$.

3.4.1 Beam line Detectors of the FRS

The FRS allows the transmission of multiple species of reaction products to its focal plane, therefore it is vital to achieve unambiguous particle identification of the ions. In the RISING set-up this is done with three types of beam line detector; plastic scintillators [116] for time-of-flight (ToF), transmission ionization chambers [117] for energy loss measurements, ΔE ($\sim Z$), and Multiwire Proportional Chambers [118] for position measurements (necessary for determining the exact path length through the separator). By combining the data collected by these beam line detectors and the magnetic rigidity ($B\rho$) of the dipole magnets, quantities such as the mass to charge ratio, A/q, and the atomic number, Z, can be used to unambiguously identify which nuclear species has arrived at the focal plane. The following section describes the basic principles of each detector type. A schematic of the relative locations of the detectors at the focal plane of the FRS (S4) is shown in figure 3.4.

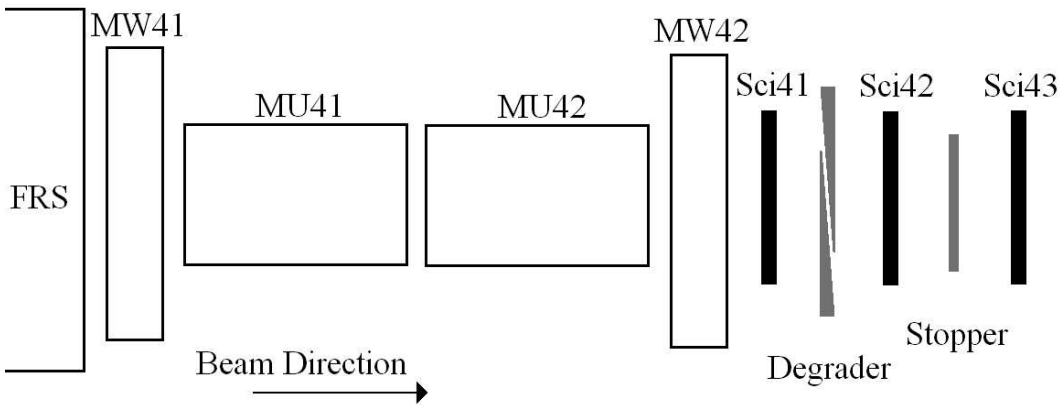

Figure 3.4: *Schematic showing the relative positions of the beam line detectors located at the final focal plane of the FRS (S4).*

Scintillation Detectors

The scintillation detectors of the FRS are used for both time-of-flight measurements and for determining the horizontal position of ions as they pass through the separator. The scintillators consist of a piece of plastic with a photomultiplier tube at each end. When a fragment passes through the plastic the atoms and molecules become excited and emit photons as they deexcite. A special type of plastic (Bicron BC420) is used as it produces a large amount of light per fragment. The light that is emitted is converted to electrons in the two photomultiplier tubes which are positioned to the left and right of the beam direction. The electrons are then multiplied by an avalanche gain and detected. The active region of the plastic covers all of the image plane and the time difference between light collected in the different photomultiplier tubes can be used to determine the position at which the fragment passed through the material.

In the set-up used in the current work there were three scintillators; one positioned at S2 and two at S4 before and after the aluminium degrader. These three scintillators are referred to as Sci21, Sci41 and Sci42 respestively. The signals from the photomultipilers of scintillators 21 (T_{S2}) and 41 (T_{S4}) are used to determine the time-of-flight (ToF) of each ion through the second half of the spectrometer (a distance of $\sim$35 m). The signals start and stop a time-to-amplitude-convertor (TAC) but before

this happens T_{S2} is delayed so that $T_{S2} + T_D > T_{S4}$. The delay is nesessary because the signal from Sci21 must travel through a much longer cable so can sometimes overlap that from Sci41.

A separate TAC is used for the left and right photomultiplier tubes of each detector respectively. The output of each TAC is an analogue signal and is converted to a digital signal by an analogue-to-digital-converter (ADC) resulting in a ToF for both left and right. The measured time-of-flight (ToF^*) is an average time-of-flight of left and right so that,

$$ToF^* = \frac{(ToF_L^* \cdot \alpha_L) + (ToF_R^* \cdot \alpha_R)}{2} = T_{S2} + T_D - T_{S4} \tag{3.2}$$

where α_L and α_R are calibration factors to convert the left and right ToF into nanaoseconds. The true ToF is then equal to,

$$ToF = T_D - ToF^* = T_{S4} - T_{S2} = \frac{d_0}{v} \tag{3.3}$$

where d_0 and v are the path length and velocity of the fragment respectively.

Multiwire Proportional Counters

A MultiWire Proportional Counter (MWPC) [118] consists of a gas-filled chamber with five parallel wire planes (see the schematic in figure 3.5), each holding a different potential. When a heavy ions passes through the gas (which is a mixture of CO_2 and argon) atoms and molecules in the gas are ionized, producing free electrons and positively charged ions. The free electrons drift towards the anode wires and create an avalanche of electrons in the cylindrical electric field. The negative signals in the anode wires induce possitive signals in the nearest x and y cathode wires. A time-to-digital converter (TDC) is started by the anode wire and stopped separately by a signal from each end of the cathode wire. The time difference between these two measured times can be used to determine the position at which the fragment passed through the detector such that,

$$x = \alpha_x(t_{xL} - t_{xR}) + \beta_x,\ y = \alpha_y(t_{yU} - t_{yD}) + \beta_y \tag{3.4}$$

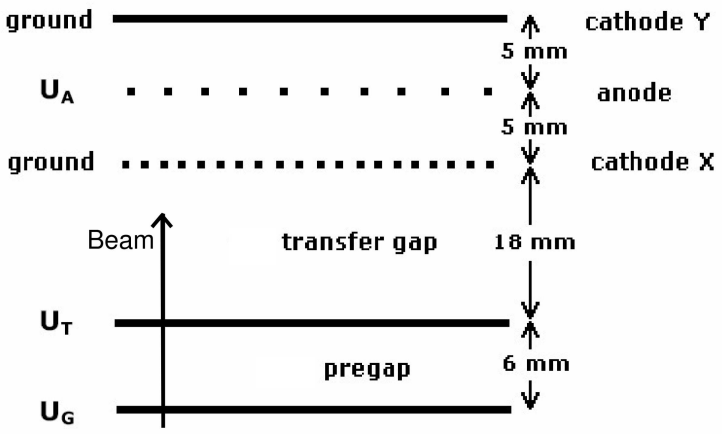

Figure 3.5: *Schematic outline of a MultiWire Proportional Counter (MWPC) taken from reference [119].*

where t_{xL} (t_{yU}) and t_{xR} (t_{yD}) are the times from the x-left and x-right (y-up and y-down) ends of the cathode wires, and α and β are the calibration factors and offsets respectively which translate the signals of the TDC to millimetres.

The anode and cathode wires are constructed of tungsten. They are 20 μm and 50 μm thickness and separated by 2 and 1 mm respectively. The anodes are positioned at 45° to the cathode wires. The cathode wires run both horizontally and vertically with respect to the beam axis to allow the measurements of both x and y positions of passing ions. The active area of the detector is around 20×20 cm.

MWPCs are located at each image plane of the FRS. Those situated in vacuum have windows of 100 μm thick titanium to contain the gas whereas the MWPCs located in air at the final focus have windows made of 25 μm kapton $(C_{22}H_{10}O_5N_2)_n$ which minimises nuclear interactions with passing fragments.

The MWPCs have a disadvantage in that their wire structure introduces inhomogenities in the beam and can destroy the achromaticity of the separator. For this reason the MWPCs in vacuum are only in the beam line during calibrations and removed for the actual experimental measurement. The increased positional sensitivity of a MWPC over that of a scintillator justifies their use during calibrations.

Multi-Sampling Ionization Chambers

A MUltiple-Sampling Ionization Chamber (MUSIC) [117] can be used to determine the nuclear charge, Z, of a fragment passing through it. In the current set-up two

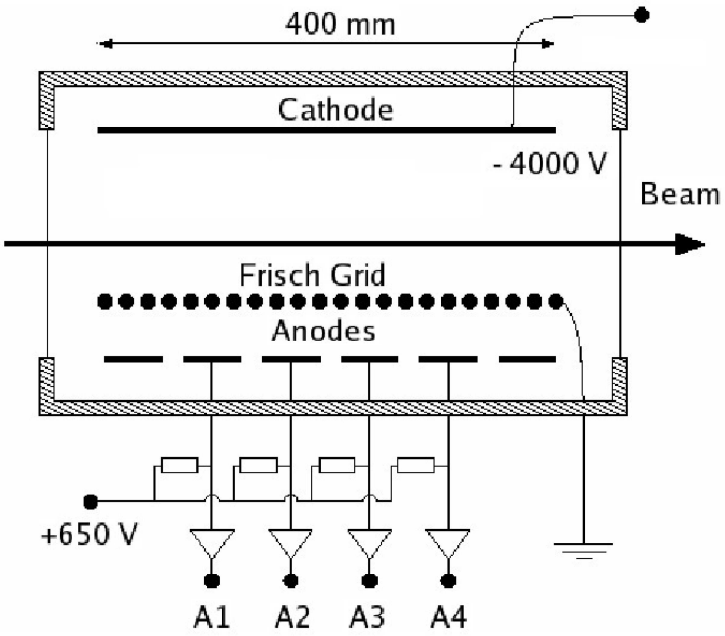

Figure 3.6: *Schematic outline of a MUltiple-Sampling Ionization Chamber (MUSIC) taken from reference [119].*

MUSIC chambers are situated at the final focal plane of the FRS (S4) just upstream of scintillator 41 (that used for the ToF measurement). The MUSIC chambers are MU41 and MU42 and have a Nb stripper positioned between them to ensure the fragments remain fully-stripped of electrons.

The MUSIC is a gas-filled chamber containing P10 gas, a mixture of Ar (90%) and CH_4 (10%) which is constantly pumped through to mantain optimum detection conditions. The 600 mm long chamber has entrance and exit windows of 25 μm thick kapton $(C_{22}H_{10}O_5N_2)_n$ to minimise interactions of fragments. When a fragment passes through the active region, which is 276 x 150 mm^2, gas particles are ionized and free electrons are generated along the trajectory. The electrons (positive ions) drift towards the anodes (cathode) with a velocity of approximately 5 cm/μs (5 cm/ms) under the influence of a homogeneous electric field. The cathode is one single piece of metal but the anode is split into eight sections, each giving an individual signal (see figure 3.6). A Frisch grid is located 23 mm in front of the anodes so the signal is independent of the position of the fragment trajectory.

The charge collected in each anode is converted to a voltage by the preamplifier and used to determine the energy loss (ΔE) of the fragment in the chamber. The

energy loss of a fragment in the MUSIC chamber is related to several properties of the material traversed by the relativistic Bethe-Bloch equation [120] so that

$$-\frac{dE}{dx} = \left(\frac{Z_1 e^2}{4\pi\epsilon_0}\right)^2 \frac{4\pi Z_2 \rho N_A}{A_2 m_e v^2}\left[\ln\left(\frac{2m_e v^2}{I(1-\beta^2)}\right) - \beta^2\right] \tag{3.5}$$

where dx is the distance traversed by a nucleus (fragment) of atomic number Z_1 travelling at velocity v through a material of density ρ with mass and atomic number A_2 and Z_2. N_A, ϵ_0, e and m_e are the Avogadro number, the permittivity of free space, and the electron charge and rest mass respectively. Relatavistic effects are included from $\beta = \frac{v}{c}$.

A manipulation of the arrival times in each anode can also be used to determine the position of the interaction with the gas and therefore the trajectory of each fragment through the MUSIC. This technique can yield a more accurate result than that of the MWPCs ($\sim$0.1 mm compared to $\sim$1 mm) but requires substantially more electronics so was not used in the current work.

3.5 Gamma-ray Spectroscopy

3.5.1 Germanium Detectors

Germanium is an example of a semiconductor which is an excellent material from which to make a radiation detector. In a semiconductor, electrons are confined to two energy bands. These bands are the valence band, in which the electrons are bound to the lattice structure of the crystal, and the conduction band in which electrons are free to move through the crystal. Between these two energy regimes is a forbidden region consisting of energies which the electrons may not possess. In an idealised, pure semiconductor crystal at zero temperature, all the electrons reside in the valence band and this band is fully occupied. With thermal excitation, electrons gain enough energy to cross the forbidden region, the size of which is known as the band gap, into the conduction band. As an electron is promoted into the conduction band a vacancy (hole) is also created in the valence band. The electron and hole act as the charge-carrier in the semiconductor.

The situation so far described in which there is always an equal number of electrons and holes is an ideal picture of an intrinsic (perfect) semiconductor. In reality this is impossible to achieve and the actual number of charge carriers in the crystal is heavily influenced by, if not characterised by, the impurities in the crystal. Germanium is a group IV element and therefore each Ge atom in a lattice forms four covalent bonds with surrounding atoms in the lattice with all electrons involved in a bond. In the intrinsic case there are only Ge atoms present so there are no additional electrons. Two types of impurities can change this situation, group III and group V elements. Group III elements such as boron or group V elements, for example phosphorus, can replace a Ge atom in the lattice. Group III elements form only three covalent bonds with surrounding atoms and therefore there is an additional electron hole added to the lattice. In the case of group V elements an extra electron is added to the system in an attempt to form five covalent bonds. These impurities are known as acceptor (p-type) and donor (n-type) impurities, referring to the acceptance of, or donation of, an electron to the system by the impurity atom. In each case there will be a large imbalance in the numbers of electrons and holes. In p-type semiconductors the holes become the majority carrier and the conductivity of the material is almost entirely dependent on their flow. In n-type semiconductors it is the electrons that are the majority carriers and dominate the electrical properties.

Other impurities in the material can act in a different manner, they can halt the movement of charge carriers in the material. Deep impurities such as zinc or cadmium can accept electrons from the conduction band or holes from the valence band and hold them for some time. This prevents them from contributing to the collected charge and is referred to as charge trapping. An additional role of these deep impurities is to accept both carriers and recombine them, removing the charge carrier from the system. This process is known as recombination.

Charged particles moving through the crystal or photons will also promote electrons into the conduction band, creating a number of electron-hole pairs proportional to the energy of the radiation. In the presence of an applied electric field the charge carriers will migrate through the crystal. The electron and the hole will move with a drift velocity,

$$v_e = \mu_e E \tag{3.6}$$

and

$$v_h = \mu_h E \tag{3.7}$$

respectively, where $\mu_{e(h)}$ represents the mobility of the electron (hole) and E is the magnitude of the applied electric field. Typical mobilities for electrons and holes in hyper-pure germanium detectors at liquid nitrogen temperatures are 4.2×10^4 and 3.6×10^4 cm^2/V.s respectively. If the applied electric field is sufficiently high then the electrons and holes will move with the maximum velocity, known as the saturation velocity. The field required for a hyper-pure germanium crystal is typically a couple of thousand volts, which is easily achievable. The saturation velocity in germanium of around 10^7 cm/s means a charge collection time of less than 10 ns for an average sized detector.

3.5.2 Gamma-ray Interactions in Ge

Gamma rays may interact with matter by means of a number of mechanisms. The most important mechanisms are that of *pair production*, *Compton scattering* and the *photoelectric effect*. The probability that a photon interacts with a material is therefore a combination of the cross sections for each of these processes [121] such that,

$$\sigma_{tot} = \sigma_{Photoelectric} + \sigma_{Compton} + \sigma_{PairProduction} \tag{3.8}$$

where each term is defined in the following sub-sections. The dominance of these different types of interaction change with the energy of the photon, E_γ, and the atomic number, Z, of the material in which the interaction takes place. Figure 3.7 shows this change as a function of E_γ and Z.

When a photon undergoes one of these processes in a Ge detector, momentum is transferred to an atomic electron which is released into the crystal with a large kinetic energy. This high energy electron will create many electron-hole pairs as it moves through the crystal and the charge is collected as has been described above.

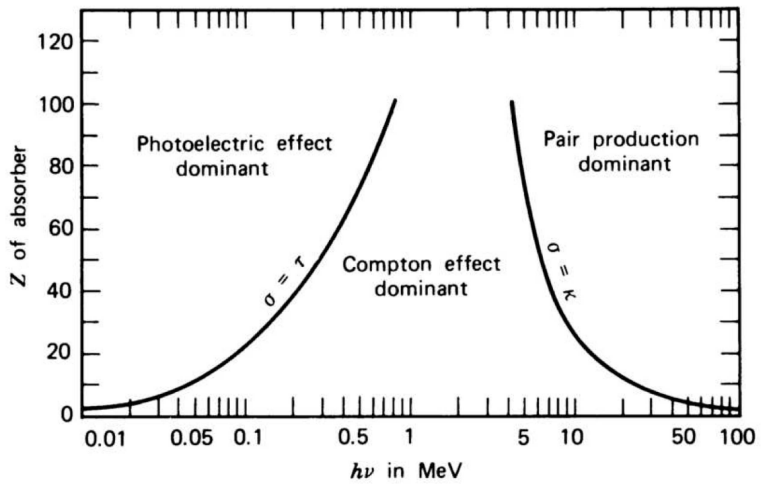

Figure 3.7: *The changing dominance of the main interaction processes of gamma rays in matter as a function of gamma-ray energy and atomic number, Z. The solid lines represent the point at which cross sections are equal. Taken from reference [121].*

The Photoelectric Effect

The most likely interaction process for low energy gamma rays is that of photoelectric absorption. The photon energy is passed entirely to an atomic electron which escapes the parent atom and travels through the material as a free electron (photoelectron) with energy [121],

$$E_{e^-} = h\nu - E_b \tag{3.9}$$

where E_b is the binding energy of the atomic electron, usually from the K shell. The ejection of this atomic electron is followed by the filling of the vacancy left in the K shell by an electron from a higher orbital and the emission of an X ray. In most instances the X ray is reabsorbed into the crystal but if the gamma-ray interaction is close to the surface of the crystal the X ray can sometimes escape causing the collected energy to be less than the gamma-ray energy.

The probability of photoelectric absorption [121] is roughly proportional to

$$\sigma_{Photoelectric} \cong A_{PE}\left(\frac{Z^n}{E_\gamma^{3.5}}\right) \tag{3.10}$$

where A_{PE} is a constant and n varies between 4 and 5 for the gamma-ray energies of interest.

Compton Scattering

When a photon Compton scatters in a material only a proportion of the photon energy of passed to an atomic electron. The photon is scattered from the interaction point, i.e. the direction in which the photon was travelling changes, and the electron is ejected from the atom. The scattering angle and amount of energy transferred is equal to [121],

$$E_\gamma = \frac{E_\gamma^0}{1 + \frac{E_\gamma^0}{m_0 c^2}\left[1 - \cos\theta\right]} \tag{3.11}$$

where E_γ^0 is the energy of the incident photon, m_0c^2 is the rest-mass energy of the electron (511 keV) and θ is the angle between the incident and scattered path of the photon.

The probability for the photon to scatter at an angle θ into the solid angle $d\Omega$ is governed by the *Klein-Nishina formula* for the differential cross section [121],

$$\frac{d\sigma}{d\Omega} = Z r_0^2 \left(\frac{1}{1+\alpha(1-\cos\theta)}\right)^2 \left(\frac{1+\cos^2\theta}{2}\right)\left(1 + \frac{\alpha^2(1-\cos\theta)^2}{(1+\cos^2\theta)[1+\alpha(1-\cos\theta)]}\right) \tag{3.12}$$

where α is the photon energy in units of the electron rest mass ($\alpha = E_\gamma/m_0c^2$) and r_0 is the classical electron radius. The cross section for a Compton scatter at any angle is dependent only on the energy of the photon and the atomic number, Z, of the material so that [122],

$$\sigma_{Compton} = A_{CS}\left(\frac{Z}{E}\right) \tag{3.13}$$

where A_{CS} is a constant.

Pair Production

Pair production is less important for most gamma-ray spectroscopy purposes as it can only takes place above the threshold energy of twice the rest mass of the electron (1022 keV) and the probability of pair production is not significant until the photon energy is several MeV. In the process of pair production, which can only take place in the coulomb field of a nucleus, the photon spontaneously changes into an electron and positron pair. The positron soon annihilates in the absorbing material accompanied by the emission of two 511 keV gamma rays. The cross section for pair production is given by [122],

$$\sigma_{PairProduction} = A_{PP}Z^2 \ln(E) - A_{PP}Z^2 \ln(1022 \text{ keV}) \tag{3.14}$$

where A_{PP} is a constant and the second term explicitly defines the threshold energy of two electron rest masses.

3.5.3 The Stopped RISING Array

The Stopped RISING array incorporates fifteen Germanium Cluster detectors, each with seven large volume crystals, in a high-efficiency arrangement [114]. A photograph of the array is shown in figure 3.8 coupled to the FRS. Photographs of the array open, closed and with the 7 mm perspex stopper mounted are shown in figures 3.9, 3.10 and 3.11 respectively.

The Cluster detectors [114, 123, 124] used in the array comprise seven hexagonical germanium crystals closely packed into a single cryostat. The advantage of grouping crystals is that the seven crystals can act as one large volume detector. Events in which gamma rays Compton scatter between individual crystals in the Cluster can be reconstructed using addback routines to increase the efficiency of the Cluster to much more than is achieved by single crystal detectors. This technique for the Stopped RISING array is outlined in section 4.7.4.

The detectors are arranged into three angular rings of five clusters each at 51, 90 and 129 degrees to the secondary beam axis. The average distance between the face of each detector and the central focus of the array is approximately 22 cm. This arrangement gives a measured photopeak efficiency of around 15% at 661 keV and up to 40% at 80 keV [114].

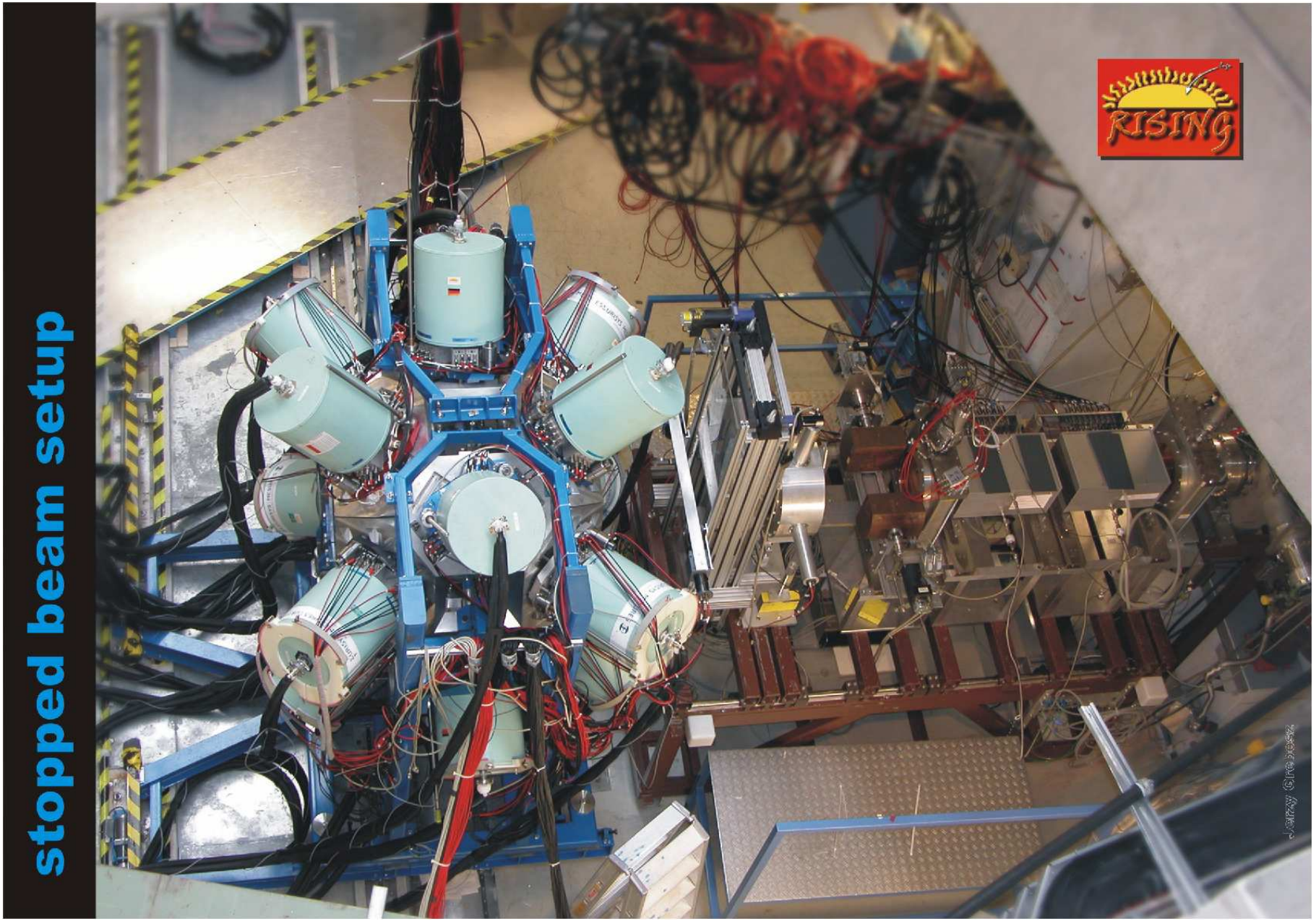

Figure 3.8: *Photograph of the Stopped RISING array coupled to the RISING beam line at the focal plane of the FRS.*

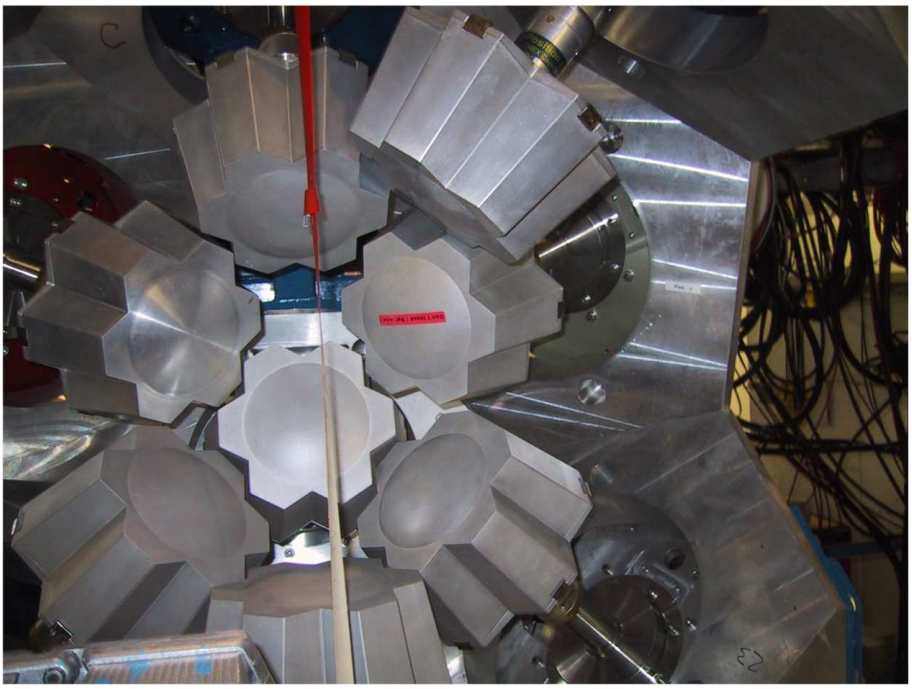

Figure 3.9: *Photograph of one hemisphere of the Stopped RISING array.*

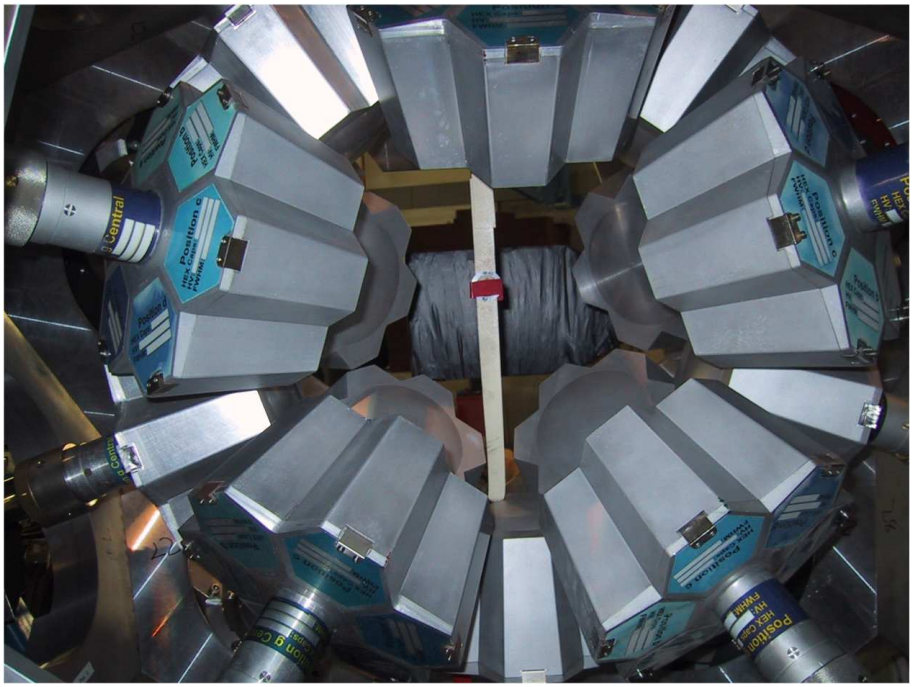

Figure 3.10: *Photograph of the Stopped RISING array with a source at the centre.*

Figure 3.11: *Photograph of the Stopped RISING array with the 7 mm perspex stopper mounted in the centre. In the foreground can be seen the veto detector, scintillator 43 (black object to the left).*

XIA DGF4 digital modules are used to process the signals recorded by the germanium detectors. The DGF module produces an energy and a time signal with a time resolution of 25 ns. Two additional analogue timing signals are produced by short-range (SR) and long-range (LR) TDCs. These TDCs have 0.293 ns resolution in a total recording period of 850 ns, and 1 ns resolution in a total recording period of 140 us respectively.

The efficiency response of the array is shown in figure 3.12 for data collected with a source of ^{133}Ba and ^{60}Co. Further details of the array and determination of the efficiency can be found in reference [114].

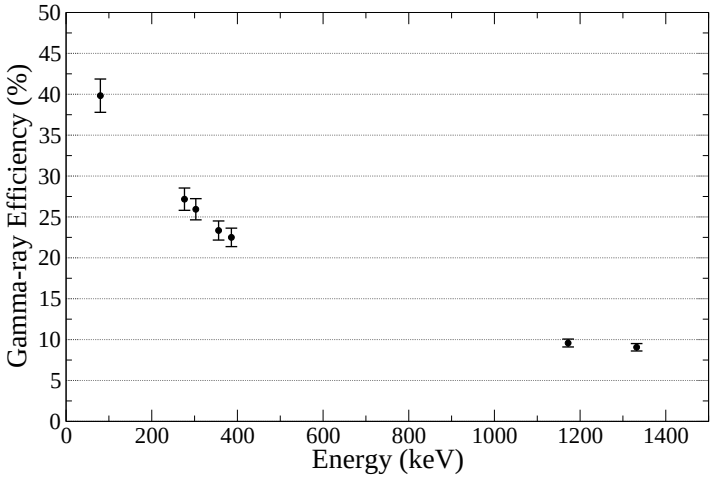

Figure 3.12: *The gamma-ray photopeak efficiency response of the Stopped RISING array determined using ^{133}Ba and ^{60}Co source data. Taken from reference [114]*

Chapter 4

Data Analysis

4.1 Experimental Details

The data described in this thesis were obtained from the first RISING Stopped-Beam experiment [125, 126] which took place in February 2006. During the experiment a beam of ^{107}Ag was accelerated to 750 MeV per nucleon by the SIS-18 Synchrotron and made to impinge on a 4 g/cm^2 Be target. The reaction products were transported to the focal plane of the FRS and each ion was unambiguously identified on an event by event basis. The particle identification methods used are outlined in section 3.4. The ions were slowed down from relativistic energies by passing through an aluminium degrader (S4 degrader) of variable thickness and implanted in a multilayer 7 mm thick perspex block (passive stopper) at the centre of the Stopped RISING germanium detector array.

The primary aim of this experiment was to confirm the existence of an isomeric state in the $N = Z$ nucleus, ^{86}Tc and gain insight into the nature of the low-lying structure. In addition there would be a search for previously unobserved isomers in the region and specifically information about the neighbouring odd-odd, $N = Z$ nuclei, $^{82}_{41}\mathrm{Nb}_{41}$ and $^{90}_{45}\mathrm{Rh}_{45}$.

At several times during the experiment the magnetic fields of the dipole magnets were changed to focus on the nuclei of interest and maximise the transmission of those ions to the focal plane of the FRS. Copper slits were used to limit the range of ions reaching the focal plane. Settings centred on ^{96}Pd, ^{90}Rh, ^{86}Tc and ^{82}Nb. The spill structures employed during the various settings are shown in table 4.1. The magnetic field strengths of the dipole magnets and the thickness of the S4 degrader are shown

Table 4.1: *Spill structures of the various FRS settings.*

Nucleus of central transmission	Ions per spill	Extraction length (s)
^{96}Pd	4×10^{6}	10
^{90}Rh	2-3$\times10^{9}$	6
^{86}Tc	1-3$\times10^{9}$	5-6
^{82}Nb	2×10^{9}	5

Table 4.2: *Magnetic field settings of the Dipole magnets of the FRS used in the different settings of the experiment.*

Nucleus of central transmission	D1 (T)	D2 (T)	D3 (T)	D4 (T)	S4 Degrader thickness (mg/cm^2)
^{96}Pd	0.73085	0.73284	0.54660	0.54910	1900
^{90}Rh	0.70210	0.70420	0.51880	0.52090	1500
^{86}Tc	0.70015	0.70214	0.52920	0.53150	1900
^{82}Nb	0.70240	0.70460	0.54170	0.54400	2400

in table 4.2. The region of nuclei populated and transmitted to the FRS focal plane in each setting are indicated in figures 4.1 and 4.2.

4.2 Improving the Cleanliness of the Particle Identification

A basic particle identification can be made assuming that the amount of energy loss in the first music chamber, $\Delta E1$, is proportional to the atomic number, Z, of the ion, and that the time-of-flight (ToF) between S2 and S4 together with the magnetic rigidity, $B\rho$, can give a rudimentery A/q value. This identification is usually sufficient to decide whether or not that particular nuclear species is being created (and can be observed) in the reaction and indeed that the settings are correct to transport the maximum amount to the final focus of the FRS. This identification will also be sufficient to correlate gamma-ray decay of strongly populated isomeric states to specfic nuclear

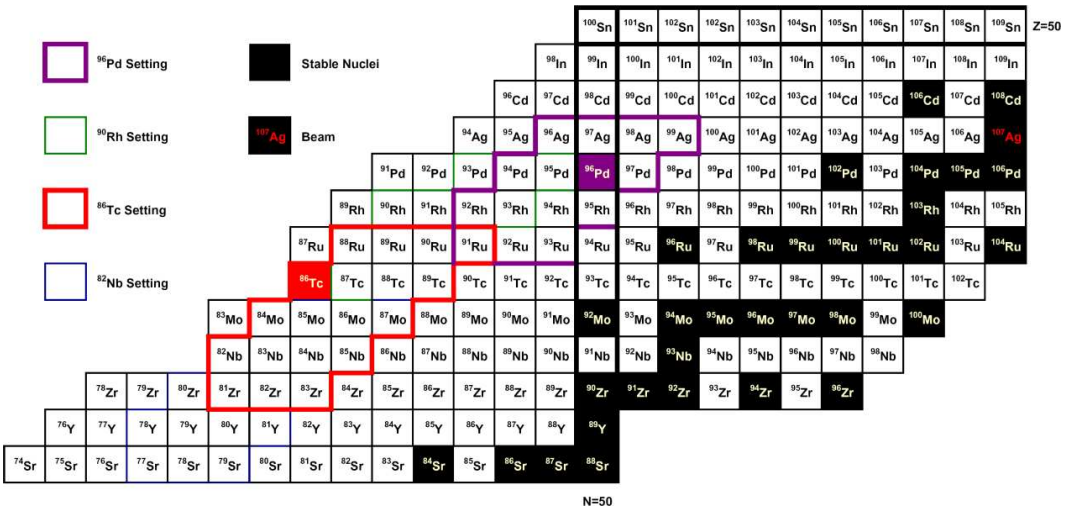

Figure 4.1: *Chart of the nuclides indicating the regions of nuclei populated and transmitted to the FRS focal plane in the* ^{96}Pd *and* ^{86}Tc *settings.*

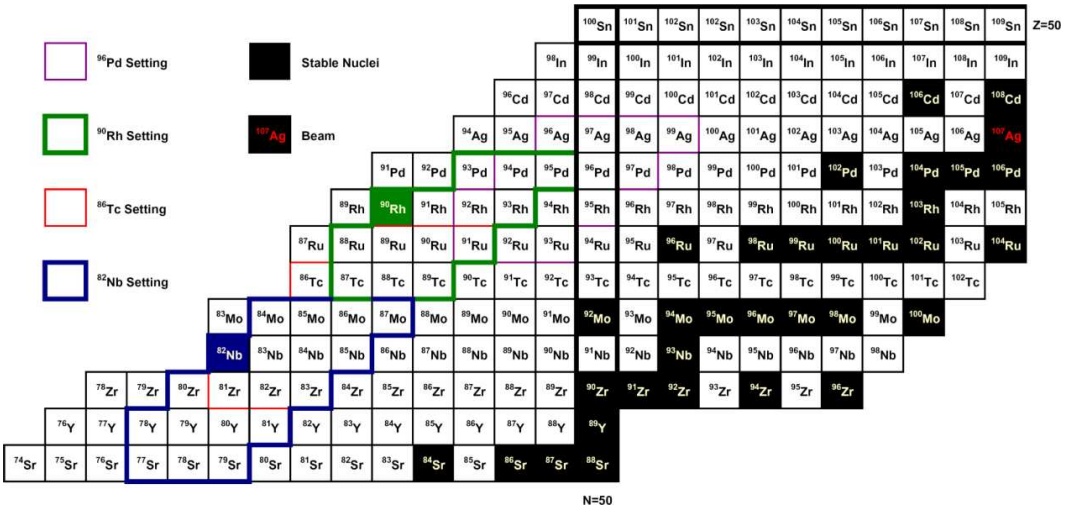

Figure 4.2: *Chart of the nuclides indicating the regions of nuclei populated and transmitted to the FRS focal plane in the* ^{90}Rh *and* ^{82}Nb *settings.*

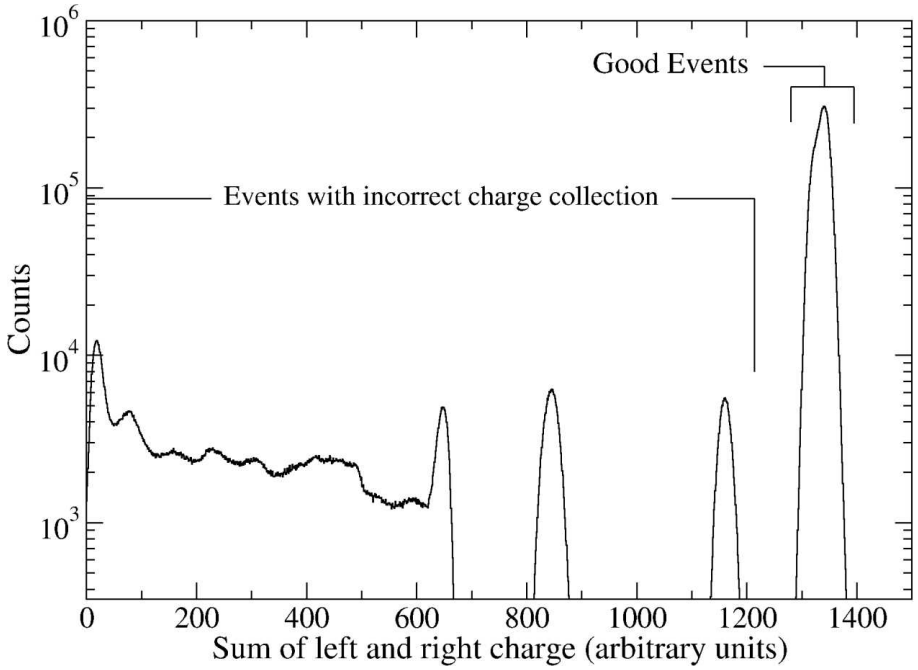

Figure 4.3: *A plot of the sum of the charges collected in the left and right photomultiplier tubes of the Multiwire 41 detector.*

species. However, the aim of the experiment was to observe gamma-ray decays from isomeric states in the most exotic and weakly populated channels. To make this task possible the identification had to be improved to remove any contamination from other nuclei.

The following section will describe several methods in which the data used for particle identification have been corrected for higher order effects and the particle identification improved.

4.2.1 MultiWire Proportional Counters

The passage of a fragment through a MWPC ionizes the gas in the detector and produces electrons. At the same time delta electrons created by interactions of the fragment with other beam line materials may enter the detector. Although the energy deposited by delta electrons is low compared to a fragment traversing the detector if enough delta electrons are created they can cause the illusion of multiple fragments passing through the detector. The situation in which this happens can be identified by examining a plot of the sum of the left and right (up and down) position data. The sum in a single-hit event should be a constant (see figure 4.3) and equal to the dimensions

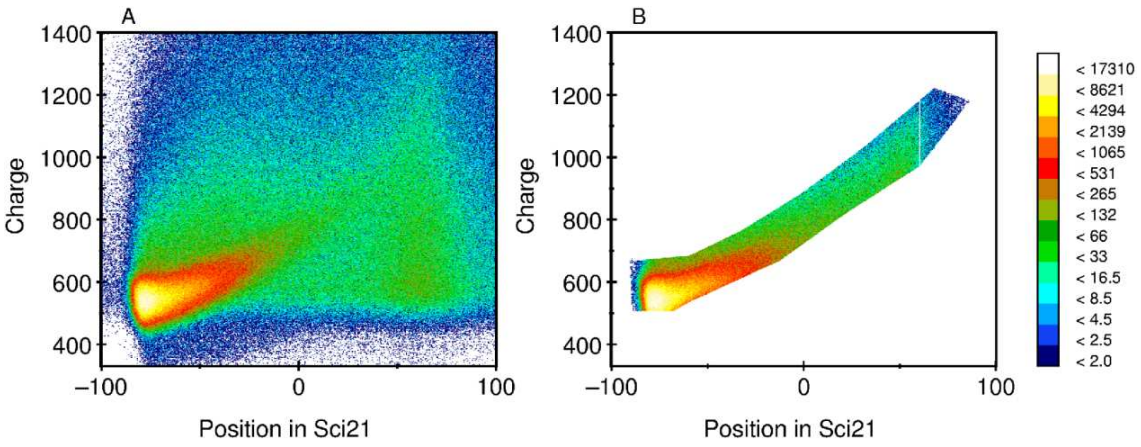

Figure 4.4: **A:** *Ungated plot of charge collected in the left photomultiplier tube of scintillator 21 plotted against the position in scintillator 21.* **B:** *Plot A gated on a correct relationship between collected charge and position. Note the axes are in arbitrary units.*

of the detector (∼20 cm). An event registering multiple hits in the multiwire will show up as a sum of less than this constant and should be vetoed. The chance of multiple hits being recorded increases with beam intensity and can be treated as an efficiency of the MWPC.

4.2.2 Scintillator 21 Charge Collection

In some events in this experiment there was an incorrect relationship between the charge collection in the photomultiplier tube of scintillator 21 and the position measurement given by the scintillator. Scintillator 21 was located in the central dispersive plane of the FRS between the second and third dipole magnets (see figure 3.3) and was used in conjunction with scintillator 41 to determine the time-of-flight of ions through the second part of the separator. The plot to the left of figure 4.4 (4.5) shows the raw charge collected in the scintillator plotted against the position in the scintillator for the left (right) photomultiplier tube. The relationship should be a single line diagonally across the plot. The right side of these same figures show the plots after software gates have been applied to demand a correct relationship between charge and position.

Demanding a correct relationship between the charge collected in the photomultiplier tubes and position of scintillator 21 has a dramatic effect on the identification plots. Figures 4.6 and 4.7 shows the effect of this gating on plots of Z vs ToF and the

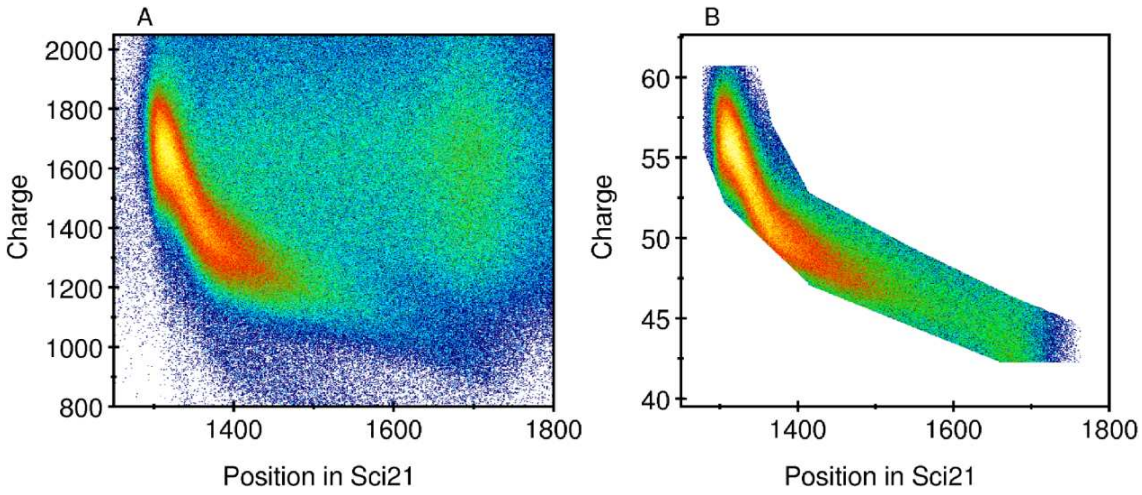

Figure 4.5: **A:** *Ungated plot of charge collected in the right photomultiplier tube of scintillator 21 plotted against the position in scintillator 21.* **B:** *Plot A gated on a correct relationship between collected charge and position. Note the axes are in arbitrary units.*

position at S2 of $Z = 43$ ions vs ToF.

The statistics which are lost in this gating technique can be recovered with a plot of position at S2 vs ToF and demanding a bad relationship between charge and position in scintillator 21. Plot **C** of figure 4.7 shows that a distinction can still be made between the different ion species.

4.2.3 Energy Loss in the Degrader

The majority of ions which pass through the FRS are fully stripped of their electrons. However other charge states can exist and be transported to the focus position. The charge state of the ions can also change through the exchange of one or more electrons as the ions pass through material, such as the degrader at the S2 position.

The energy loss in the degrader at S2 can be calculated from the magnetic rigidity of the magnets in the first (D1 and D2) and second (D3 and D4) half of the FRS. If this quantity is plotted against ToF there is a clear distinction between different charge states, and events in which the charge state has changed in transit.

In the current experiment the majority of the ions are fully-stripped. The program Global [127] predicts only 1.59% of fragments are not fully stripped of their electrons. This small quantity means this effect can be neglected in the current work but is very

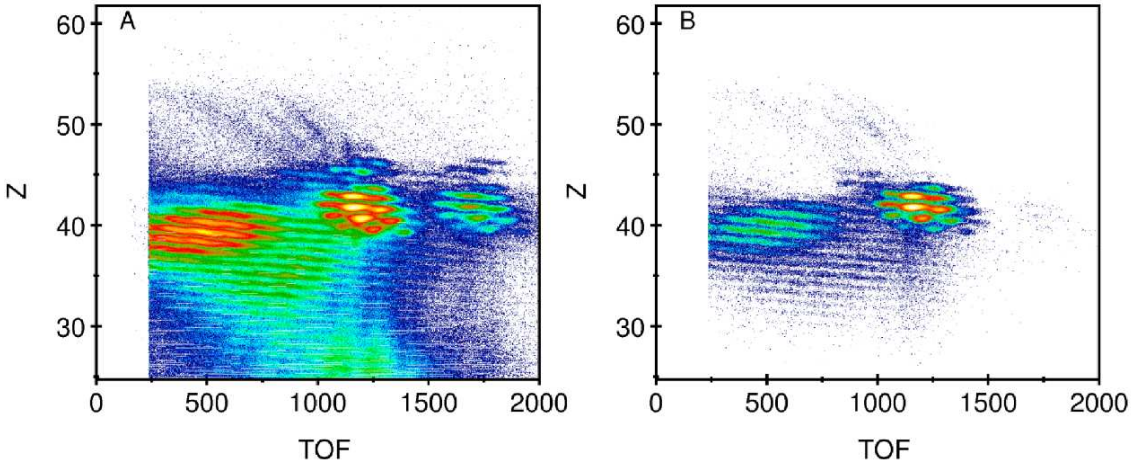

Figure 4.6: **A:** *Ungated plot of Z vs ToF.* **B:** *Same as A, now gated on a correct relationship between collected charge and position.*

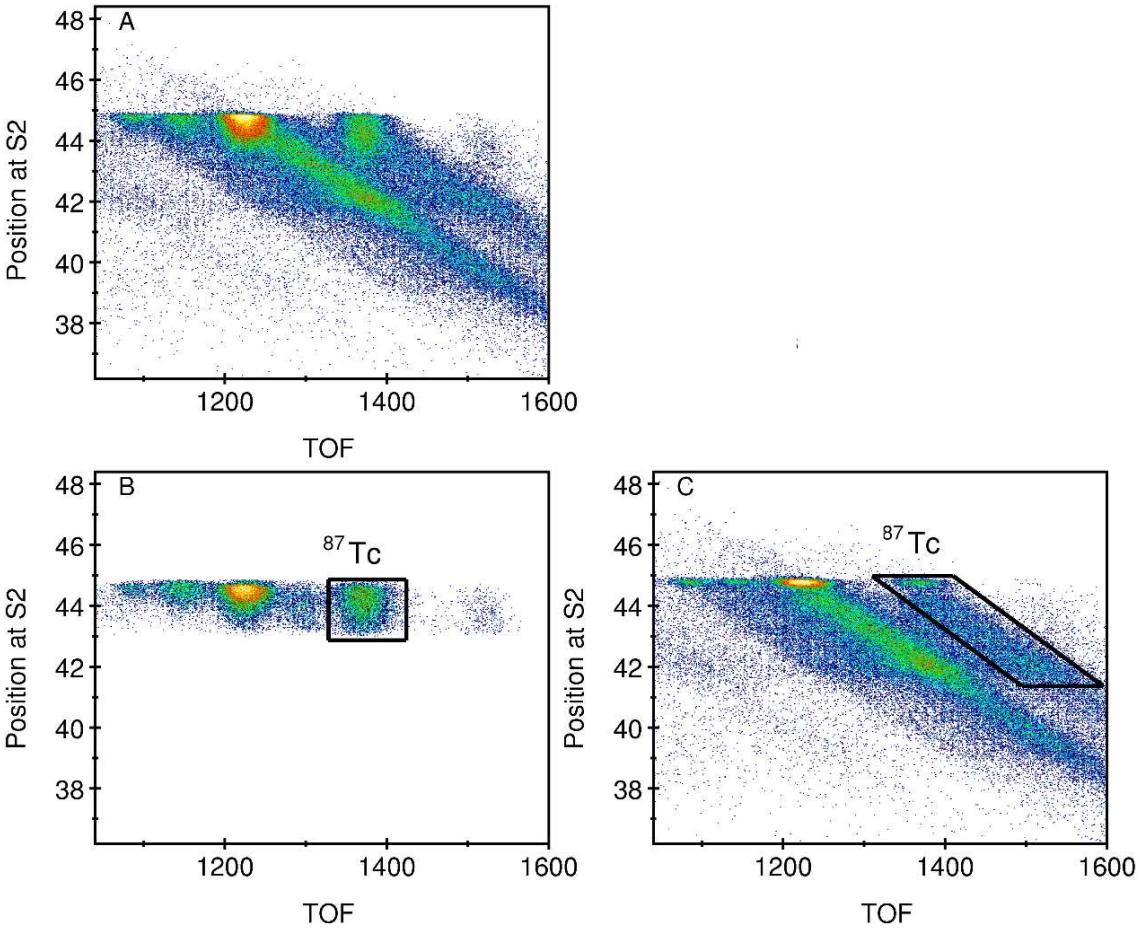

Figure 4.7: **A:** *A plot of the position at S2 of $Z = 43$ ions vs ToF.* **B:** *Same as A, now gated on a correct relationship between collected charge and position.***C:** *Same as A, now gated on an incorrect relationship between collected charge and position.*

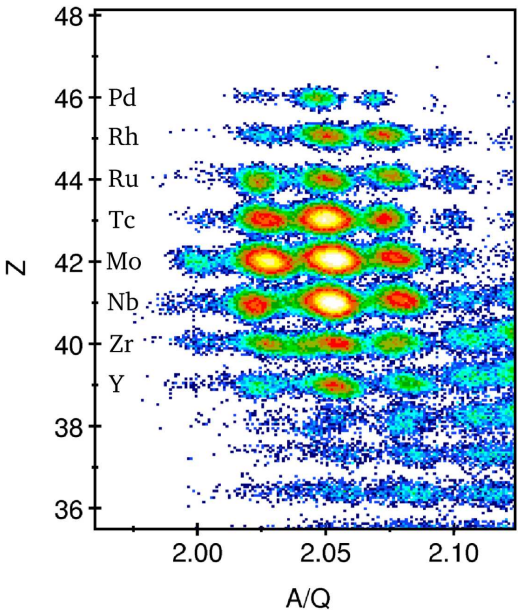

Figure 4.8: *Final, calibrated Z vs A/q identification plot for the combined ^{90}Rh, ^{86}Tc and ^{82}Nb settings.*

important for experiments investigating much heavier and neutron-rich systems.

4.3 Z vs A/q Identification Plot

Figure 4.8 shows the combined identification plot for the three settings focused on ^{90}Rh, ^{86}Tc and ^{82}Nb. This plot is constructed using the Z identification from the first MUSIC chamber and the mass to charge ratio, A/q, calculated from the magnetic rigidity of the magnets and the ToF through the second half of the FRS using the equations discussed in section 3.4.

4.4 LISE++ Simulations

The program LISE++ [106, 107] can be used to simulate the transmission of ions through the FRS. Figures 4.9, 4.10, 4.11 and 4.12, show the identification plots of the ^{96}Pd, ^{90}Rh, ^{86}Tc and ^{82}Nb settings respectively for both simulation and experiment. The source of the discrepancy between simulation and experiment is the use of copper slits in the experiment which physically stop some ion species from being transmitted to the final focus of the FRS.

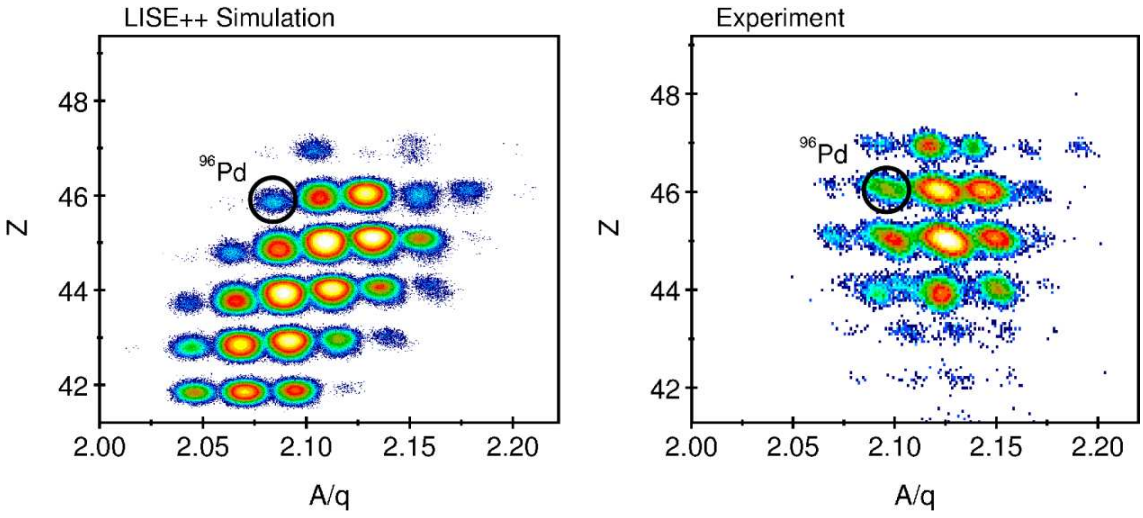

Figure 4.9: *Simulated (***Left***) and experimental (***Right***) Z vs A/q identification plot for the setting focused on ^{96}Pd.*

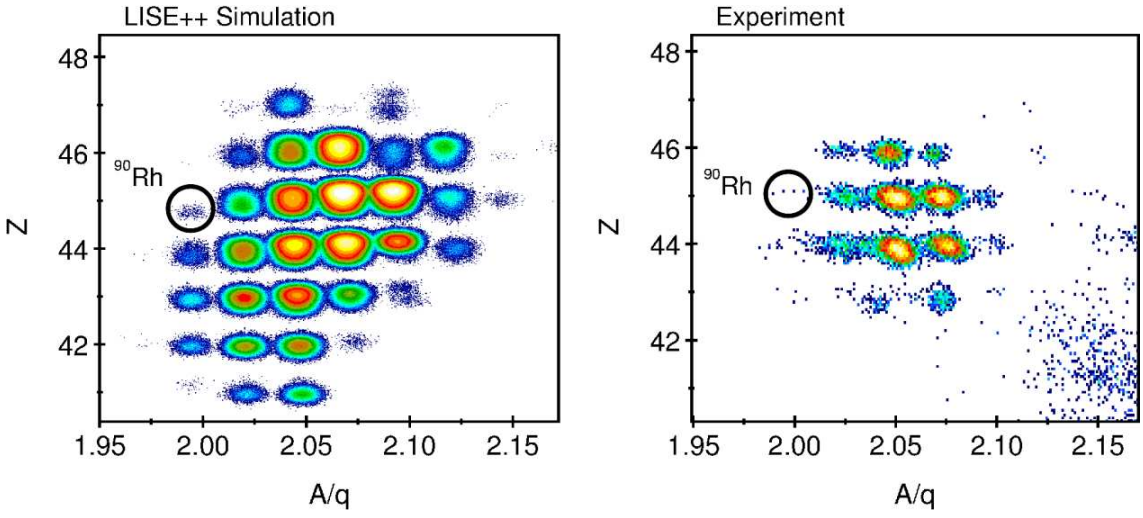

Figure 4.10: *Simulated (***Left***) and experimental (***Right***) Z vs A/q identification plot for the setting focused on ^{90}Rh.*

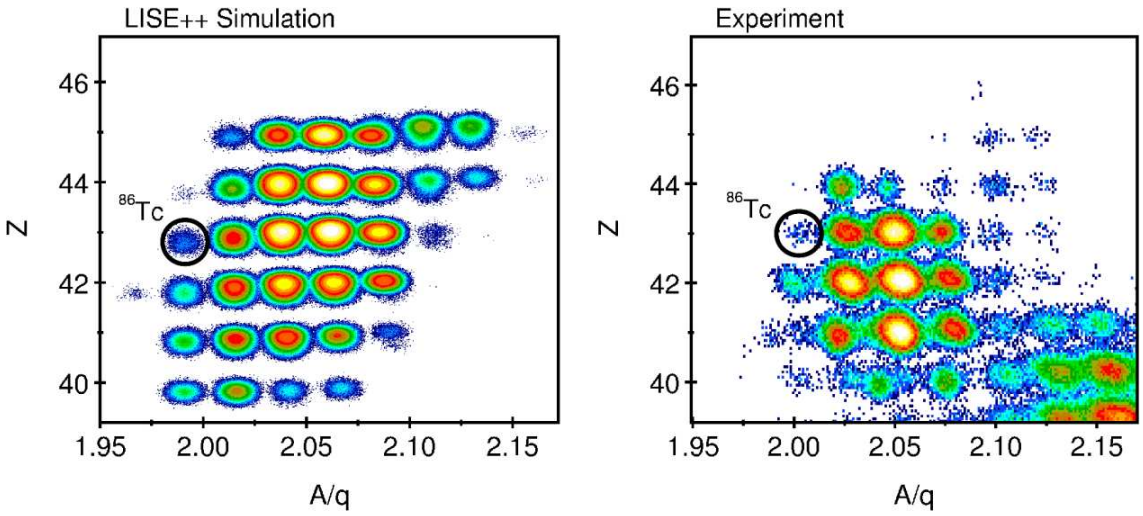

Figure 4.11: *Simulated (***Left***) and experimental (***Right***) Z vs A/q identification plot for the setting focused on* ^{86}Tc.

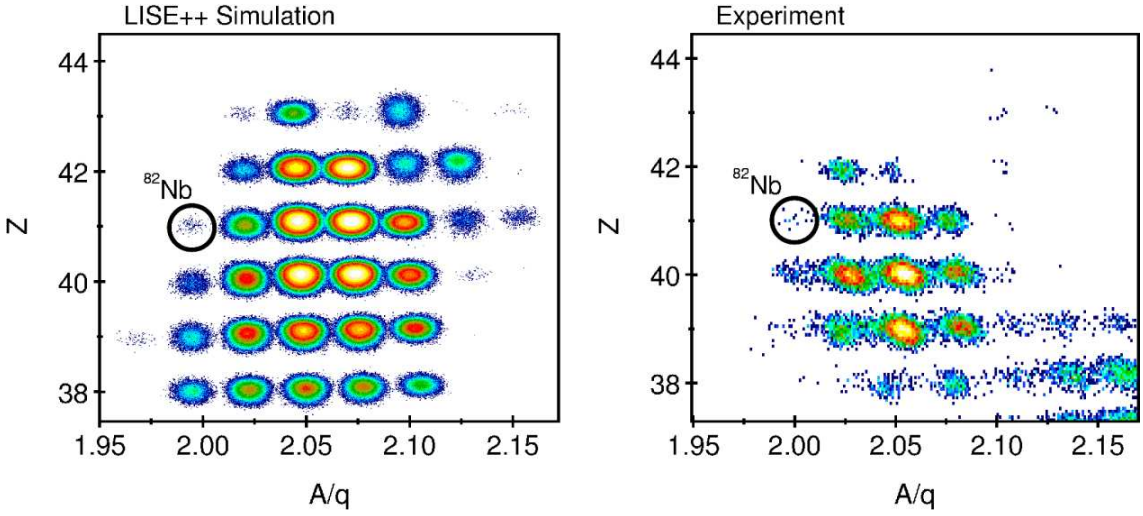

Figure 4.12: *Simulated (***Left***) and experimental (***Right***) Z vs A/q identification plot for the setting focused on* ^{82}Nb.

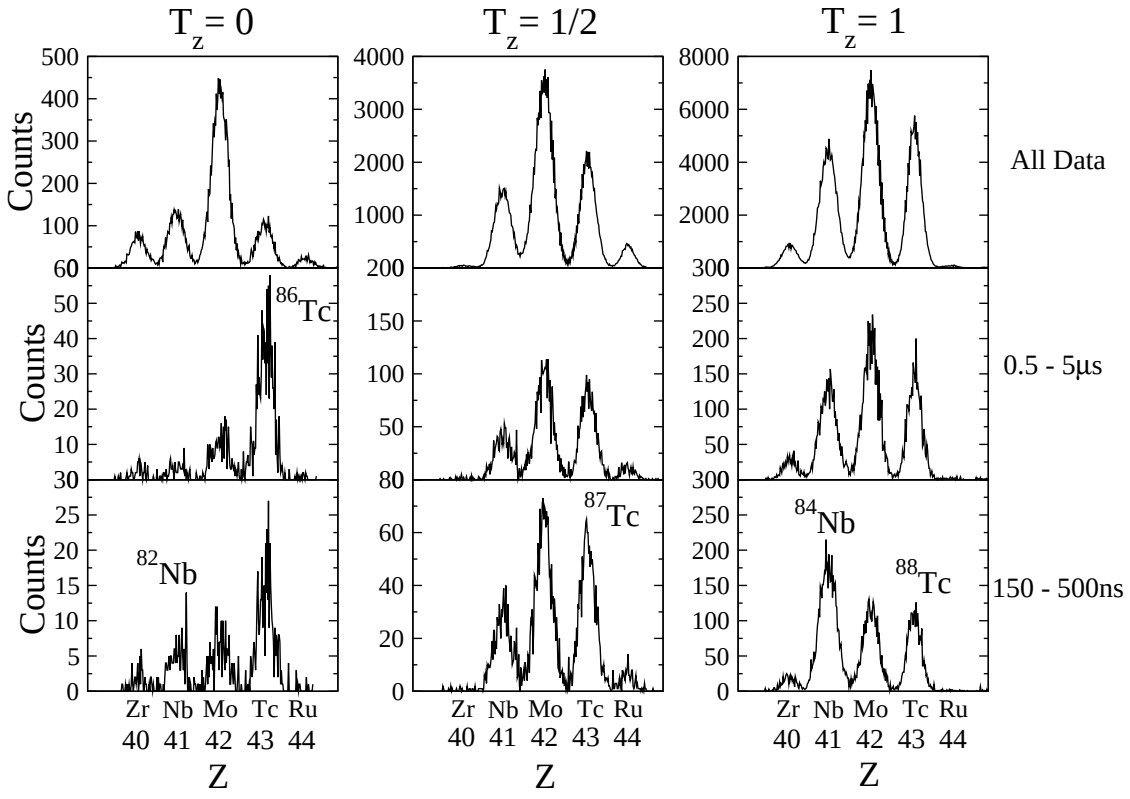

Figure 4.13: *Particle identification projections gated on delayed gamma rays with the following time conditions: (Upper) all; (Centre) 0.5→5 μs; and (Lower) 150→500 ns.*

4.5 Identification of Isomeric States

Figure 4.13 shows projections of Z for nuclei of $T_z = 0$, $\frac{1}{2}$ and 1 for which delayed gamma rays were detected in various timing regimes. The uppermost panel shows the Z projection with no additional timing condition. The central panel is gated on gamma rays observed between 1 and 5 μs after implantation to identify isomers with μs half-lives, and the lower panel shows nuclei gated between 150 and 500 ns to indicate short-lived isomers. Evidence for an isomeric state in ^{86}Tc can be seen in the central and lower projections. The lower panel also indicates evidence for previously unreported isomeric states in ^{87,88}Tc as well as the previously reported isomer in ^{84}Nb [39]. The results for these nuclei are discussed in Chapter 5.

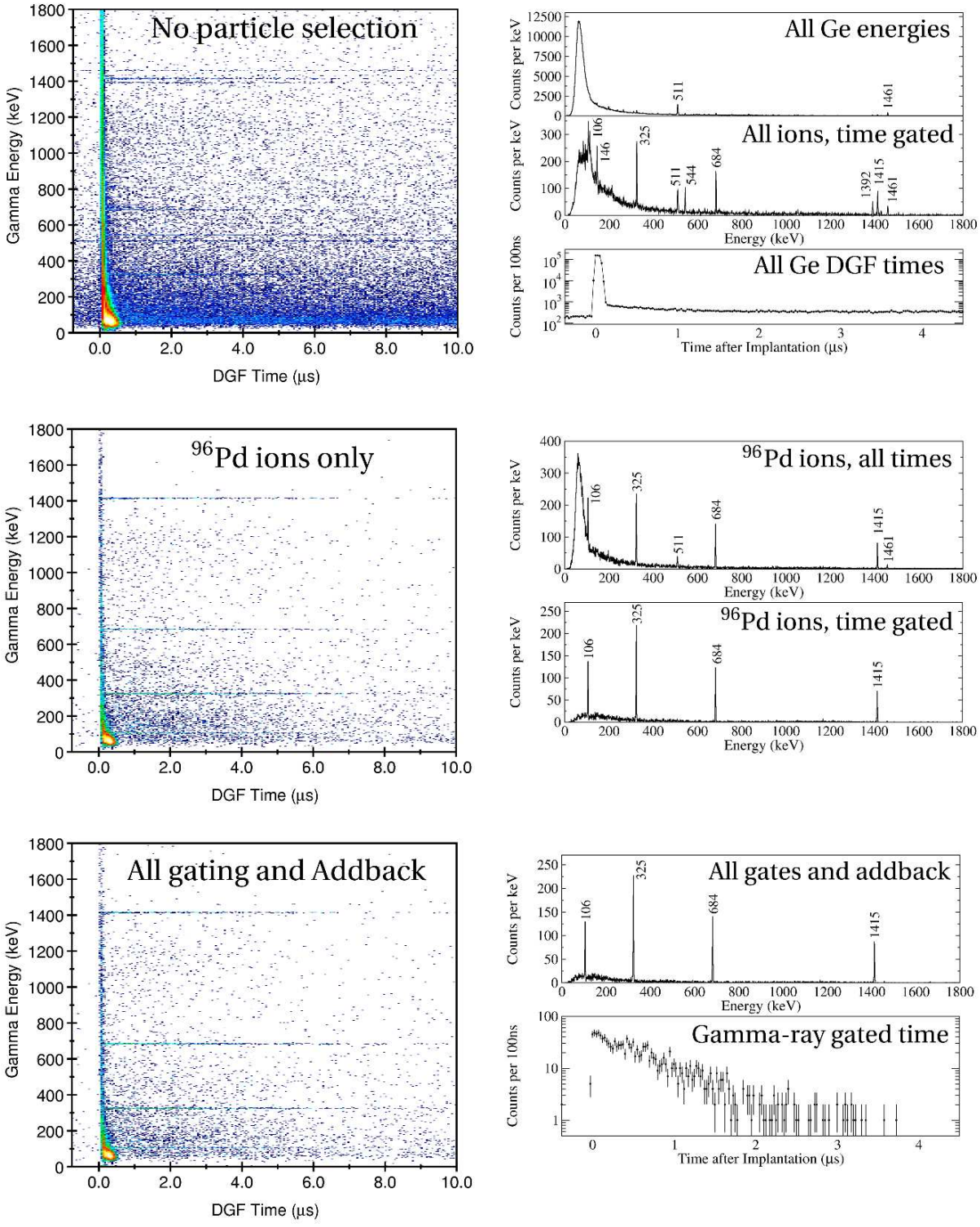

Figure 4.14: *Energy vs DGF time matrices and Ge energy and time projections (150 ns→ 5 μs following implantation) to show the effect of ion species selection, time and background reduction gating techniques described in section 4.7. Spectra with no time gate include DGF times for 100 μs following implantation.*

A gamma-ray energy vs DGF time matrix can be used to identify delayed transitions from the decay of isomeric states. The upper left panel of figure 4.14 shows such a plot for the setting focused on ^{96}Pd. The intense vertical distribution at the time of implantation (time zero) is the 'prompt' flash associated with the Bremsstrahlung and other light particle radiation produced by the ions slowing down in the stopper (described in section 4.7.3). Gamma rays with an associated lifetime can be seen growing outwards horizontally from this 'prompt' flash with their intensity dropping exponentially. In this plot, delayed transitions from isomeric decays in ^{96}Pd [128] and ^{93}Ru [129, 130, 131] can be seen, as well as background radiation such as 511 keV (electron-positron annihilation) and 1461 keV (decay of ^{40}K which is found in concrete). Note that the intensity of gamma rays from background sources does not reduce over time. The projections of energy and time at the upper right of this figure show that without selection of an individual nuclear species or time gating the energy spectrum is dominated by background peaks and the time spectrum by the prompt flash.

The central matrix of figure 4.14 demonstrates the dramatic effect that gating on an individual nuclear species can make. Here the 1.82 (5) μs isomeric state in ^{96}Pd [128] is used as an example. The projections to the right hand side show how time gating can be used to reduce the background produced by the 'prompt' flash.

The matrix and projections in the lower part of the figure show the effect on the gamma-ray spectrum of the gating techniques and addback described in section 4.7. The DGF time spectrum is also gated on the gamma-ray energies of the observed transitions and results in a very low background contribution.

4.6 Previously Reported Isomeric States

Isomeric states which have been previously identified and reported can provide an unquestionable confirmation of the particle identification and provide an additional internal calibration of gamma-ray energies and timing. ^{94}Pd and ^{96}Pd were observed in the current work and the data obtained are shown in figure 4.15. The mean lifetimes measured in the current work, 2.52 (9) μs and 676 (28) ns for ^{96}Pd and ^{94}Pd respectively, using the digital timing are consistent with previously reported values of 3.2 (4) μs [128] and 765 (14) ns [132]. Results for ^{93}Ru are shown in figure 4.16. The same gamma rays are observed but the measured mean lifetime of 3.9 (3) μs is in contrast to the

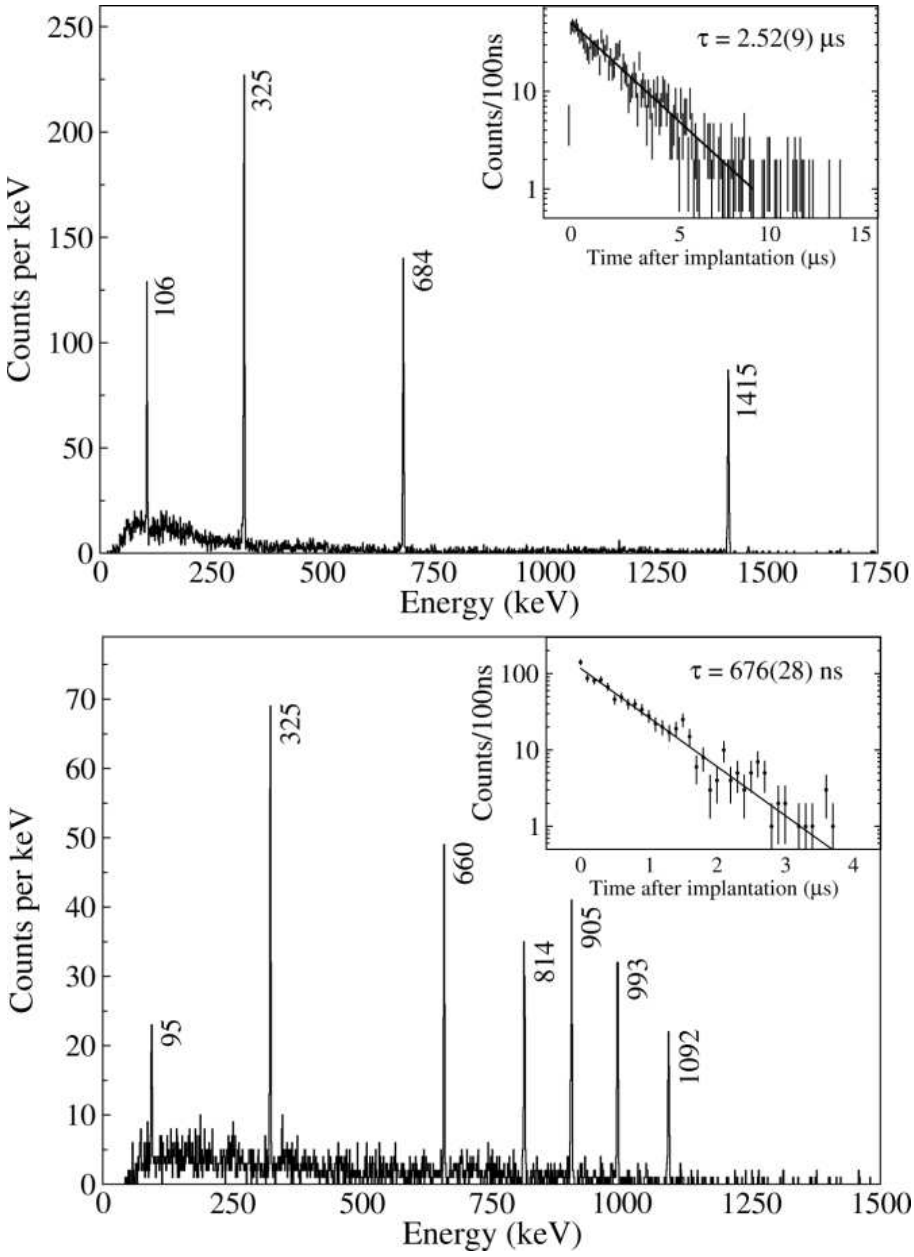

Figure 4.15: *Gamma-ray spectra of delayed events associated with ions identified as* ^{96}*Pd (***Upper***) and* ^{94}*Pd(***Lower***). Both spectra are gated between 150 ns→ 5 μs following the time of implantation. The insets show the associated decay curves from the DGF timing for* ^{96}*Pd and* ^{94}*Pd gated on the 325, 684 and 1415 keV and 325, 660, 814, 905, 993 and 1092 keV gamma rays respectively.*

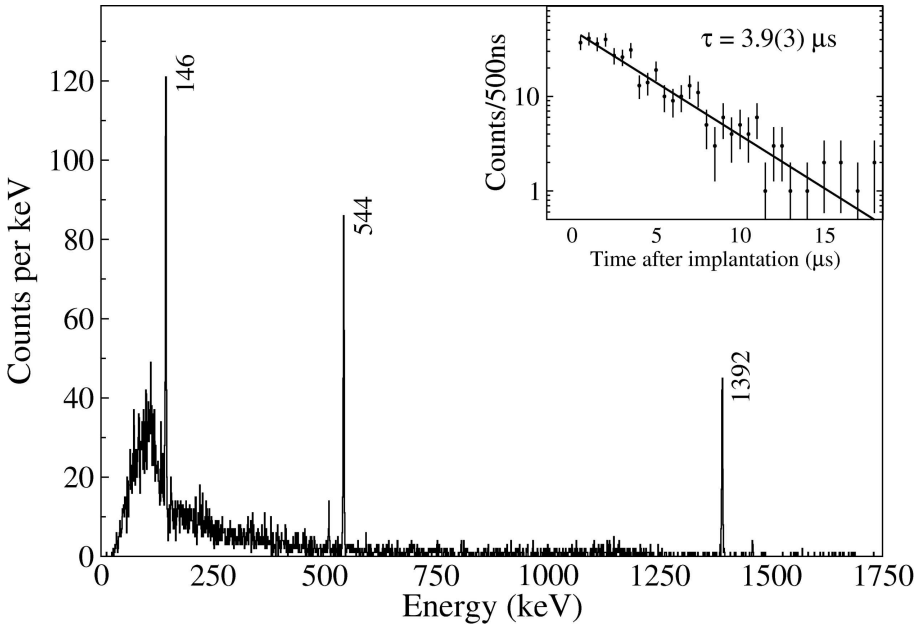

Figure 4.16: *Gamma-ray spectrum of delayed events associated with ions identified as ^{93}Ru gated between 150 ns→ 5 μs following the time of implantation. The inset shows the associated decay curve from the DGF timing gated on the 544 and 1392 keV gamma rays.*

evaluated value reported in reference [133] of 2.20 (17) μs.

4.7 Reducing Background in Gamma-ray Spectra

In the Z vs A/q method of particle identification the Z value is taken from the first MUSIC chamber and the ToF is stopped by Sci42. Therefore if a fragment undergoes a nuclear reaction after these detectors it will still be included in the identification unless additional gating techniques are applied. If these events are permitted to remain in the particle identification they will increase the background in the gamma-ray spectra and reduce the quality.

4.7.1 Nuclear Reactions Before the Stopper

Nuclear reactions which take place between the transported ion and nuclei in the gas of the first MUSIC chamber or in the niobium stripper situated between the two MUSIC chambers can be identified using a plot of the energy loss in the first MUSIC chamber against the energy loss in the second MUSIC chamber, shown in figure 4.17.

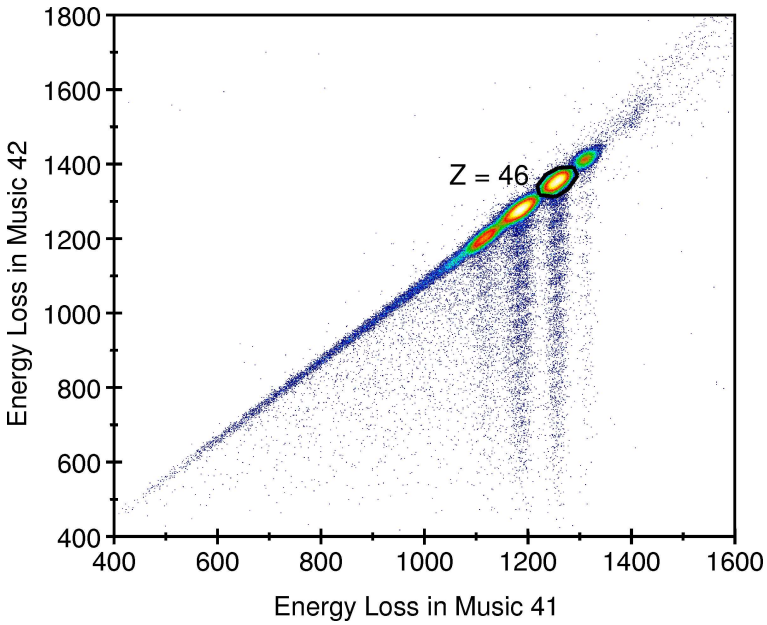

Figure 4.17: *Energy loss in MUSIC 41 plotted against the energy loss in MUSIC 42 from the ^{96}Pd setting. Events in which reactions have taken place in the first MUSIC chamber, or in the niobium stripper between the chambers are seen as off-diagonal in this plot.*

Good events in which the ion has been identified as having the same Z in both the first and second music chambers will appear along a central diagonal line in this plot. Events where the ion has undergone an interaction with a gas nucleus or in the Nb stripper will lie off this diagonal line.

Nuclear reactions can also take place in the second MUSIC chamber or in the Multiwire detector. These events will not be removed by the gating method just described but can be identified in a plot of the energy loss in Sci42 vs the energy loss in the first MUSIC chamber, shown in figure 4.18. Events to the right in this plot have the correct relationship.

4.7.2 Scintillator 43 - Veto Detector

Although the thickness of the final degrader and of the stopper are selected to bring all ions of interest to rest in the stopper some ions continue on and are detected in the veto detector, scintillator 43. The energy loss spectrum of this scintillator is shown in figure 4.19. Channels 58 and 59 of this scintillator register a pulser in every event and have been omitted from this plot. The purpose of the pulser is to ensure

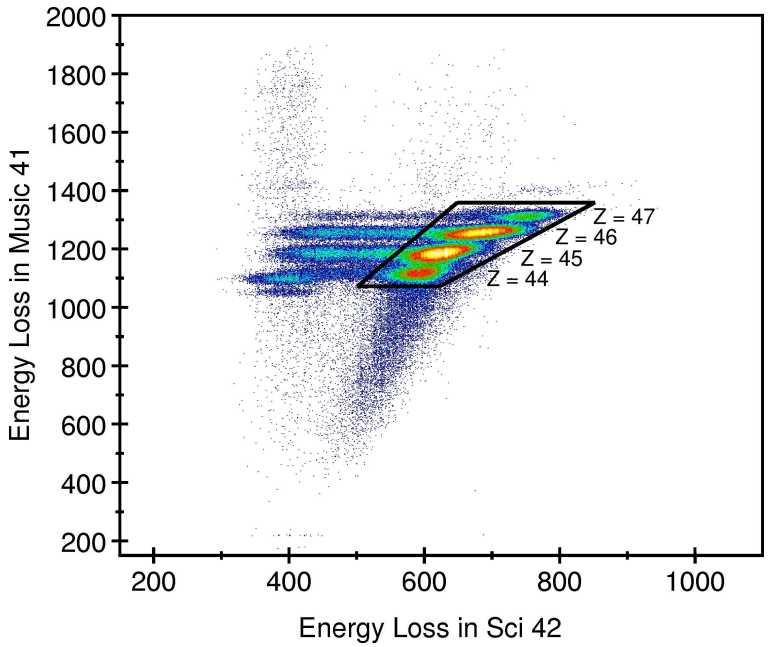

Figure 4.18: *Energy loss in Scintillator 42 plotted against the energy loss in MUSIC 41 from the ^{96}Pd setting. Events in which reactions have taken place in the second MUSIC chamber, or in another detector at the final FRS focal plane, appear to the left in this plot.*

that the scintillator is functioning correctly. In most events the ions are stopped in the stopper and there is no other signal from this detector.

This detector can also aid in rejecting events in which the ion of interest is destroyed through a reaction in the stopper. In this situation light particles may be ejected forwards and register a hit in the veto detector.

4.7.3 Germanium Signal Fold

When an ion arrives in the stopper it has to lose typically around 10-20 GeV of energy before it comes to rest. Bremsstrahlung radiation is associated with this slowing down in the stopper. A large number of X rays and gamma rays of all energies are emitted and detected in the Ge array so that a significant number of crystals fire at the same time. The number of crystals which fire is called the Ge fold.

In the current experiment the aim is to observe the decay from long-lived excited states in the neutron-deficient region around mass 80 to 90. The decay from these states to the ground state of the nucleus often consists of a cascade of only a few gamma rays.

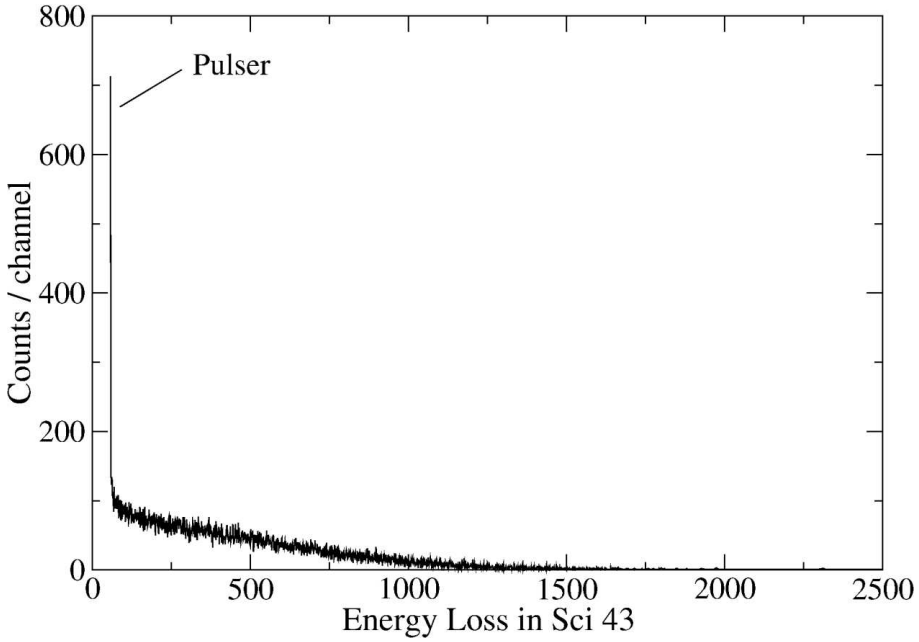

Figure 4.19: *Energy loss in Scintillator 43 from the ^{86}Tc setting. Events in which this is greater than zero are events in which the ion was not stopped in the stopper. A pulser signal is included in the data from this detector and appears in channels 58 and 59, the data in these channels have been omitted from this plot for scaling reasons but the pulser can still be seen in channel 60 to the left in the plot.*

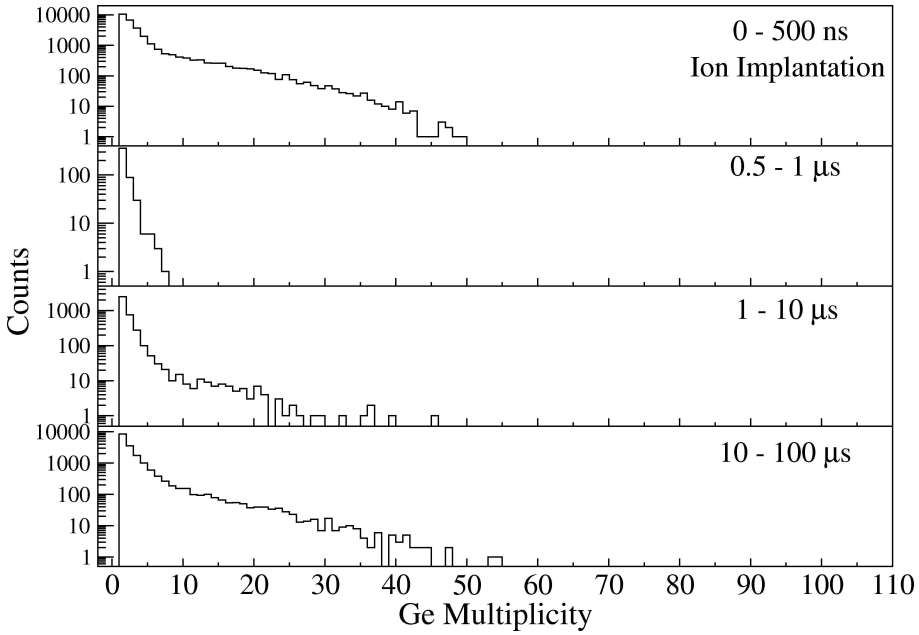

Figure 4.20: *A comparison of the germanium fold in the ^{96}Pd setting with different timing gates. The top panel is for 0 to 500 ns so constitutes the flash component in which ions arrive in the stopper. The other three panels show the fold for different time periods starting at $500ns \rightarrow 1\mu s$, $1 \rightarrow 10\mu s$ and $10 \rightarrow 100\mu s$ respectively.*

In this situation the fold will be much lower than in the event of the arrival of an ion in the stopper. However it is also important to consider the correct fold when placing a condition on its value. Figure 4.20 compares the multipilcity of each event for different timing gates. The upper panel is for the first 500 ns so includes the flash component in which ions arrive in the stopper. The other three panels show the fold for different time periods; 500ns $\rightarrow$ 1μs, 1 $\rightarrow$ 10μs and 10 $\rightarrow$ 100μs respectively. It is shown that when the time window is kept open for longer there is a greater possibility of more ions arriving in the stopper and the bremsstrahlung radiation being detected (causing large fold events).

It can also be seen from figure 4.20 that placing conditions on the fold with the intent of improving the quality of gamma-ray spectra is unnecessary. The timing conditions placed to produce gamma-ray spectra of the decay of isomeric states also reduce the background from large fold events as the vast majority of these events occur in the flash, i.e. the first 500 ns after the start.

4.7.4 Addback for the RISING Stopped-Beam Array

The RISING Stopped-Beam array is comprised of 15 cluster detectors which each consist of 7 hyper-pure germanium crystals. These clusters do not have Compton-suppression shields and are closely-packed so there is a significant probability of gamma rays scattering between crystals in different clusters. Therefore it is not the best approach to only consider adding back events within a single cluster. Although such addback routines would be simpler to program and would make improvements to the spectra. In this section results using both approaches are presented and compared. The construction of addback routines which consider scattering between clusters is also described in this section.

Addback algorithms which consider scattering between clusters must categorize crystals together into groups within which addback can be considered. These groups are determined by the geometry of the array and the relative positions of the crystals to each other. There are 105 groups, one for each crystal. The crystals to be included in each group can be determined empirically by source data and hit patterns. When a gamma ray is Compton scattered between two crystals the sum of the energies of these two crystals will sum to the full photo-peak energy of that gamma ray. In this situation a spectrum can be incremented for one crystal which shows the crystal number of a second crystal when the sum of the energies in the two crystals is equal to the full photo-peak energy of that gamma ray. The crystals to which true Compton-scatter events occur will have more counts than in the other crystals and will be easily identified in these hit patterns.

The choice of gamma ray to use for the full photo-peak energy is important. If the gamma ray is of a low energy then there is a larger chance of the full energy being deposited in a single crystal and no scattering taking place. Therefore a gamma ray of energy higher than about 1 MeV would be preferable. In addition, it is important that the gamma ray does not have a competing decay branch of two gamma rays as these two gamma rays will be distributed around the entire array but still satisfy the condition of incrementing the hit pattern, thus adding spurious events into the hit pattern.

A source of ^{60}Co beta-decays to excited states in ^{60}Ni. Two intense gamma rays of 1173 and 1332 keV are emitted following this decay and dominate the gamma-ray

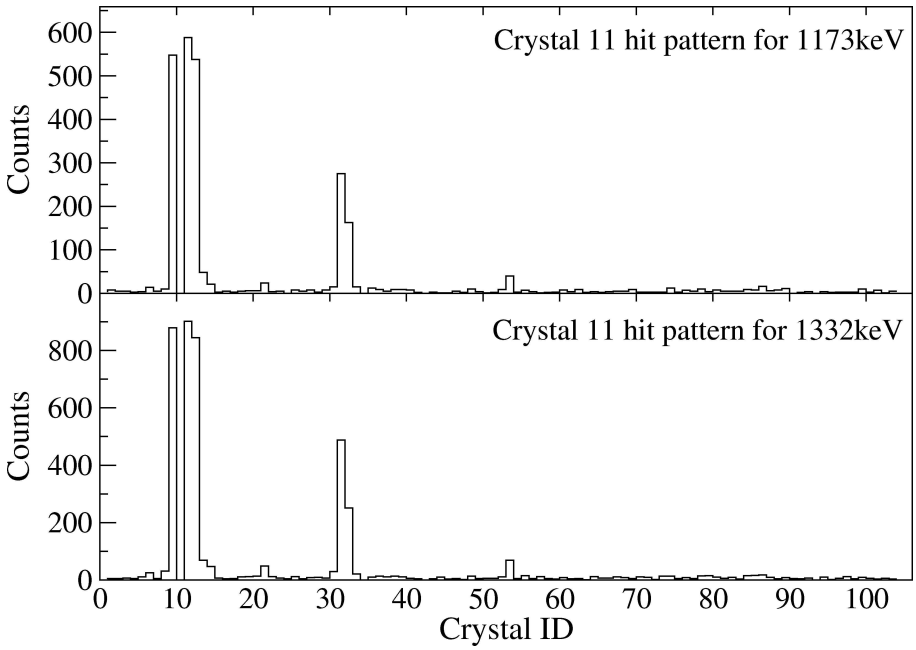

Figure 4.21: *Hit patterns produced for crystal 11 using ^{60}Co source data. The spectrum is incremented if the sum of the energy in crystal 11 and one other crystal is equal to the full photo-peak energy of 1173 or 1332 keV. The most hits are observed in the 3 crystals adjacent to crystal 11 in the same cluster, crystals (channels) 10, 12 and 13. Crystals 32, 33 and 54 are in neighbouring clusters to crystal 11 and demonstrate a modest amount of scattering to these crystals. See figure 4.22 for a geometry map of the array.*

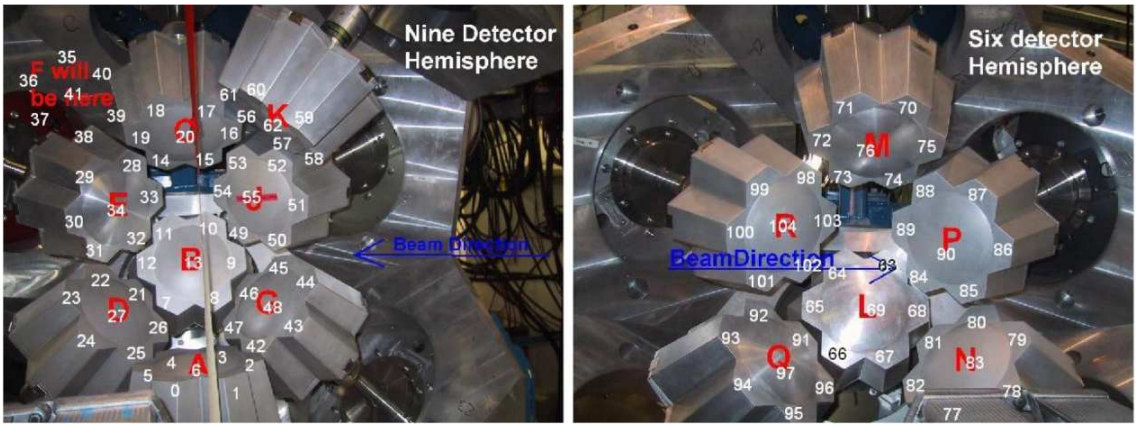

Figure 4.22: *The numbering of the crystals in the RISING Stopped Array.*

spectrum. The 1173 keV gamma ray de-populates a state at 2505 keV above the ground state of ^{60}Ni and populates a state at 1332 keV above the ground state [1]. The level at 1332 keV is the yrast 2^+ state of this even-even nucleus and there is no competing decay pathway for the 1332 keV gamma ray. Therefore these gamma rays are used to build Compton-scatter hit patterns for each crystal.

Figure 4.21 shows the hit patterns for crystal 11 for the 1173 and 1332 keV gamma rays. The most hits are observed in the 3 crystals adjacent to crystal 11 in the same cluster, channels 10, 12 and 13. Crystals 32, 33 and 54 are in neighbouring clusters to crystal 11 and demonstrate a modest amount of scattering to these crystals. Hit patterns like these were produced for each crystal in the array and used to confirm the numbering of the crystals shown in figure 4.22 and to determine a group of crystals for each crystal. These groups contain the numbers of the crystals to which scattering can take place and will be considered in the addback routines.

Figure 4.23 shows three gamma-ray spectra of both ^{60}Co and ^{152}Eu source data. The black spectrum is with no addback applied. The red spectrum shows the effect of applying a simple addback routine which considers scattering between crystals in the same cluster. These routines were written by Dirk Rudolph of Lund University [134]. This simple addback results in a reduction of the background in this spectrum when compared to the black spectrum. The blue spectrum shows the effect of applying a full addback routine which considers scattering within the groups of crystals defined using the source data technique. This spectrum again shows an improvement in the peak to background ratio of the ^{60}Co gamma-ray peaks but there is a shift in the Compton continuum towards higher energies indicating that some events are only partially reconstructed. A quantative analysis of the effects of these addback routines is shown in tables 4.3 and 4.4 by means of the peak to total ratios of the gamma rays. The peak to total ratio is the ratio of the number of counts in the full photo-peak and the total number of counts in the spectrum.

The results show that both addback routines have a positive effect on the spectra at all energies. The addback routine which considers scattering between clusters improves the spectra over the cluster addback for energies above 1 MeV but is not so good at lower energies. This is perhaps not surprising as the crystal groups were defined

[1] It is noted that a decay branch consisting of two gamma rays of 347 keV and 826 keV competes with this transition on a less than 1% level. This will not affect the current analysis.

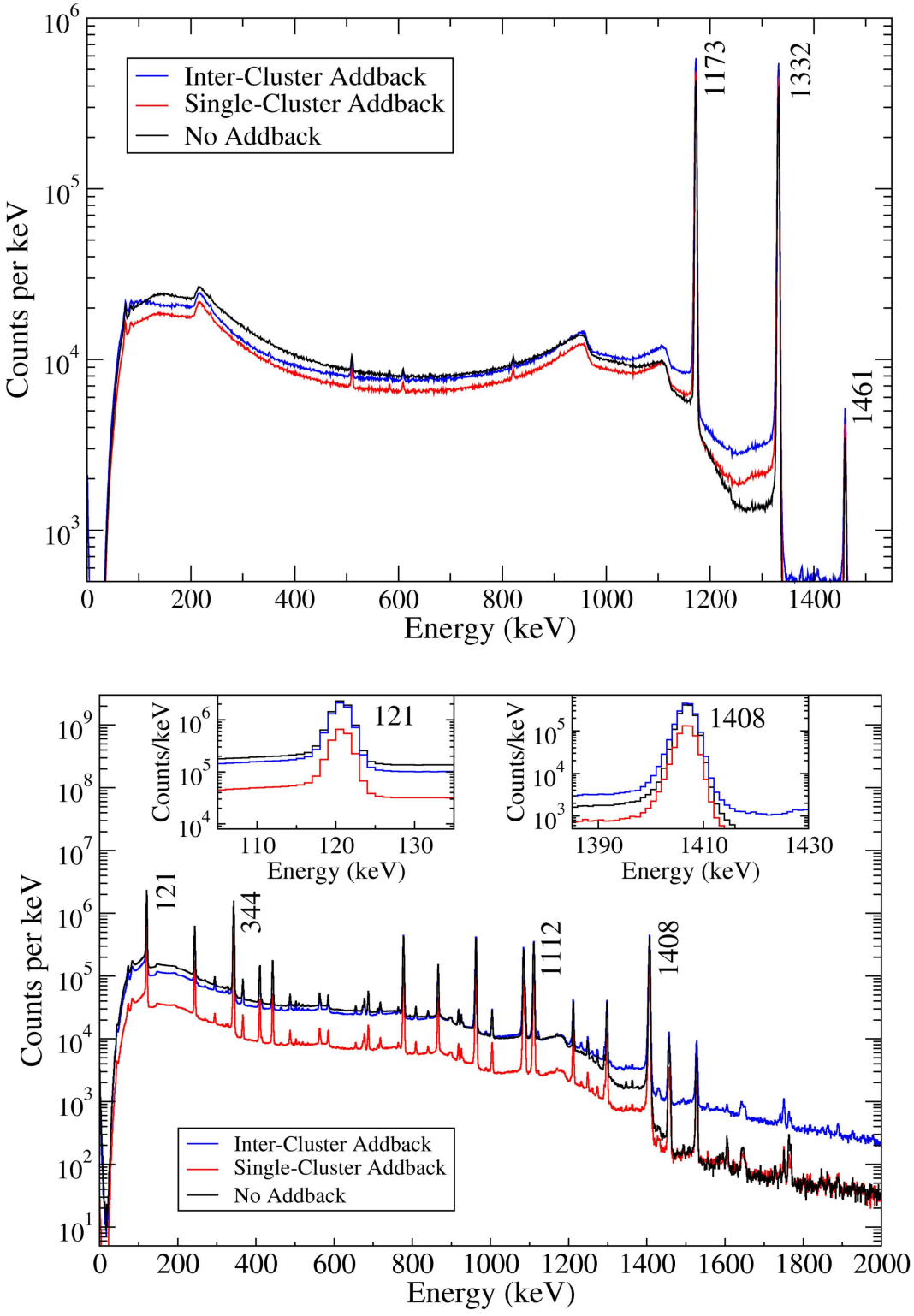

Figure 4.23: *Gamma-ray spectra of ^{60}Co (Upper) and ^{152}Eu (Lower) source data. The black line is without addback. The red line with addback only considering scattering within a cluster (Single-Cluster addback). The blue line is with addback that also considers scattering between different clusters (Inter-Cluster addback).*

Table 4.3: *The effect of addback routines on the peak to total ratio of the 1173 and 1332 keV gamma rays emitted from a ^{60}Co source.*

Condition	1173 keV	1332 keV
No Addback	0.0909	0.0809
Single-Cluster Addback	0.1218	0.1102
Inter-Cluster Addback	0.1250	0.1137

Table 4.4: *The effect of addback routines on the peak to total ratios of gamma rays emitted from a ^{152}Eu source.*

Condition	121 keV	344 keV	779 keV	1086 keV	1408 keV
No Addback	0.0853	0.0605	0.0176	0.0115	0.0203
Single-Cluster Addback	0.0931	0.0699	0.0216	0.0146	0.0259
Inter-Cluster Addback	0.0893	0.0685	0.0216	0.0147	0.0261

from hit patterns using gamma rays above 1 MeV. The routines can be improved by more sophisticated algorithms which act differently for various energies of gamma ray. This would make it necessary to investigate the Compton scattering properties of lower energy gamma rays in the array.

Chapter 5

Results and Discussion

The primary aim of the current work was to investigate the low-lying structures of the odd-odd self-conjugate nuclei, ^{82}Nb and ^{86}Tc. Results for these nuclei related to neutron-proton pairing are described in reference [135]. Preliminary results from this work have been presented in references [115, 125, 126, 136, 137, 138]. This thesis reports results from the final analysis of the data.

5.1 Previously Unobserved States in $^{82}_{41}Nb_{41}$

The existence of a short-lived isomeric state in $^{82}_{41}Nb_{41}$ was suggested by Chandler *et al.* [39] but no discrete gamma-ray transitions could be identified. The current data have confirmed the assignment of this isomeric state and facilitated the identification of two other excited states. Figure 5.1 shows the energy vs DGF time matrix for ions identified as ^{82}Nb and figure 5.2 shows the projection of gamma-ray energies in the time range 20→150 ns. The three delayed gamma rays associated with the decay of this isomer have energies of 124, 418 and 638 keV. A least-squares fit to the summed time spectrum of the 418 and 638 keV transitions gives a mean lifetime of 133 (25) ns (see inset of figure 5.2).

A gamma-gamma energy coincidence analysis (shown in figure 5.3) finds all three gamma rays to be in mutual coincidence. The level scheme constructed from these data is shown in figure 5.4. The 638 and 418 keV gamma rays have similar energies to the $4^+ \rightarrow 2^+$ (634 keV) and $2^+ \rightarrow 0^+$ (407 keV) transitions in the isobaric analogue, $^{82}_{40}Zr_{42}$ [139]. Therefore it is assumed that the isomeric state decays directly to the 4^+ member of the $T = 1$ ground-state band via a 124 keV transition.

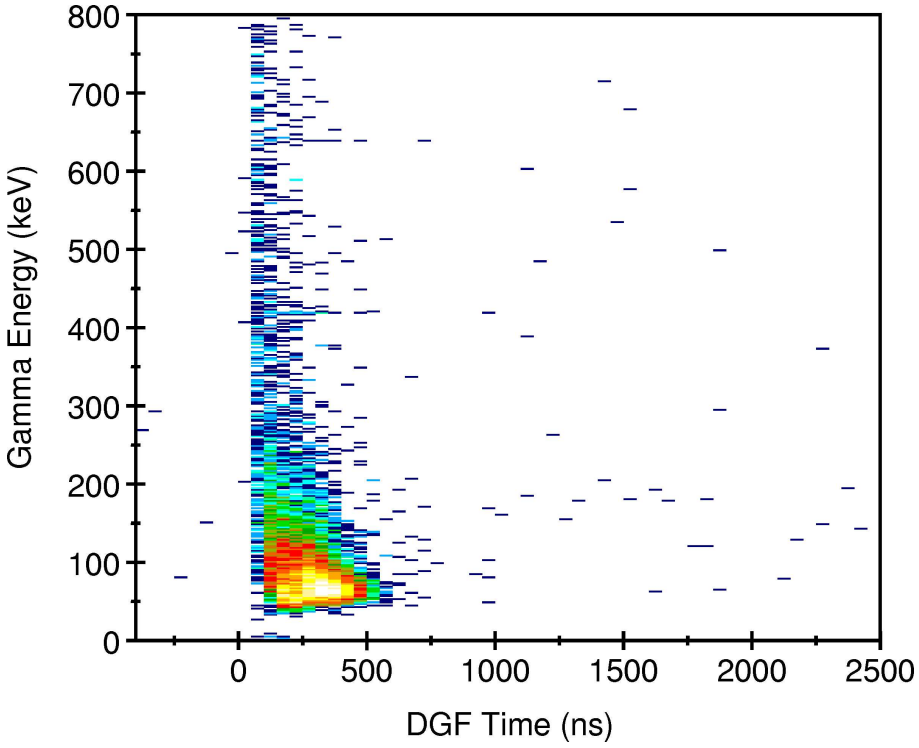

Figure 5.1: *Energy vs DGF time plot gated on ions identified as ^{82}Nb.*

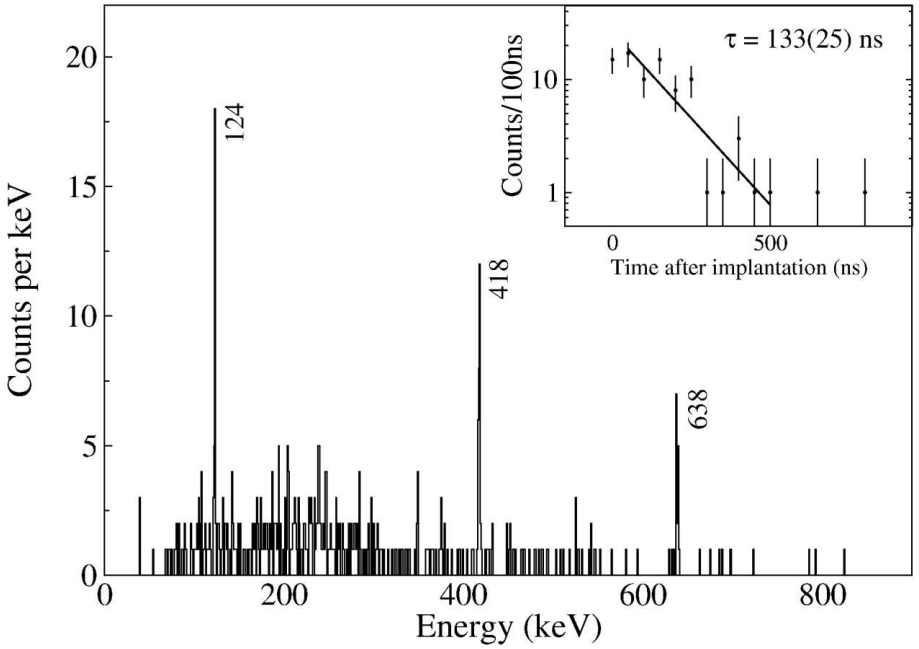

Figure 5.2: *Gamma-ray spectrum gated on ions identified as ^{82}Nb and a time gate between 20 and 150 ns. The inset is the associated DGF time spectrum gated on the 418 and 638 keV gamma rays.*

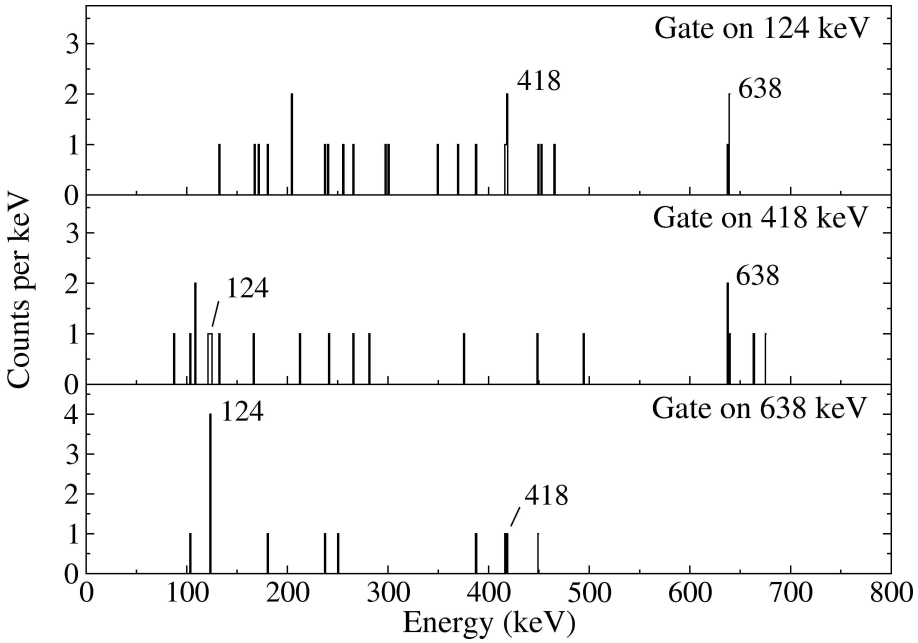

Figure 5.3: *Coincidence gamma-ray spectrum gated on ions identified as ^{82}Nb and time-gated between 20 and 150 ns.*

The gamma-ray intensity balance around the (4^+) state has been used to infer the internal conversion coefficient, α_{tot}, of the 124 keV transition to be 0.3(3) (for further explanation see Appendix A). The large uncertainty does not make it possible to discriminate between an M1, E1 or E2 multipolarity assignment (see table 5.1). An E2 transition would be somewhat enhanced when compared to the Weisskopf estimate so seems less probable (table 5.1). In addition the deduced value for the isomeric ratio [140] depends on the value of the internal conversion coefficient of the direct decay. Although the statistical uncertainties are large an E2 multipolarity for the 124 keV transition would result in an unphysically large isomeric ratio of 185(354)%. E1 or M1 assignments yield more physical values of 78(140)% and 76(137)% respectively. Using these arguments, plausible spin/parity assignments are restricted to $I^\pi = 5^-$ or 5^+.

A shell model calculation has been performed for ^{82}Nb [141]. The valence space used for the calculation was limited to the $g_{9/2}$ and $p_{1/2}$ orbitals and the results are shown in figure 5.4. The 2^+ member of the ground-state band is predicted at 1315 keV in the calculation, 897 keV above the experimentally observed level. This large discrepancy must be due to the limited valence space allowed in the calculation. A more accurate shell model calculation could perhaps be achieved if other orbitals were included in the valence space. Possible candidates would be the $f_{5/2}$ and $p_{3/2}$, or from

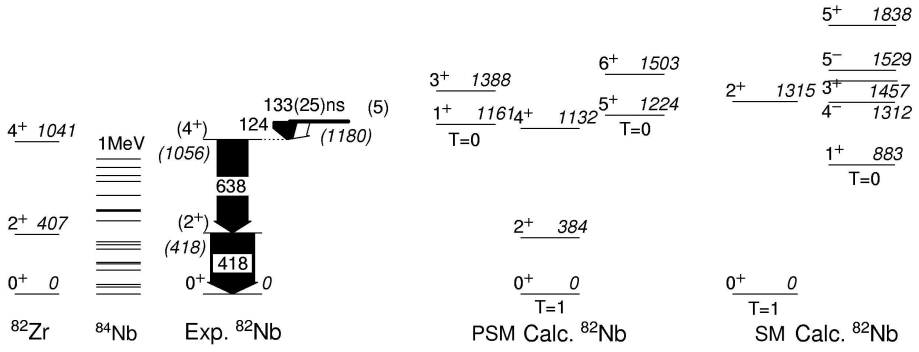

Figure 5.4: *Experimental level scheme of ^{82}Nb constructed from the current data and results from Shell model and Projected Shell Model calculations. The isobaric analogue states in ^{82}Zr and the excited states below 1 MeV excitation in ^{84}Nb are also shown for comparison.*

the next major shell the $d_{5/2}$ and $g_{7/9}$ orbitals. Such a calculation would undoubtably be more computationally difficult and greater insight may be achieved in this case with the application of a different theoretical model.

Total-Routhian-Surface (TRS) calculations can be used to predict the deformation and single-particle structure in the vicinity of the Fermi surface in a given nucleus. The configuration-constrained potential energy surface calculations developed by Xu [67] can predict the deformation for a specific multiquasiparticle configuration whilst accounting for the γ degree of freedom. Figure 5.5 shows a TRS calculation for the ground state of ^{82}Nb. The calculation predicts a large stable prolate deformation with $\beta_2 = 0.430$ which is maintained in the ground-state band to at least $\omega = 0.403$ MeV/$\hbar$ (shown to the right of figure 5.5). This compares well with the measured value of β_2=0.41(7) in the isobaric analogue, ^{82}Zr which was determined from the $B(E2 : 2^+ \rightarrow 0^+)$ value with the assumption of axial symmetry [143].

The Projected Shell Model (PSM) [63] has had success in describing the observed structures in deformed nuclear systems. The inclusion of a *np* interaction [64] has been used to accurately reproduce the observed ground-state structures in the even-even $N = Z$ nuclei with $A = 68 \rightarrow 88$. The projected shell model has been used here to suggest possible configurations for the isomeric state observed in ^{82}Nb. The calculation predicts a $I^\pi = 5^+$, 2-quasiparticle state with a Nilsson configuration of $\nu[422]5/2^+ \times \pi[422]5/2^+$ at 1224 keV. This is just above the $T = 1$, 4^+ state and is a possible candidate for the configuration of the isomer. The population of a $T = 0$

Table 5.1: *Partial half-lives and calculated total conversion coefficients [142] of transitions in ^{82}Nb for various multipolarities derived from the single particle unit Weisskopf estimates. The Weisskopf estimates are in units of seconds.*

	α_{TOT}			Weisskopf estimates (s)		
	124 keV	418 keV	638 keV	124 keV	418 keV	638 keV
E1	0.065	2.19×10^{-03}	7.98×10^{-04}	1.87×10^{-13}	4.88×10^{-15}	1.37×10^{-15}
E2	0.534	7.81×10^{-03}	2.26×10^{-03}	8.97×10^{-07}	2.06×10^{-09}	2.49×10^{-10}
E3	4.11	0.025	5.73×10^{-03}	6.53	1.32×10^{-03}	6.84×10^{-05}
E4	34.9	0.078	0.014	$7.16\times10^{+07}$	$1.27\times10^{+03}$	28.3
M1	0.131	5.67×10^{-03}	2.10×10^{-03}	1.46×10^{-12}	1.28×10^{-13}	5.50×10^{-14}
M2	1.12	0.020	5.98×10^{-03}	5.64×10^{-05}	1.30×10^{-07}	1.56×10^{-08}
M3	8.80	0.066	0.015	411	0.083	4.31×10^{-03}
M4	71.2	0.214	0.039	$4.51\times10^{+09}$	$8.02\times10^{+04}$	$1.78\times10^{+03}$

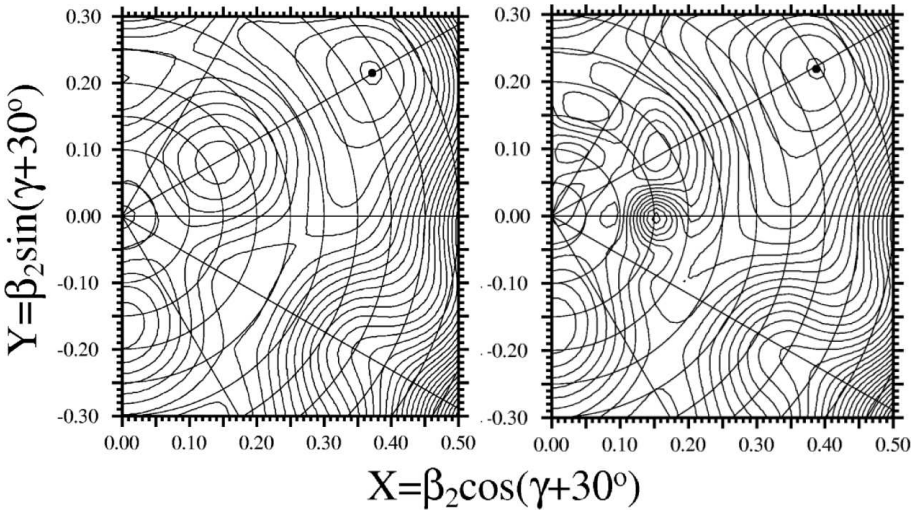

Figure 5.5: *TRS calculation for the ground state and an excited state of ^{82}Nb. The minimum of the ground state is located at $\beta_2 = 0.430$, $\gamma = 0.1$ and $\beta_4 = -0.023$. This strong prolate deformation is still dominant at $\omega = 0.403$ MeV/$\hbar$ shown to the right. Contours are separated by 200 keV.*

state with this configuration is also consistent with the low-lying band structures in the $T_z = +\frac{1}{2}$ neighbours ^{81}Zr [78] and ^{83}Nb [144, 145]. The calculations also predict two low-lying $K = 4^-$ states at approximately 1.3 MeV which are not included in the figure.

The measured mean lifetime of the isomeric state in ^{82}Nb is longer than predicted by the partial half-life for a 124 keV M1 transition (~ 1.5 ps). A well known mechanism by which nuclear half-lives can be prolonged in axially well deformed nuclei is that of K hindrance [30] which was discussed in section 2.8.4. In the case of ^{82}Nb the 124 keV transition decaying from a $I^\pi = K^\pi = (5^+)$ to a $I^\pi = (4^+)$, $K = 0$ state has $\Delta K = 5$, $\nu = 4$, where $\nu = \Delta K - \lambda$. Assuming an M1 decay for the 124 keV transition in ^{82}Nb, this results in a value of $f_\nu \approx 11$. This value is intermediate between the accepted f_ν values of approximately 100 for the best case axially-symmetric K isomers and $f_\nu \sim 1$ for unhindered decays. This is suggestive of some degree of K mixing possibly associated with gamma-softness.

The isomeric state in ^{82}Nb lies more than half an MeV below the proton separation energy which is calculated to be 1775 (341) keV [4].

5.2 Isomeric States in $^{84}_{41}$Nb$_{43}$

The first gamma-ray transitions assigned to ^{84}Nb were identified by Gross *et al.* [146]. Two band structures were observed but were not fitted into a level scheme. A further in-beam study by Mărginean *et al.* [147] using a ^{58}Ni(^{28}Si,$pn\gamma$) reaction enabled the construction of a comprehensive level scheme at low energy, shown in figure 5.6. Several rotational bands were also identified (including those suggested by Gross *et al.*) and connected to the low-lying structure. The author notes the confirmation of a previously reported isomeric state but within the experimental set up was unable to measure the half-life or identify other long-lived states.

The isomer reported had been observed in the fragmentation of a ^{92}Mo beam. Preliminary results were published in reference [148] prior to the study of Mărginean *et al.*. The final analysis was published later by Chandler *et al.* [39] where two decay paths depopulating an isomeric state at 338 keV were reported with a mean lifetime of 148 (28) ns. This paper also suggests a state at 48 keV may have an additional lifetime associated with its decay but low statistics prevented this from being confirmed.

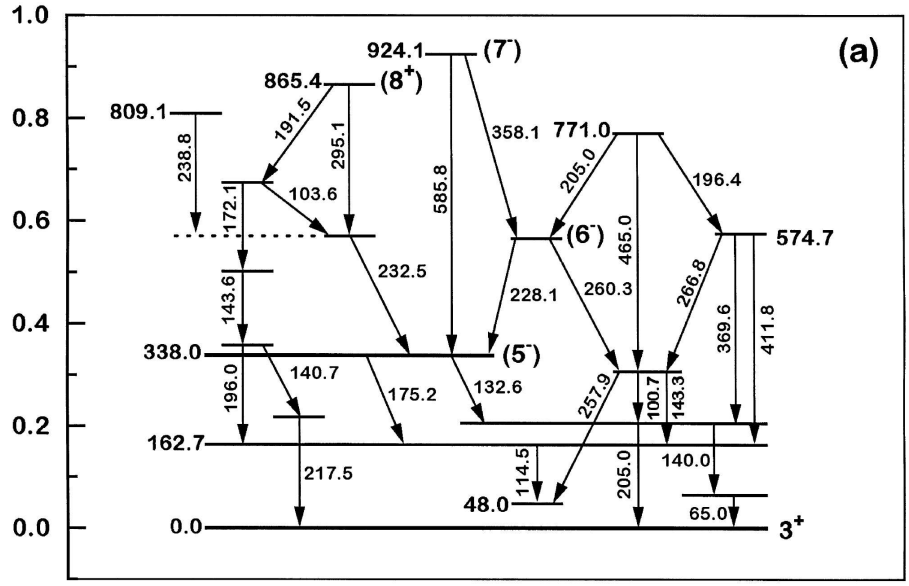

Figure 5.6: *Level scheme for ^{84}Nb reported by Mărginean et al. (taken from reference [147])*

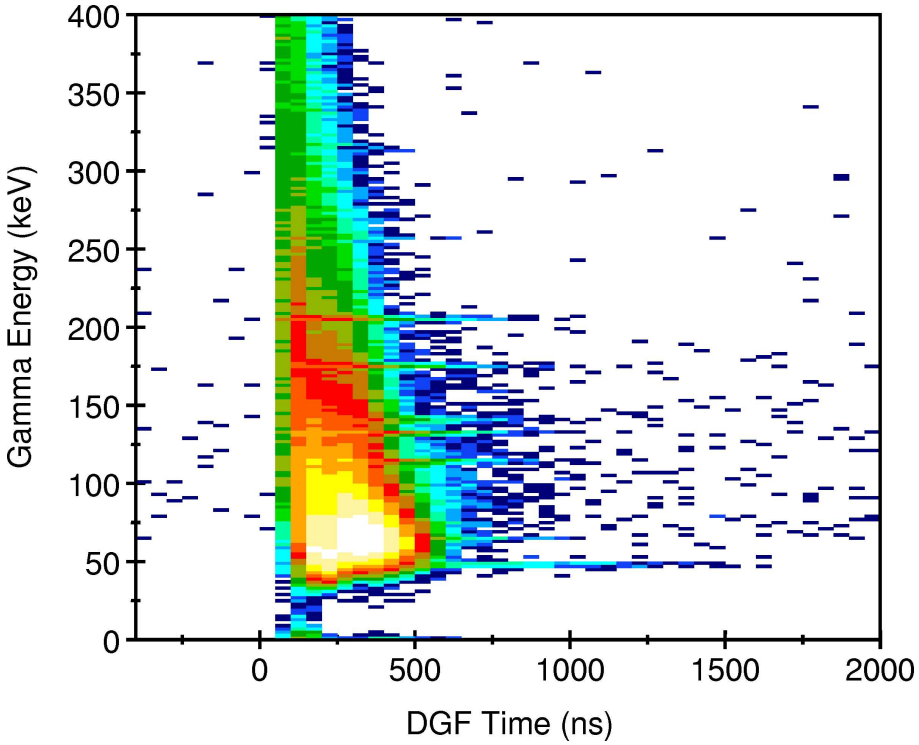

Figure 5.7: *Energy vs DGF time plot gated on ions identified as ^{84}Nb. Note this plot has a threshold of 2 counts on the z axis.*

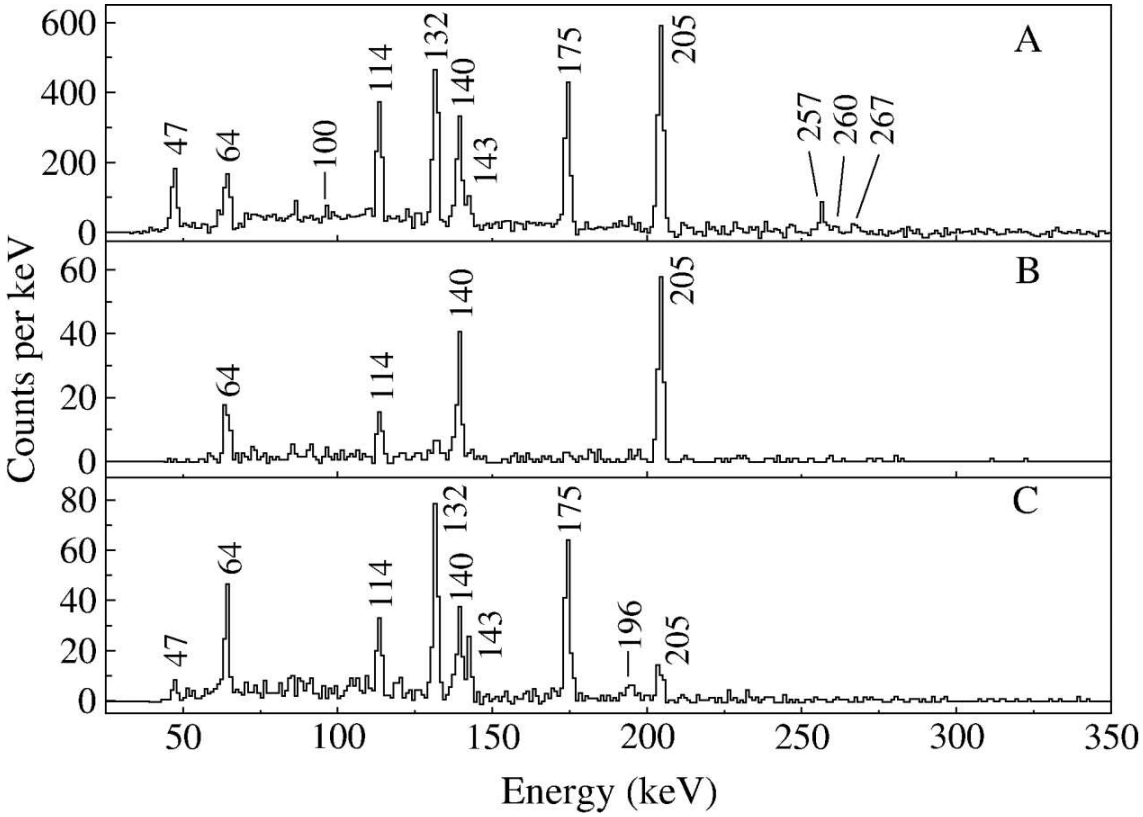

Figure 5.8: *Singles (***A***) and coincidence gamma-ray spectra gated on ions identified as ^{84}Nb and a time gate between 200 ns and 1.75 μs.* **B:** *Sum of gate on 132 and 175 keV transitions to highlight the previously observed isomeric decay.* **C:** *Sum of gates on gamma rays of 47, 64, 114 and 140 keV. Note the coincidence of the 205 keV transition and the enhancement of the 143 and 196 keV transitions, indicating the existence of the isomeric state at higher excitation energy.*

The present work is in agreement with the findings of Chandler *et al.* and has made it possible to measure the mean lifetime of the 48 keV state. In addition the present work finds that a state at 771 keV reported by Mărginean *et al.* is isomeric. The gamma-ray energy vs DGF time matrix produced from gating on ions identified as ^{84}Nb is shown in figure 5.7 and a projection of the delayed gamma rays is shown in figure 5.8.

The present work is only sensitive to delayed gamma rays. The singles spectrum shown in the upper panel of figure 5.8 indicates, in addition to known isomeric transitions, delayed gamma rays at 100, 143, 257, 260 and 267 keV. These transitions were not observed by Chandler *et al.* but are included in the level scheme reported in the in-beam study. A sum of energy coincidence gates on the 132 and 175 keV direct decays from the previously reported isomeric state is shown in the central panel and indicates the previously reported decay paths. When the low-lying transitions (47, 64, 114 and 140 keV) are gated on, as shown in the lower panel, an enhancement of the 143 and 196 keV transitions is observed. This is an indication of an additional isomeric state at higher excitation energy. These transitions appear as doublets in the level scheme of Mărginean *et al.* giving two possible candidates for the location of the isomeric state. The fact that the low-lying transitions are also in coincidence with the 205 keV transition rules out one of these possibilities as the 205 keV transition is also a doublet and appears higher in the cascade of only one candidate decay path. Furthermore the observation of the 257, 260 and 267 keV gamma rays in the singles data (too weak to appear in coincidence) adds further strength to the assignment of the 771 keV state as isomeric. Other gamma rays previously placed in the level scheme below the 771 keV state are assumed to be weaker branches as they are not observed in the current data. Their intensities were not reported by Mărginean *et al.*. The transitions and relative intensities observed in the current work are shown in the level scheme of figure 5.9.

The intensity of the 205 keV transition depolpulating the 771 keV isomeric state was made equal to the intensity of the 260 keV transition (with relative efficiciency correction) and subtracted from the total observed 205 keV intensity. It is noted that additional intensity may advance through the 228 keV transition to the 338 keV isomeric state but this is too weak to observe in the current data.

Least-squares fits to the associated decay curves have been made to determine the mean lifetimes of the three isomeric states observed in ^{84}Nb. The fits are shown in

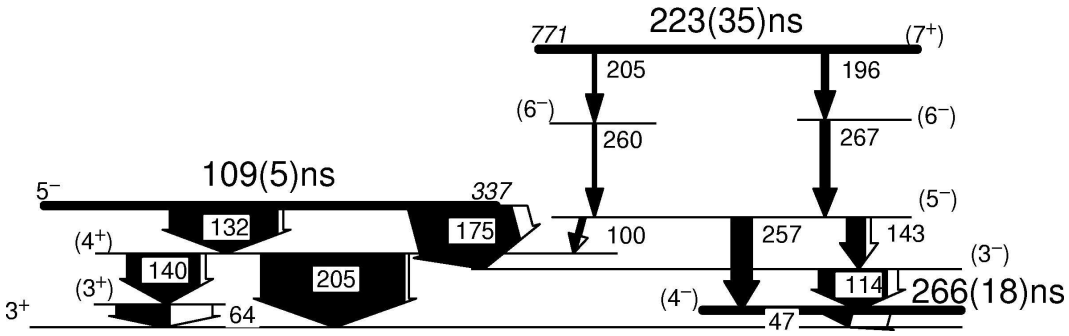

Figure 5.9: *Proposed level scheme for ^{84}Nb observed in the current work. The widths of the arrows indicate the relative intensities of the gamma rays.*

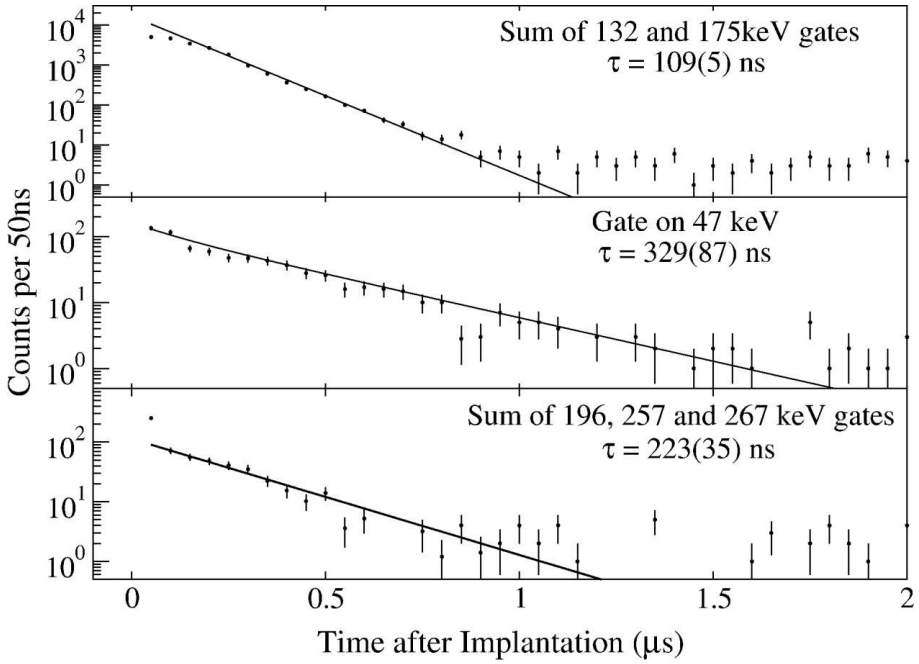

Figure 5.10: *Mean lifetime fits to the gamma rays associated with the decay of the isomeric states in ^{84}Nb. The decay from the 47 keV isomeric state has been fitted using a two-component least-squares fit due to feeding from the 109 (5) ns isomeric state.*

Table 5.2: *Partial half-lives of transitions in ^{84}Nb for various multipolarities derived from the single particle unit Weisskopf estimates. The units are seconds.*

	47 keV	65 keV	100 keV	114 keV	132 keV	140 keV	143 keV
E1	3.38×10^{-12}	1.28×10^{-12}	$3.51\times10^{+13}$	2.31×10^{-13}	1.49×10^{-13}	1.25×10^{-13}	1.20×10^{-13}
E2	1.11×10^{-04}	2.20×10^{-05}	2.55×10^{-6}	1.27×10^{-06}	6.12×10^{-07}	4.57×10^{-07}	4.26×10^{-7}
E3	$5.54\times10^{+03}$	$5.72\times10^{+02}$	$2.81\times10^{+1}$	10.5	3.81	2.53	2.29
E4	$4.16\times10^{+11}$	$2.25\times10^{+10}$	$4.66\times10^{+8}$	$1.32\times10^{+08}$	$3.57\times10^{+07}$	$2.11\times10^{+07}$	$1.86\times10^{+7}$
E5	$4.41\times10^{+19}$	$1.25\times10^{+18}$	$1.09\times10^{+16}$	$2.34\times10^{+15}$	$4.73\times10^{+14}$	$2.49\times10^{+14}$	$2.13\times10^{+14}$
M1	1.01×10^{-11}	5.30×10^{-12}	2.24×10^{-12}	1.69×10^{-12}	1.27×10^{-12}	1.13×10^{-12}	1.10×10^{-12}
M2	7.09×10^{-03}	1.40×10^{-03}	1.63×10^{-4}	8.09×10^{-05}	3.91×10^{-05}	2.92×10^{-05}	2.72×10^{-5}
M3	$3.54\times10^{+05}$	$3.66\times10^{+04}$	$1.79\times10^{+3}$	$6.74\times10^{+02}$	$2.44\times10^{+02}$	$1.62\times10^{+02}$	$1.47\times10^{+2}$
M4	$2.66\times10^{+13}$	$1.44\times10^{+12}$	$2.98\times10^{+10}$	$8.46\times10^{+09}$	$2.29\times10^{+09}$	$1.35\times10^{+09}$	$1.19\times10^{+9}$
M5	$2.82\times10^{+21}$	$7.96\times10^{+19}$	$6.97\times10^{+17}$	$1.50\times10^{+17}$	$3.03\times10^{+16}$	$1.59\times10^{+16}$	$1.36\times10^{+16}$

	175 keV	196 keV	205 keV	257 keV	260 keV	267 keV
E1	6.55×10^{-14}	4.66×10^{-14}	4.07×10^{-14}	2.07×10^{-14}	1.95×10^{-14}	1.84×10^{-14}
E2	1.55×10^{-07}	8.81×10^{-8}	7.04×10^{-08}	2.27×10^{-8}	2.06×10^{-8}	1.88×10^{-8}
E3	0.558	0.253	0.184	0.038	0.033	0.029
E4	$3.02\times10^{+06}$	$1.09\times10^{+6}$	$7.28\times10^{+05}$	$9.52\times10^{+4}$	$8.00\times10^{+4}$	$6.75\times10^{+4}$
E5	$2.31\times10^{+13}$	$6.65\times10^{+12}$	$4.06\times10^{+12}$	$3.37\times10^{+11}$	$2.73\times10^{+11}$	$2.22\times10^{+11}$
M1	7.31×10^{-13}	5.83×10^{-13}	5.33×10^{-13}	3.39×10^{-13}	3.26×10^{-13}	3.14×10^{-13}
M2	9.91×10^{-06}	5.62×10^{-6}	4.49×10^{-06}	1.45×10^{-6}	1.32×10^{-6}	1.2×10^{-6}
M3	35.7	16.1	11.8	2.42	2.12	1.85
M4	$1.93\times10^{+08}$	$6.97\times10^{+7}$	$4.65\times10^{+07}$	$6.09\times10^{+6}$	$5.12\times10^{+6}$	$4.32\times10^{+6}$
M5	$1.48\times10^{+15}$	$4.25\times10^{+14}$	$2.59\times10^{+14}$	$2.16\times10^{+13}$	$1.74\times10^{+13}$	$1.42\times10^{+13}$

Table 5.3: *Calculated total conversion coefficients [142] for the transitions observed in ^{84}Nb.*

	47 keV	65 keV	100 keV	114 keV	132 keV	140 keV	143 keV
E1	1.06	0.422	0.121	0.0805	0.0527	0.0445	0.0427
E2	17.5	5.51	1.17	0.702	0.414	0.335	0.318
E3	420	83.1	10.9	5.78	3.00	2.31	2.17
E4	$1.27\times10^{+4}$	$1.59\times10^{+3}$	119	53.3	23.6	17.1	15.9
M1	2.05	0.802	0.237	0.161	0.108	0.0922	0.0887
M2	42.4	12.2	2.44	1.47	0.872	0.709	0.675
M3	715	159	22.7	12.2	6.49	5.04	4.74
M4	1410	2270	220	105	49.5	36.7	34.1

	175 keV	196 keV	205 keV	257 keV	260 keV	267 keV
E1	0.0238	0.0172	0.0151	8.01×10^{-3}	7.59×10^{-3}	7.21×10^{-3}
E2	0.154	0.102	0.0871	0.0393	0.0368	0.0345
E3	0.891	0.544	0.449	0.172	0.159	0.147
E4	5.37	2.96	2.35	0.754	0.685	0.625
M1	0.0516	0.0383	0.0340	0.0190	0.018	0.0172
M2	0.334	0.227	0.195	0.0925	0.0869	0.0818
M3	2.01	1.25	1.04	0.419	0.388	0.360
M4	12.3	7.03	5.64	1.91	1.74	1.60

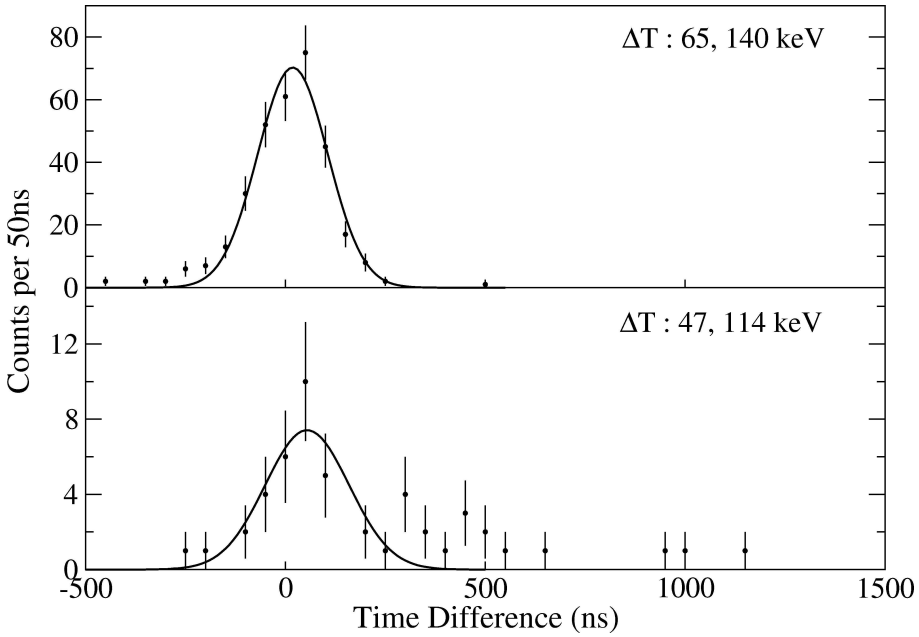

Figure 5.11: *Time difference spectra between the 65 and 140 keV transitions (Upper panel) and the 47 and 114 keV transitions (Lower panel) in ^{84}Nb. The counts which appear with a large time difference indicate the 47 keV state is isomeric.*

figure 5.10. The upper panel is the DGF time spectrum associated with the 132 and 175 keV transitions. The deduced mean lifetime in the current work of 109 (5) ns is consistent with the previous measurement by Chandler *et al.* of 148 (28) ns.

The 47 keV transition appears to have a longer mean lifetime than the other transitions which indicates the 47 keV state is also isomeric. Figure 5.11 shows the time difference spectra between the 65 and 140 keV transitions and the 47 and 114 keV transitions. Despite the low coincidence statistics, a significant number of counts appear to the right of the centroid in the lower panel which are absent in the upper. This is an indication that the 47 keV state has a mean lifetime associated with it and the apparent mean lifetime in figure 5.10 is not due to feeding from the longer-lived isomeric state at 771 keV. Feeding from the 109 (5) ns isomeric state at 337 keV must be taken into account so a two-component least-squares fit has been used in this case. The mean lifetime of 329 (87) ns suggests the multipolarity of the decay to be a hindered E1 (see Table 5.2). The mean lifetime of the 771 keV state has been obtained by a least-squares fit to the 196, 257 and 267 keV transitions and is found to be 223 (35) ns.

The 566 keV level has been established by Mărginean *et al.* to have a spin/parity

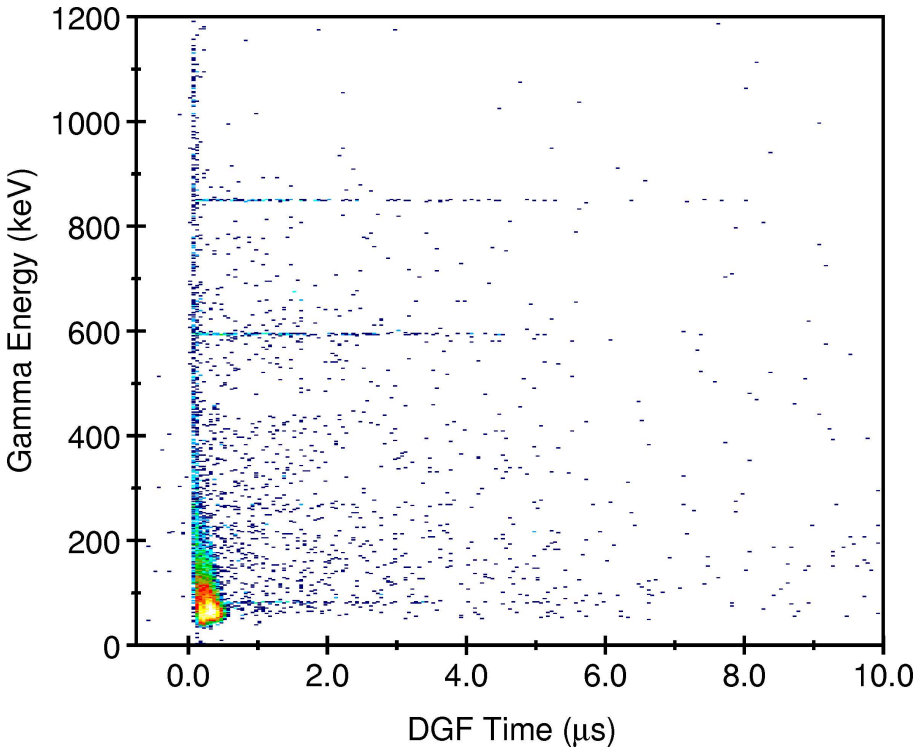

Figure 5.12: *Energy vs DGF time plot gated on ions identified as ^{86}Tc.*

of (6^-) from the DCO ratios of the relevant gamma rays. No spin or parity is suggested for the 771 keV state. Table 5.2 shows the calculated partial half-lives of the transitions observed in ^{84}Nb in the current work. The spin of the 771 keV isomeric state is most likely 7^+ on the basis of decay multipolarity arguments.

5.3 Results for $^{86}_{43}$Tc$_{43}$

The primary aim of this experiment was to observe and confirm the isomeric decay of ^{86}Tc and gain insight into the low-lying structure of this nucleus. When a gamma-ray spectrum is created, gated on ions identified as ^{86}Tc, several gamma rays are observed, see figure 5.12.

Figure 5.13 is a gamma-ray spectrum produced by a projection of energies detected between 200 ns and 11.05 μs following implantation of the associated ion. The two gamma-ray transitions identified by Chandler *et al.* are confirmed here as originating from the isomeric decay of ^{86}Tc. The gamma rays of 593 and 850 keV lie notably close in energy to the $2^+ \rightarrow 0^+$ (567 keV) and $4^+ \rightarrow 2^+$ (761 keV) isobaric analogue transitions in $^{86}_{42}$Mo$_{44}$ [149]. On this basis they are assigned to be the first two

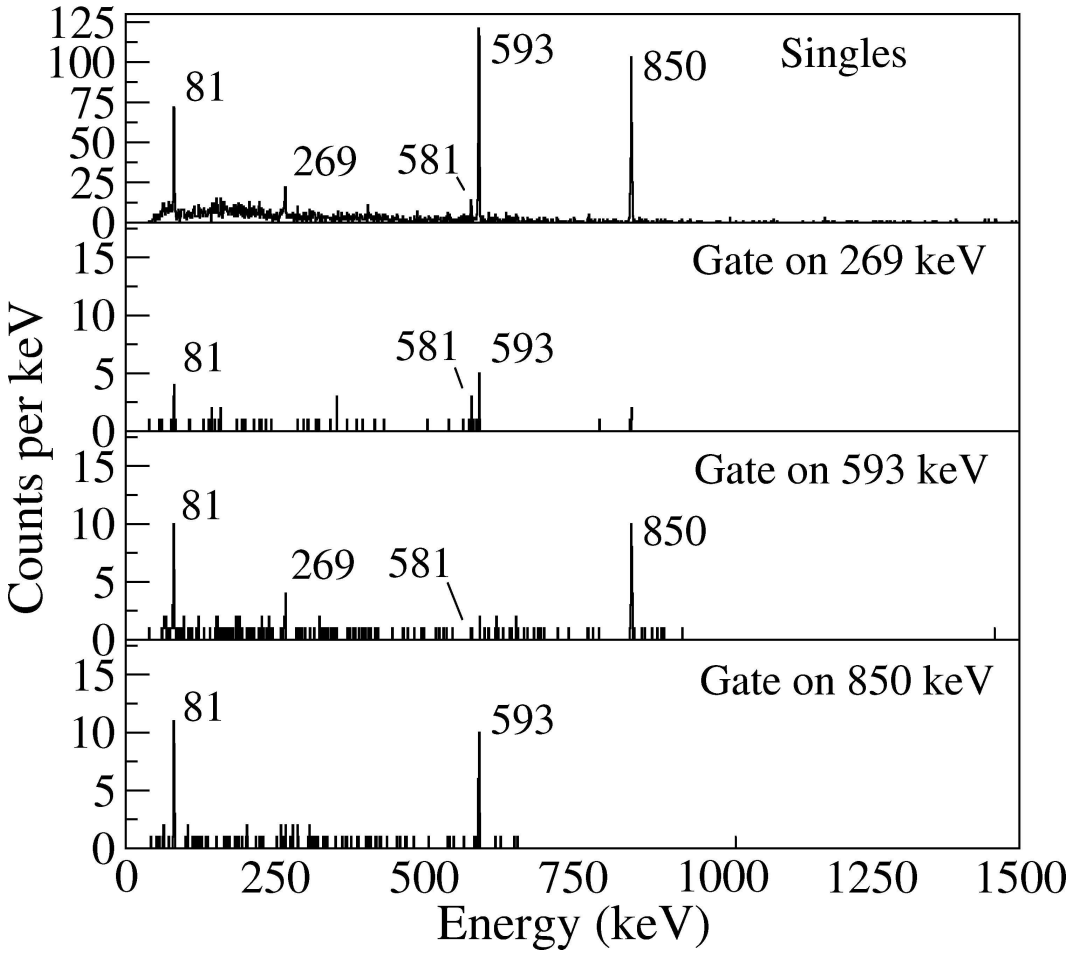

Figure 5.13: *Singles and coincidence gamma-ray spectra gated on ions identified as ^{86}Tc and a time gate between 200 ns and 11.05 μs.*

transitions of the T=1 ground-state band in ^{86}Tc.

Several other gamma rays can also be identified in this spectrum and assigned to ^{86}Tc. Most significant is the intense gamma ray with an energy of 81 keV. Figure 5.14 shows a least-squares fit to the decay curve of the 593 and 849 keV gamma rays. The mean lifetime of the isomeric state is found to be 1.59 (20) μs.

A gamma-gamma coincidence analysis has been performed and the gates shown in figure 5.13 indicate that the gamma rays with energies 81, 593 and 849 keV are all in mutual coincidence. A timing condition on this matrix only allows gamma rays detected after 200 ns following the arrival of ions in the stopper to be included in this matrix. Events must be time correlated to within 200 ns of each other to be included.

The fact that the 269 and 581 keV gamma-ray energies sum to 850 keV suggests a competing decay branch to the $(4^+) \rightarrow (2^+)$ transition and this is confirmed in the

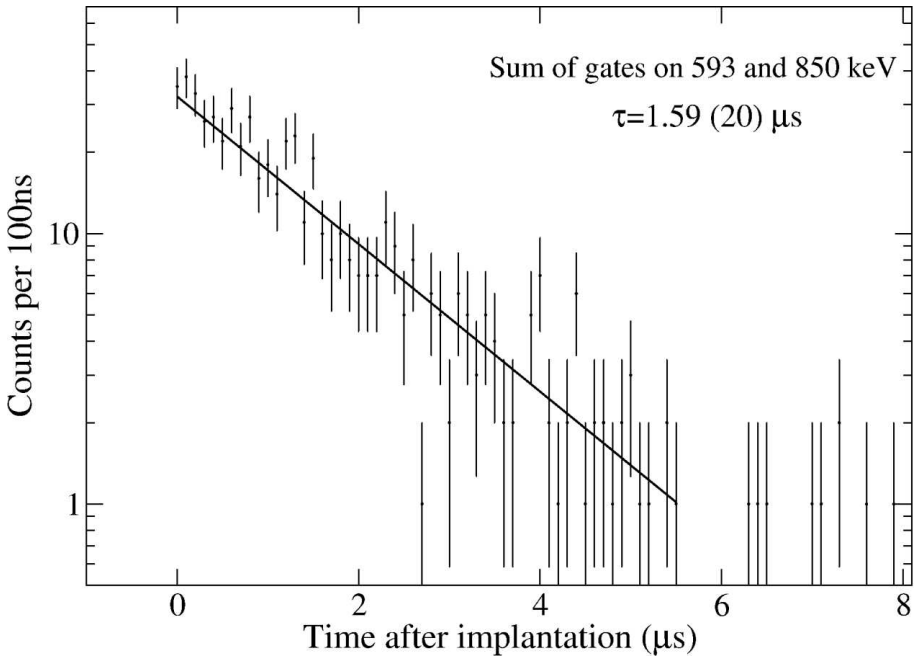

Figure 5.14: *DGF-timing spectrum with energy gates on the 593 and 849 keV gamma rays in the isomeric decay of ^{86}Tc.*

gamma-gamma coincidence data. The spin and parity of this state is most likely 3^+ or 4^+ when gamma-ray selection rules and Weisskopf estimates of the transitions are considered (Table 5.4).

An intensity balance around the (4^+) state has been used to infer the conversion coefficient, α_{TOT}, of the 81 keV gamma ray to be 3.13(17) (for further explanation see Appendix A). Calculated values of total conversion coefficients for this transition are displayed in Table 5.5 [142]. On this basis the 81 keV transition in ^{86}Tc is assigned to be of stretched-E2 multipolarity, leading to a spin/parity assignment of (6^+) for the isomeric state.

The $I^\pi = 6^+$ member of the ground-state band in ^{86}Mo lies at 2260 keV, 932 keV above the 4^+ state. Considering the similarity in energy of the (2^+) and (4^+) members the T=1, $I^\pi = 6^+$ state in ^{86}Tc would therefore be expected to have an excitation energy of around 2.5 MeV. The isomeric 6^+ state appears at an excitation energy of 1524 keV creating an yrast-trap isomeric state. The fact that this 6^+ state appears only 81 keV above the yrast 4^+ state would explain the somewhat large isomeric ratio (Table 5.9).

The results of a shell model calculation for ^{86}Tc [141] is shown in figure 5.15.

Table 5.4: *Partial half-lives of transitions in ^{86}Tc for various multipolarities of different gamma-ray energies derived from the single particle unit Weisskopf estimates. The units are seconds.*

	81 keV	269 keV	581 keV	593 keV	849 keV
E1	6.26×10^{-13}	1.77×10^{-14}	1.76×10^{-15}	1.66×10^{-15}	5.64×10^{-16}
E2	6.66×10^{-06}	1.75×10^{-08}	3.73×10^{-10}	3.37×10^{-10}	5.60×10^{-11}
E3	$1.07\times10^{+02}$	2.63×10^{-02}	1.20×10^{-04}	1.04×10^{-04}	8.42×10^{-06}
E4	$2.61\times10^{+09}$	$5.93\times10^{+04}$	$5.80\times10^{+01}$	$4.82\times10^{+01}$	1.91
E5	$8.94\times10^{+16}$	$1.89\times10^{+11}$	$3.96\times10^{+07}$	$3.16\times10^{+07}$	$6.10\times10^{+05}$
M1	3.33×10^{-12}	3.10×10^{-13}	6.64×10^{-14}	6.37×10^{-14}	3.11×10^{-14}
M2	4.32×10^{-04}	1.14×10^{-06}	2.42×10^{-08}	2.18×10^{-08}	3.63×10^{-09}
M3	$6.97\times10^{+03}$	1.71	7.78×10^{-03}	6.74×10^{-03}	5.47×10^{-04}
M4	$1.69\times10^{+11}$	$3.85\times10^{+06}$	$3.76\times10^{+03}$	$3.13\times10^{+03}$	$1.24\times10^{+02}$
M5	$5.81\times10^{+18}$	$1.23\times10^{+13}$	$2.57\times10^{+09}$	$2.05\times10^{+09}$	$3.96\times10^{+07}$

Table 5.5: *Calculated total conversion coefficients [142] for the transitions observed in ^{86}Tc.*

	81 keV	269 keV	581 keV	593 keV	849 keV
E1	0.245	7.91×10^{-03}	1.12×10^{-03}	1.06×10^{-03}	4.91×10^{-04}
E2	2.69	3.71×10^{-02}	3.30×10^{-03}	3.12×10^{-03}	1.22×10^{-03}
E3	32.3	1.56×10^{-01}	8.73×10^{-03}	8.16×10^{-03}	2.72×10^{-03}
E4	481	0.663	2.26×10^{-02}	2.09×10^{-02}	5.85×10^{-03}
M1	0.514	1.99×10^{-02}	3.03×10^{-03}	2.89×10^{-03}	1.27×10^{-03}
M2	6.42	9.48×10^{-02}	9.13×10^{-03}	8.62×10^{-03}	3.23×10^{-03}
M3	69.8	0.414	2.47×10^{-02}	2.31×10^{-02}	7.27×10^{-03}
M4	814	1.82	6.52×10^{-02}	6.02×10^{-02}	1.58×10^{-02}

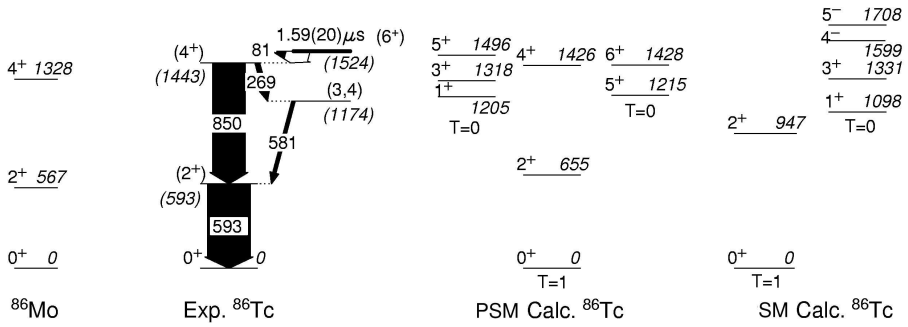

Figure 5.15: *Experimental and theoretical (Shell model and Projected Shell Model) level schemes of ^{86}Tc. The ground-state band of ^{86}Mo is also shown for comparison.*

The valence space used in the calculation included only the $g_{9/2}$ and $p_{1/2}$ orbitals. As in the case of ^{82}Nb this limited valence space does not provide sufficent collectivity to accurately reproduce the observed ground-state band energies.

A potential energy surface calculation has been performed for ^{86}Tc and the result for the ground state is shown to the left of figure 5.16. The minimum for a rotational frequency of $\omega = 0.0$ MeV/$\hbar$ is at $\beta_2 = 0.004$, $\gamma = -120.0$ and $\beta_4 = -0.001$. However if the system is allowed to rotate then the minimum quickly moves to the triaxially soft, prolate minimum focused around $\beta_2 \approx 0.2$ which is indicated to the right of figure 5.16. This soft triaxial shape suggests that $N = Z = 43$ represents the boundary along the $N = Z$ line of the transitional region as the doubly-magic ^{100}Sn is approached. These findings are in agreement with recent results described by Fischer *et al.* [150].

The positive parity states in ^{86}Tc predicted by the Projected Shell Model are shown in figure 5.15. Negative parity states with $K = 5, 6$ are also predicted at ≈1.2 MeV but are not shown in the figure. The ground-state band is shown to be well reproduced in the calculation. The $I^\pi = 6^+$ state predicted at 1428 keV is the first member of a rotational band built on the $I^\pi = 5^+$ 2-quasiparticle band head ($\nu[422]5/2^+ \times \pi[422]5/2^+$) and therefore seems unlikely to be isomeric. A more probable configuration for a $I^\pi = 6^+$ isomeric state would be a coupling of the $[413]7/2^+ \times [422]5/2^+$ Nilsson orbitals. Both of these orbitals lie close to the Fermi surface but the calculation places this state at a significantly higher excitation energy.

It is also noteworthy that the isomeric state in ^{86}Tc lies above the proton separation energy of 1393 (409) keV [4] thus unlocking the possibility of direct proton

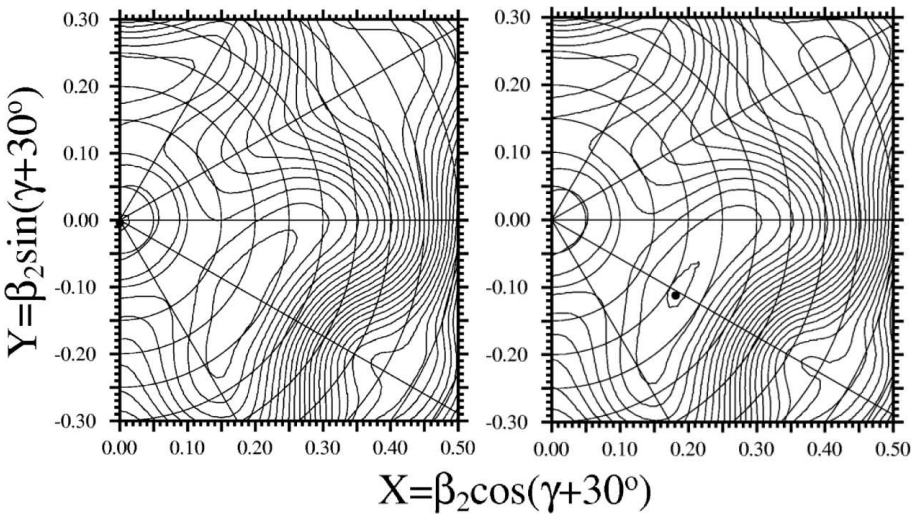

Figure 5.16: *A configuration-constrained potential-energy-surface calculation for the ground state of ^{86}Tc ($\omega = 0.0$ MeV/$\hbar$) and $\omega = 0.198$ MeV/$\hbar$. The minimum is at $\beta_2 = 0.004$, $\gamma = -120.0$ and $\beta_4 = -0.001$ for the ground state but moves to the shallow minimum centred around $\beta_2 = 0.213$, $\gamma = -61.6$ and $\beta_4 = -0.050$ if $\omega > 0$ MeV/$\hbar$. The spacing between the contour lines corresponds to 200 keV.*

emission from the isomer competing with internal gamma-ray decay. Such a competing decay branch would speed up the apparent mean lifetime of the isomeric state and could explain the absence of any K-hindrance. Unfortunately this possibility cannot be confirmed in the current experiment.

5.4 Results for $^{87}_{43}$Tc$_{44}$

A number of gamma rays, forming deformed bands, have been observed in this nucleus previously [151] but no linking transitions to the ground state were identified. The nuclei were produced in fusion-evaporation reactions and populated via the $p2n$ evaporation channel with a cross section of around a hundred millibarns. The prompt gamma-ray decays were observed with Ge detectors and the reaction products were identified using the Daresbury separator and energy loss measurements in an ionization chamber. The experimental set up used was only sensitive to gamma rays between 0.1 and 2.4 MeV which were emitted in the first 0.5 ns following production.

The current work identifies two delayed gamma rays associated with ^{87}Tc which

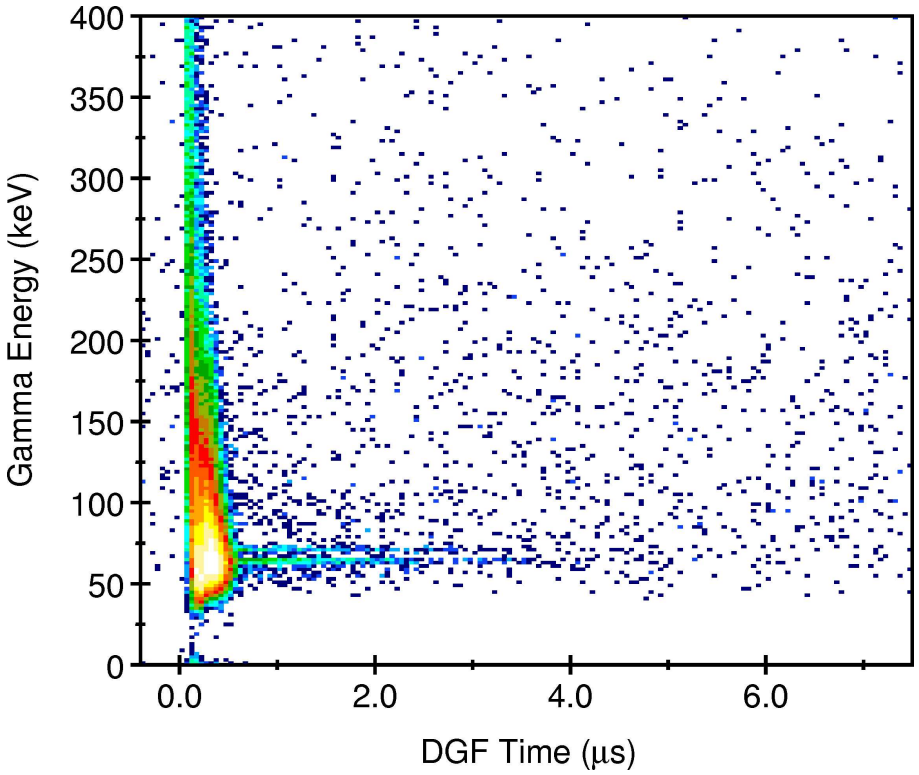

Figure 5.17: *Energy vs DGF time plot gated on ions identified as ^{87}Tc.*

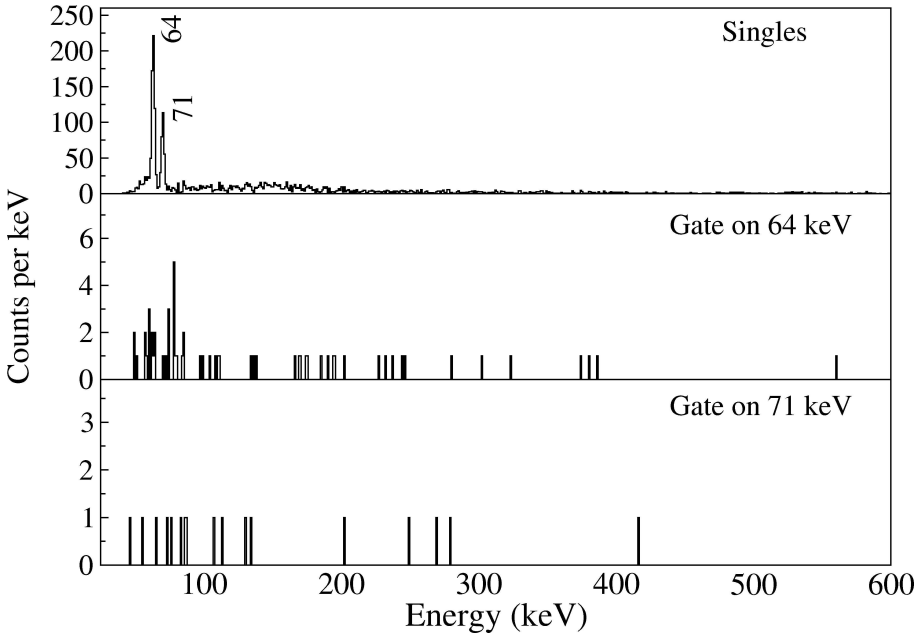

Figure 5.18: *Gamma-ray spectrum gated on ions identified as ^{87}Tc and a time gate between 200 ns and 2.3 μs. The upper spectrum is gamma singles and the lower two spectra are energy coincidence gates (indicated in the panels) which show a null coincidence between the two gamma rays.*

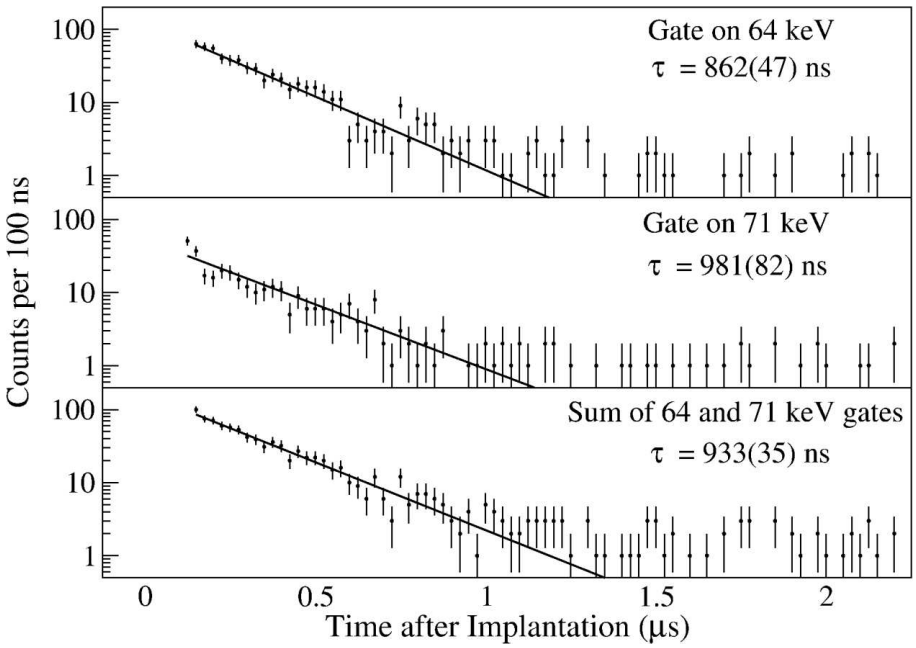

Figure 5.19: *Mean lifetime fits on the individual gamma rays observed in the decay of an isomeric state in ^{87}Tc and on the sum of the two.*

can be seen in the energy vs DGF time matrics in figure 5.17 and gamma-ray projection in figure 5.18. The two transitions of 64 and 71 keV are found not to be in coincidence with each other (see inset of figure 5.18). This consitutes either separate decay paths from an isomeric state or represent the decay of two isomeric states in ^{87}Tc. Least-squares fits to the decay curves associated with the individual gamma rays, shown in figure 5.19, finds their mean lifetimes however to be the same within experimental uncertainties. The most likely scenario is therefore a single isomeric state with competing decay paths. A single component mean lifetime fit to the summed decay curve (figure 5.19) gives a mean lifetime measurement of 933 (35) ns.

An inspection of the calculated partial half-lives (table 5.6) of these observed gamma rays indicates that only hindered E1 or M1 multipolarity can result in the observed mean lifetime of the isomeric state. Other multipolarities would result in a much longer-lived isomer. E1 and M1 transitions require a large degree of hindrance which is unlikely for M1 transitions in this region [152]. Therefore E1 assignment for both gamma rays is suggested.

Table 5.6: *Partial half-lives for transitions in ^{87,88}Tc of various multipolarities derived from the single particle unit Weisskopf estimates. The units are seconds.*

	^{87}Tc			^{88}Tc
	7 keV	64 keV	71 keV	95 keV
E1	6.69×10^{-10}	1.31×10^{-12}	9.18×10^{-13}	3.97×10^{-13}
E2	7.42×10^{-01}	2.26×10^{-05}	1.26×10^{-05}	3.09×10^{-06}
E3	$1.25\times10^{+09}$	$5.95\times10^{+02}$	$2.61\times10^{+02}$	$3.66\times10^{+01}$
E4	$3.16\times10^{+18}$	$2.35\times10^{+10}$	$8.15\times10^{+09}$	$6.52\times10^{+08}$
E5	$1.13\times10^{+28}$	$1.31\times10^{+18}$	$3.60\times10^{+17}$	$1.64\times10^{+16}$
M1	3.50×10^{-10}	5.47×10^{-12}	4.32×10^{-12}	2.48×10^{-12}
M2	$4.85\times10^{+01}$	1.48×10^{-03}	8.21×10^{-04}	2.04×10^{-04}
M3	$8.16\times10^{+10}$	$3.89\times10^{+04}$	$1.71\times10^{+04}$	$2.41\times10^{+03}$
M4	$2.07\times10^{+20}$	$1.54\times10^{+12}$	$5.34\times10^{+11}$	$4.30\times10^{+10}$
M5	$7.39\times10^{+29}$	$8.60\times10^{+19}$	$2.35\times10^{+19}$	$1.08\times10^{+18}$

Table 5.7: *Calculated total conversion coefficients for transitions in ^{87,88}Tc.*

	^{87}Tc			^{88}Tc
	7 keV	64 keV	71 keV	95 keV
E1	24.4	0.482	0.344	0.155
E2	$4.32\times10^{+04}$	6.25	4.10	1.52
E3	$1.68\times10^{+07}$	$1.01\times10^{+02}$	56.8	15.2
E4	$2.79\times10^{+09}$	$2.09\times10^{+03}$	996	184
M1	62.0	1.01	0.718	0.327
M2	$3.20\times10^{+04}$	15.6	10.0	3.55
M3	$1.70\times10^{+07}$	$2.05\times10^{+02}$	119	34.1
M4	$3.92\times10^{+09}$	$2.98\times10^{+03}$	$1.55\times10^{+03}$	$3.44\times10^{+02}$

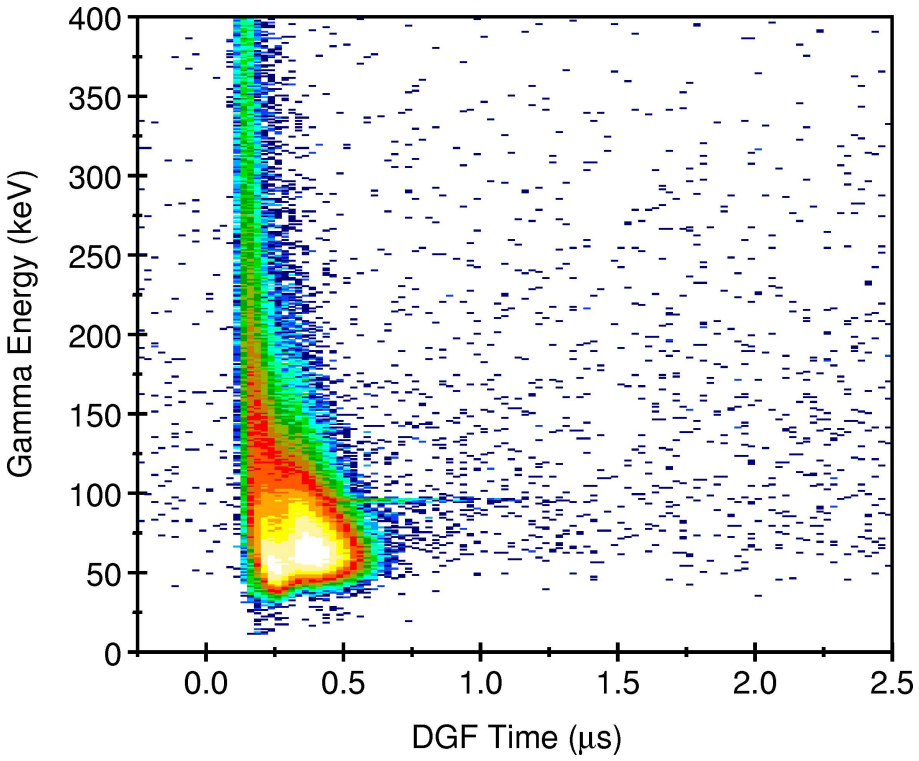

Figure 5.20: *Energy vs DGF time plot gated on ions identified as ^{88}Tc.*

5.5 Results for $^{88}_{43}Tc_{45}$

Two beta-decaying states with half-lives of 6.4 and 5.8 s are known in this odd-odd nucleus [153]. In addition a quasirotational band was identified in an in-beam study [151]. It is not clear which state, if either, is the ground state or to which state the quasirotational band decays.

In the current work a 211 (18) ns isomeric state is found to decay via a 95 keV gamma ray (see figures 5.20 and 5.21). An inspection of the Weisskopf estimates (Table 5.6) for this transition suggests an E1 multipolarity. The E1 strength would therefore be B(E1) = 2.64×10^{-5} W.u. which is well below the recommended upper limit for this mass region of 10 mW.u. [152]. This value also compares well with E1 transitions in neighbouring nuclei such as the $4^+ \rightarrow 3^-$ transition (1.7×10^{-7} W.u.) in ^{76}Rb [154] or the $2^+ \rightarrow 1^-$ transition (1.34×10^{-7} W.u.) in ^{80}Y [39].

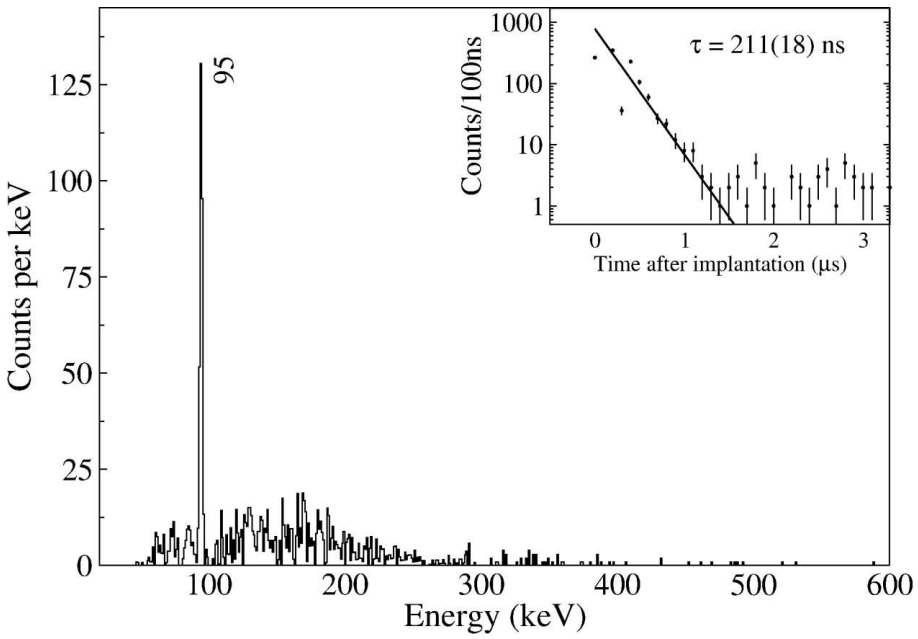

Figure 5.21: *Gamma-ray spectrum gated on ions identified as ^{88}Tc and a time gate between 200 ns and 2.3 μs. The inset is the associated DGF time spectrum gated on the 95 keV gamma ray.*

Table 5.8: *Summary of E1 transitions identified in the current work. In all cases the branching ratio is assumed to be 100%.*

Nucleus	E_γ (keV)	$J_i^\pi \rightarrow J_f^\pi$	B(E1) (W.u.)
^{87}Tc	64		1.48×10^{-6}
^{87}Tc	71		1.00×10^{-6}
^{88}Tc	95		2.34×10^{-6}
^{84}Nb	47	$(4^-) \rightarrow (3^+)$	4.27×10^{-6}
^{84}Nb	132	$(5^-) \rightarrow (4^+)$	9.03×10^{-7}
^{84}Nb	196	$(7^+) \rightarrow (6^-)$	1.42×10^{-7}
^{84}Nb	205	$(7^+) \rightarrow (6^-)$	1.24×10^{-7}

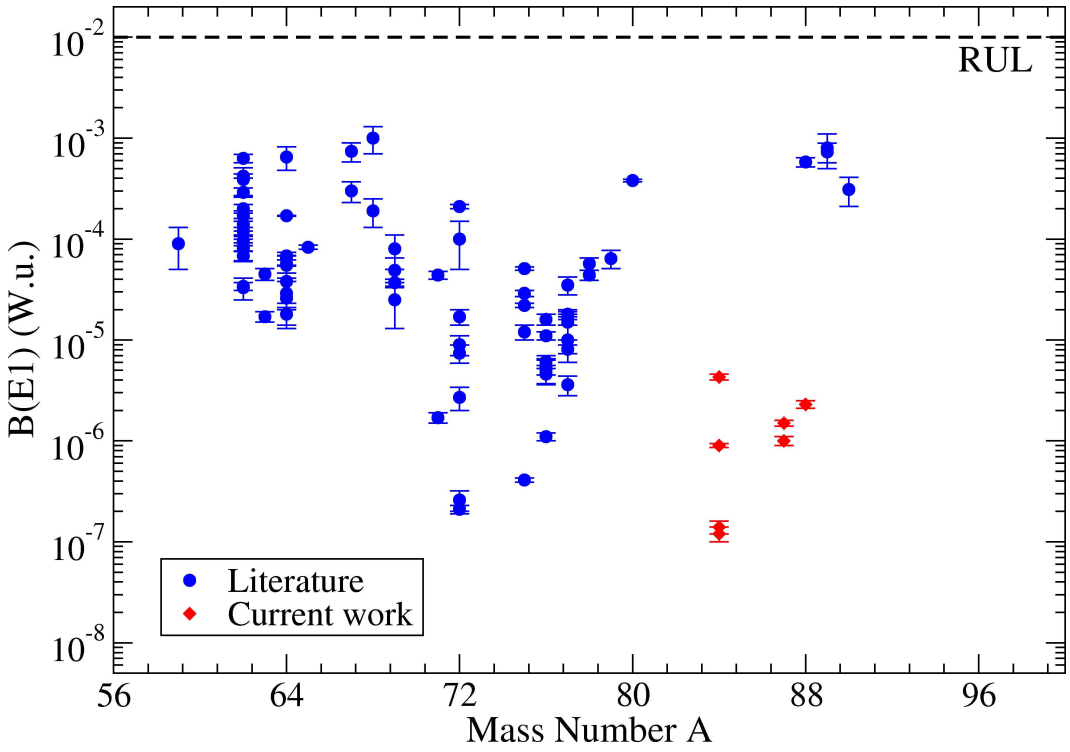

Figure 5.22: *Strengths of E1 transitions in the fpg shell from reference [152] and from the current work. The dashed line indicates the Recommended Upper Limit (RUL) for E1 transition strengths in $A = 45 \rightarrow 90$ nuclei.*

5.6 Hindered E1 Transitions in the $A \sim 80$ Region

The work of this thesis has identifed a number of E1 transitions which have not been previously reported. All of these transitions appear somewhat hindered when compared to single-particle Weisskopf estimates which is consistent with previously observed E1 transitions in this mass region. A summary of the E1 transitions found in the current work is listed in table 5.8. These transition strengths are plotted along with other E1 transitions in the fpg shell in figure 5.22.

5.7 Neutron-Proton Interactions

These new data provide strong evidence for a $T = 1$, np pairing condensate in ^{82}Nb and ^{86}Tc. This is a continuation of the trend seen in the lighter odd-odd $N = Z$ nuclei of the *fpg* shell. Figure 5.23 shows the deformation calculated from the empirical relationship described by Raman *et al.* [155] for the $N = Z$ nuclei in the *fpg* shell, excitation energy of the first 2^+ state and the E(4^+)/E(2^+) ratio. The remarkable similarity in the structure of the odd-odd nuclei and their even-even neighbours is striking in this plot. Only here along the $N = Z$ line is any resemblance at all seen in the pattern of excited states in an odd-odd and an even-even nucleus.

The lowest $T = 0$ states to be observed in ^{82}Nb and ^{86}Tc are at 1180 and 1174 keV respectively. These new data are included in the plot (shown previously in figure 1.4) of the energy difference between the lowest observed $T = 0$ and $T = 1$ states in odd-odd $N = Z$ nuclei plotted against mass number shown in figure 5.24. The same data plotted against valence product, $N_{\pi \bullet} N_{\nu}$, is shown in figure 5.25.

It has been suggested by Jenkins *et al.* [20] that the low level density found in the first MeV above the ground state in odd-odd, $N = Z$ nuclei is a signiture of neutron-proton pairing. Figure 8 of reference [20] compares the number of levels observed experimentally in the most neutron-deficient Br, Rb and Y isotopes. The number of levels in the T_z=0 members is 1 or 3 levels compared to an average of more than 30 in the other nuclei. In these examples each case has been investigated using similar reaction mechanisms and experimental set-ups of equal sensitivity thus excluding the possibility of the observed low level density being an experimental shortcoming.

A similar comparison is made here for the Y, Nb, Tc and Rh isotopes. Figure

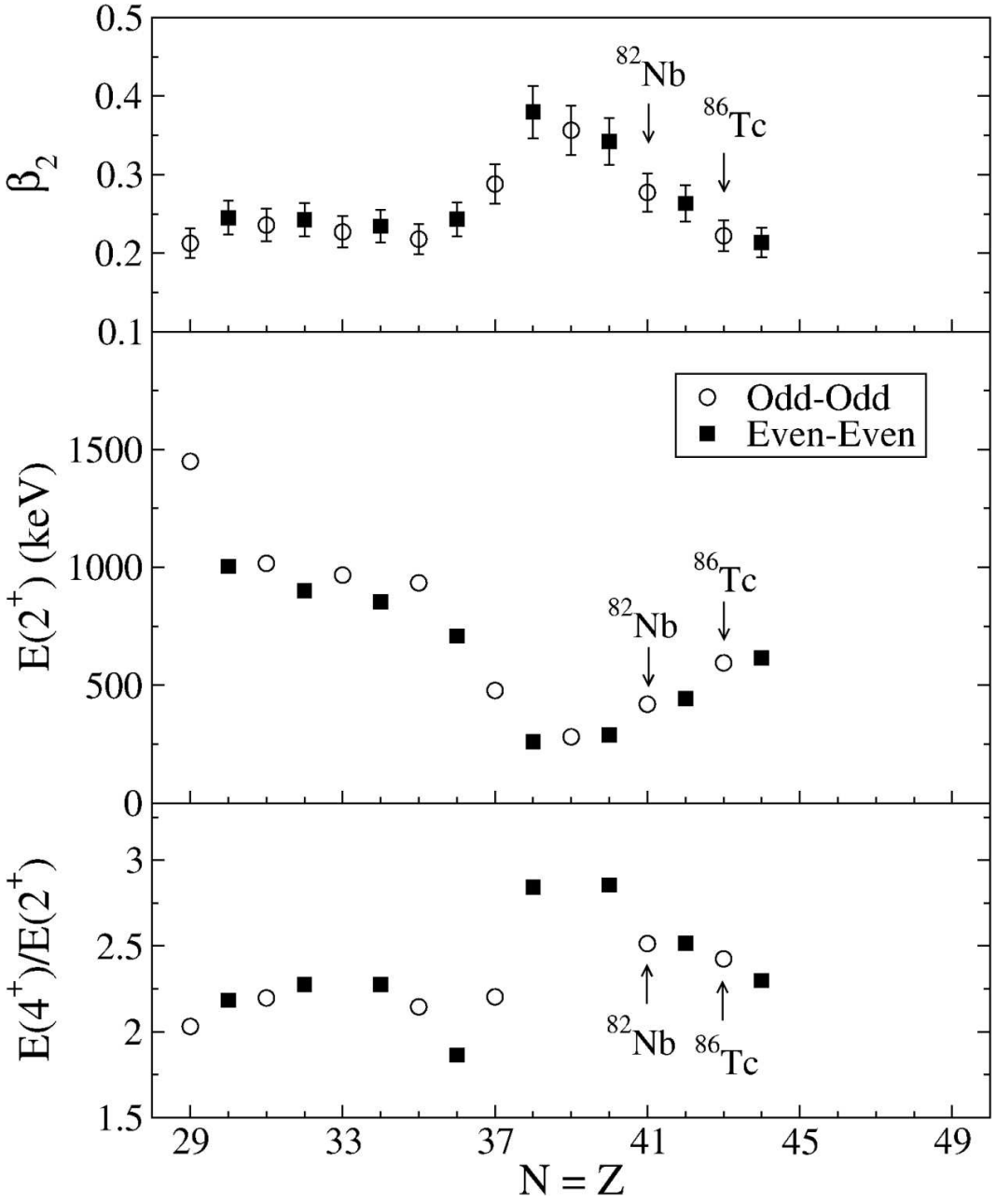

Figure 5.23: *Structural evolution of the $N = Z$ nuclei across the fpg shell;* **Upper:** *Deformation calculated using the empirical relationship described in reference [155],* **Central:** *Excitation energy of the first $I^{\pi} = 2^{+}$ state, and* **Lower:** *$E(4^{+})/E(2^{+})$ ratio. Note the value of the 2^{+} energy of ^{58}Cu has been adjusted due to the 0^{+} state being an excited state at 203 keV above the ground state.*

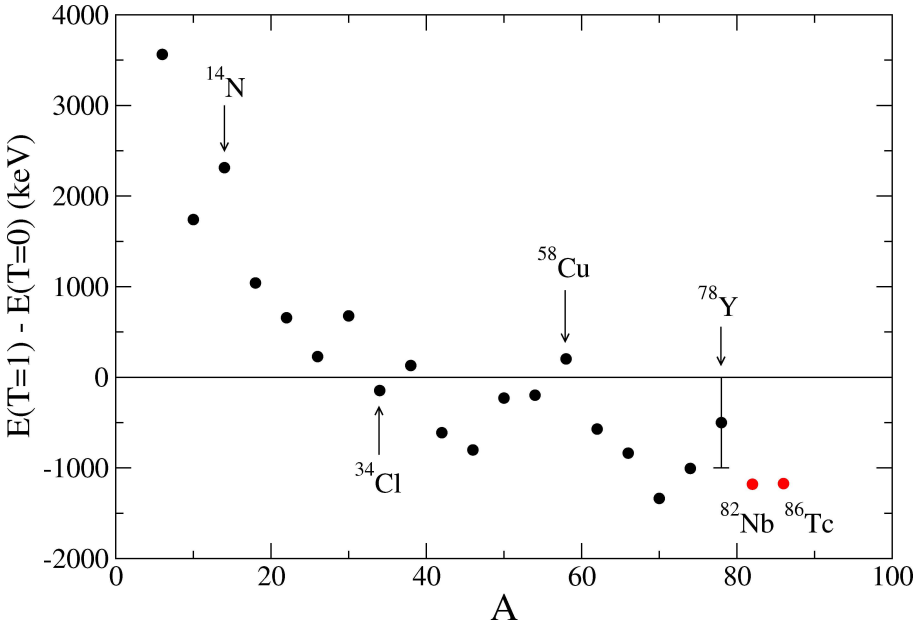

Figure 5.24: *Energy difference between the lowest observed $T = 0$ and $T = 1$ states in odd-odd $N = Z$ nuclei plotted against mass number. Nuclei with positive energy differences have $T = 0$ ground states, those with negative energy differences have $T = 1$ ground states.*

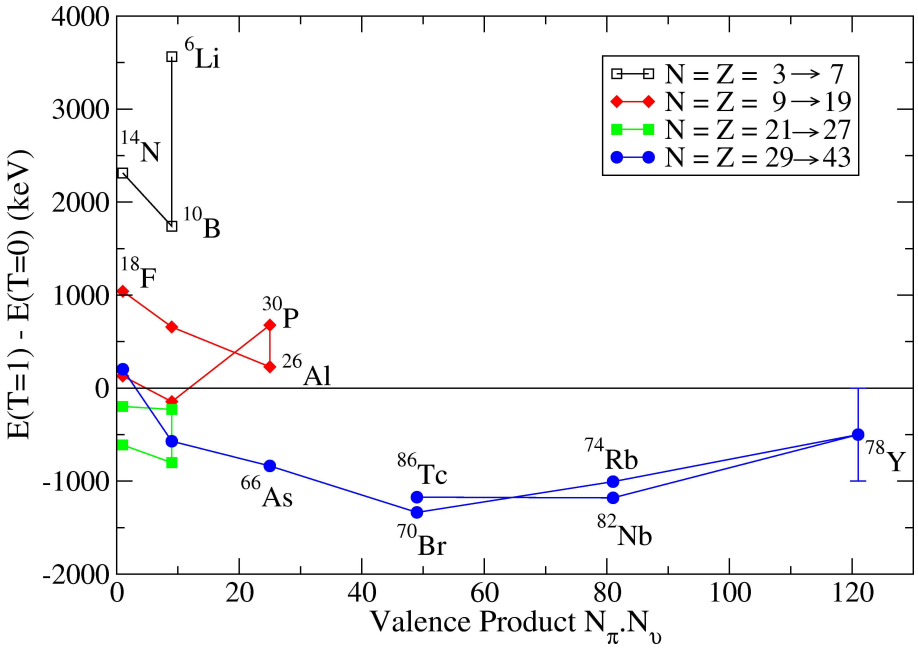

Figure 5.25: *Energy difference between the lowest observed $T = 0$ and $T = 1$ states in odd-odd $N = Z$ nuclei plotted against valence product.*

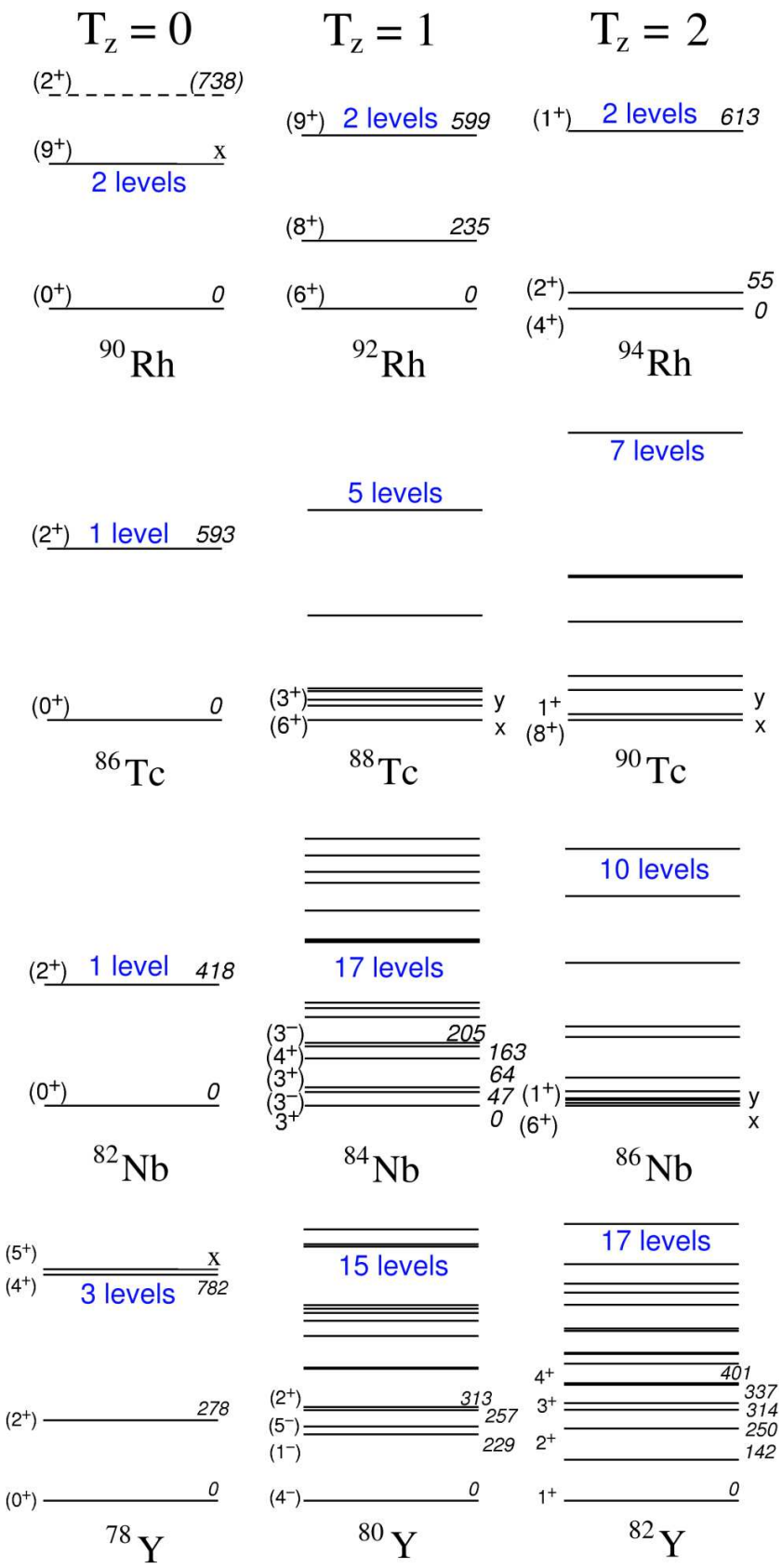

Figure 5.26: *Experimentally identified energy levels below 1 MeV in the $T_z = 0, 1$ and 2 isotopes of Y, Nb, Tc and Rh.*

5.26 shows the experimentally observed levels in the $T_z = 0, 1$ and 2 isotopes which lie below 1 MeV of excitation. The data come from references [26, 147, 156, 157, 158, 159, 160, 161, 162, 163, 164, 165] and the current work. Although a lower level density is noted for the $N = Z$ cases, the Tc and Rh nuclei have not been investigated in such a comprehensive manner as in the lighter elements. This unfortunately means the rigourous comparison necessary to confirm a low level density resulting from a neutron-proton pairing gap cannot yet be made. In Y and Nb a significant difference is observed. It must be remembered that the experimental investigation of ^{82}Nb was only sensitive to the decay of isomeric states therefore other states may exist which are simply not populated. However the decay of the 337 keV isomeric state in ^{84}Nb populates 4 states which means an experiment only sensitive to isomeric decays would identify 5 excited states below 337 keV in this $T_z = 1$ nucleus compared to 3 states below 1180 keV in the $T_z = 0$ case.

Taking all these considerations into account there does seems to be a consistent and persistant energy difference between the lowest $T = 1$ and first $T = 0$ state in the heaviest $N = Z$ nuclei of around 1 MeV. This is suggested as reasonable evidence for a $T = 1$, np pairing gap in self-conjugate nuclei in the fpg shell.

5.8 Determination of Isomeric Ratios

The reaction mechanism of projectile fragmentation has been found to populate primarily the yrast states in the product nuclei [140, 166, 167]. Measurements of isomeric ratios can give insight into both the reaction process and the structure of the observed isomeric states. The isomeric ratio, R, is defined as [140],

$$R = \frac{N_{isomer}}{N_{ions} F G}, \tag{5.1}$$

where N_{isomer} is the total number of ions produced in the isomeric state, N_{ions} is the total number of ions of that nuclear species produced and F and G are correction factors for in-flight losses and for a finite measuring time respectively. The number of ions produced in the isomeric state is equal to [140],

$$N_{isomer} = \frac{N_{\gamma_i}}{\epsilon_i} \frac{(1+\alpha_i)}{b_\gamma}, \tag{5.2}$$

where N_{γ_i} is the number of gamma rays observed in the decay of the i^{th} decay branch depopulating the isomeric state, ϵ_i is the absolute efficiency of the germanium detectors at that energy, b_γ is the branching ratio of the gamma-ray transition and α_i is the internal conversion coefficient of that gamma-ray transition. The correction for in-flight losses is,

$$F = \exp\left[-\left(\lambda^{q1}\frac{TOF_1}{\gamma_1} + \lambda^{q2}\frac{TOF_2}{\gamma_2}\right)\right] \tag{5.3}$$

where λ is the decay constant for the nucleus with charge state q. The finite gamma-ray measuring time period is accounted for by,

$$G = \exp(-\lambda t_i) - \exp(-\lambda t_f) \tag{5.4}$$

where t_i and t_f are the times of the start and finsh of the measurement respectively.

In some cases a nucleus may have two isomeric states which are populated in an experiment. The decay of a higher-lying isomer may populate a lower-lying isomeric state and this feeding must be accounted for in the determination of the isomeric ratios. In the work of this thesis ^{84}Nb (section 5.2) is such a case where this must be considered. The isomeric ratio of the lower-lying isomer, R_L, is determined by [140]

$$R_L = \frac{Y_L}{N_{ions}F_L G_L} - b_{UL}\frac{R_U}{F_L G_L}\left[\frac{\lambda_L G_U - \lambda_U G_L}{\lambda_L - \lambda_U}F_U + \frac{\lambda_U^0}{\lambda_L^0 - \lambda_U^0}G_L(F_U - F_L)\right], \tag{5.5}$$

where the indix, U, refers to the upper isomeric state and b_{UL} is the branching of the decay of the upper isomeric state to the lower isomeric state.

The isomeric ratios measured in the current work are summarized in table 5.9.

Table 5.9: *Isomeric ratios measured in the current experiment. In all cases the branching ratio is assumed to be 100%.*

Nucleus	E (keV)	J^π	τ	$R(\%)$
^{94}Pd	4884	(14^+)	530(10) ns	28±5
^{96}Pd	2531	8^+	1.82(5) μs	17±3
^{93}Ru	2083	$(21/2)^+$	4.3(4) μs	7±1
^{86}Tc	(1524)	(6^+)	1.59(20) μs	41±7
^{87}Tc	64+x	Unknown	862(47) ns	12±2
^{87}Tc	71+x	Unknown	981(82) ns	5±1
^{88}Tc	95+x	Unknown	211(18) ns	83±54
^{82}Nb	(1180)	(5^+)	133(30) ns	78±140

Chapter 6

Conclusions

The gamma-ray decay of isomeric states in neutron-deficient nuclei around the $N = Z$ line have been investigated as part of the RISING campaign at GSI. The relativistic fragmentation of 750 MeV per nucleon ^{107}Ag projectiles on a 4 g/cm^2 berylium target was used to populate the isomeric states and the FRS with its ancillary detectors was used to separate and unambiguously identify the nuclei of interest. An aluminium degrader was used to slow down the fragments so they could be implanted in a passive stopper made of plastic located at the centre of the RISING Stopped Array. The Ge detectors identified the gamma-ray decay of isomeric states and digital electronics were utilised to correlate the decays to the associated ion.

The experimental work reported in this thesis has allowed the identification of previously unobserved excited states in the self-conjugate odd-odd nuclei ^{82}Nb and ^{86}Tc. The low-lying structures of both systems are dominated by $T = 1$, np pairing effects which have already been observed in the other odd-odd $N = Z$ nuclei above $^{42}_{21}$Sc. The new data suggest that the $T = 1$, rather than $T = 0$, pairing interaction is the dominant feature throughout the fpg shell.

Previously unreported isomeric states have been identified in ^{87}Tc and ^{88}Tc with mean lifetimes of 933 (35) ns and 211 (18) ns respectively. A previously reported isomeric state in ^{84}Nb has been observed in the present data and another previously identified excited state in this nucleus has now been assigned as isomeric with a mean lifetime of 223 (35) ns. The spin of the isomeric state is most likely 7^+ on the basis of decay mutlipolarity arguments but this cannot be confirmed.

Appendix A

Calculation of Internal Conversion Coefficients

An intensity balance has been used to determine the internal conversion coefficients of the 124 and 81 keV transitions which decay directly from the isomeric states in ^{82}Nb and ^{86}Tc. The total internal conversion coefficient of a transition is defined as

$$\alpha_{TOT} = \frac{I_{e^-}}{I_\gamma} \tag{A.1}$$

where I_{e^-} is the number of decays by electron conversion and I_γ is the number of decays by gamma-ray emission. If all gamma-ray decays populating and de-populating an excited state are measured (and corrected for detection efficiency) then the difference between the de-populating intensity and the feeding transition (the 'missing' intensity) is due to internal conversion. It follows that the internal conversion coefficient is equal to

$$\alpha_{TOT} = \frac{(I_\gamma^D - I_\gamma^P)}{I_\gamma^P} \tag{A.2}$$

where I_γ^P and I_γ^D is the observed intensity of the populating and de-populating gamma-ray transitions respectively.

^{82}Nb

Table A.1 shows the intensities of the relevant gamma rays observed in ^{82}Nb. The internal conversion coefficient is calculated such that,

Table A.1: *Gamma-ray intensities observed in the decay of ^{82}Nb.*

E_γ (keV)	Counts	Efficiency (%)	α_{TOT}	Intensity
124	28(5)	37.3	-	75(13)
418	30(5)	21.5	0.00772	141(23)
638	16(4)	16.0	0.00224	100(25)

Table A.2: *Gamma-ray intensities observed in the decay of ^{86}Tc.*

E_γ (keV)	Counts	Efficiency (%)	α_{TOT}	Intensity
81	161(13)	40.5	-	398(32)
269	57(8)	28.1	0.0199	207(29)
850	210(14)	14.6	0.00122	1438(96)

$$0.33 = \frac{(100 - 75)}{75} \tag{A.3}$$

and the error is,

$$0.304 = \sqrt{\left(\frac{13}{75}\right)^2 + \left(\frac{25}{100}\right)^2} \tag{A.4}$$

Therefore the internal conversion coefficient of the 124 keV transition in ^{82}Nb is 0.33 (30).

^{86}Tc

The intensities of the relevant gamma rays observed in ^{86}Tc are shown in Table A.2. The internal conversion coefficient is calculated such that,

$$3.13 = \frac{(1438 + 207) - 398}{398} \tag{A.5}$$

and the error is,

$$0.17 = \sqrt{\left(\frac{32}{398}\right)^2 + \left(\frac{29}{207}\right)^2 + \left(\frac{96}{1438}\right)^2} \tag{A.6}$$

Therefore the internal conversion coefficient of the 81 keV transition in ^{86}Tc is 3.13 (17).

Appendix B

Publications

B.1 First Author Peer-Reviewed Publications

A.B. Garnsworthy, P.H. Regan, L. Cáceres *et al.*,
Neutron-Proton Pairing Competition in $N = Z$ Nuclei:
Metastable State Decays in the Proton Dripline Nuclei $^{82}_{41}$Nb and $^{86}_{43}$Tc
Submitted to Physics Letters B, (2007)

A.B. Garnsworthy, P.H. Regan, S. Pietri *et al.*,
Isomeric States in the Light Tc Isotopes,
Proceedings of the 2006 Zakopane Conference on Nuclear Physics,
Acta Physica Polonica B, Vol. 38, p.1265 (2006)

A.B. Garnsworthy, N.J. Thompson, Zs. Podolyák *et al.*,
Spectroscopy of ^{212}Po and ^{213}At using a ^{8}He Beam and EXOGAM,
Proceedings of NUSTAR 2005,
Journal of Physics G, Vol. 31, N10, S1851 (2005)

B.2 Other Publications in Peer-Reviewed Journals

P.H. Regan, A.B. Garnsworthy, S. Pietri *et al.* [+50 others],
Isomer Spectroscopy Using Relatavistic Projectile Fragmentation at the $N = Z$ Line for $A \sim 80 \rightarrow 90$,
Proceedings of NN2006, Rio de Janeiro, Aug 2006
Nuclear Physics A787, p491c-498c, (2007)

N.J. Thompson, P.H. Regan, A.B. Garnsworthy *et al.* [+15 others],
Spectroscopy of $^{91}Zr_{51}$ at Medium to High Spins,
Proceedings of the 2006 Zakopane Conference on Nuclear Physics,
Acta Physica Polonica B, Vol. 38, p.1381 (2006)

S. Pietri, P.H. Regan, Zs. Podolyák, D. Rudolph, S.J. Steer, A.B. Garnsworthy *et al.* [+57 others],
Recent Results in Fragmentation Isomer Spectroscopy With Rising,
Nuclear Instruments and Methods B, Vol. 261, p.1079-1083, (2007)

G.A. Jones, P.H. Regan, P.M. Walker ... A.B. Garnsworthy *et al.* [+15 others]
Identification of a High-Spin Isomer in ^{99}Mo,
Physical Review C, 76, 047303 (2007)

S. Pietri, P.H. Regan, Zs. Podolyák, A.B. Garnsworthy *et al.* [+57 others],
First Results from the Stopped Beam Isomer RISING Campaign at GSI,
Proceedings of the 2006 Zakopane Conference on Nuclear Physics,
Acta Physica Polonica B, Vol. 38, p.1255 (2006)

L.S. Cáceres, M. Gorska, A. Jungclaus, P.H. Regan, A.B. Garnsworthy *et al.* [+52 others],
Identification of Excited States in the $N = Z$ Nucleus, ^{82}Nb,
Proceedings of the 2006 Zakopane Conference on Nuclear Physics,
Acta Physica Polonica B, Vol. 38, p.1271 (2006)

S. Myalski, M. Kmiecik, A. Maj, P.H. Regan, A.B. Garnsworthy *et al.* [+48 others],
Isomeric Ratio for the $I^{\pi} = 8^{+}$ Yrast State in ^{96}Pd Produced in the Relativistic Fragmentation of ^{107}Ag,
Proceedings of the 2006 Zakopane Conference on Nuclear Physics,
Acta Physica Polonica B, Vol. 38, p.1277 (2006)

S.J. Steer, Zs. Podolyák, S. Pietri, A.B. Garnsworthy *et al.* [+46 others],
Identification of Isomeric States 'South' of ^{208}Pb via Projectile Fragmentation,
Proceedings of the 2006 Zakopane Conference on Nuclear Physics,
Acta Physica Polonica B, Vol. 38, p.1283 (2006)

V. Werner, N. Benczer-Koller, G. Kumbartzki ... A.B. Garnsworthy *et al.* [+29 others],
Evidence for Configurational Isospin Polarization of Mixed-Symmetry States from Magnetic Moment Measurements
Submitted to Physical Review Letters, (2007)

G.A. Jones, S.J. Williams, P.M. Walker ... A.B. Garnsworthy *et al.* [+16 others],
High-Spin, Multi-particle Isomers in ^{121,123}Sb,
Submitted to Physical Review C, (2007)

A. Wolf ... A.B. Garnsworthy *et al.* [+12 others],
g factor of the 2_1^+ state of ^{170}Hf,
Submitted to Physical Review C, (2007)

T.R. Saito, N. Saito, K. Starosta A.B. Garnsworthy *et al.* [+53 others],
Yrast and Non-Yrast 2^+ States of ^{134}Ce and ^{136}Nd Populated in Relatavistic Coulomb Excitation
Submitted to Physics Letters B, (2007)

B.3 Other Publications

P.H. Regan, A.B. Garnsworthy, S.J. Steer *et al.* [+50 others],
First Results from the Stopped RISING Campaign at GSI: The Mapping of Isomeric Decays in Highly Exotic Nuclei,
Sixth International Conference of the Balkan Physical Union, Istanbul, Aug 2006
AIP Conference Proceedings 899, p19-22, (2007)

P. Doornenbal, A. Brger, D. Rudolph ... A.B. Garnsworthy *et al.* [+71 others],
RISING: Gamma-ray Spectroscopy with Radioactive Beams at GSI,
Tours Symposium on Nuclear Physics VI, Tours, Sept 2006
AIP Conference Proceedings 891, p99-107, (2007)

G.A. Jones, P.M. Walker, Zs. Podolyák ... A.B. Garnsworthy *et al.* [+17 others],
Microsecond and nanosecond isomers populated in fission reactions,
Proceedings of Fusion 2006, Venezia, March 2006
AIP Conference Proceedings 853, p342-349, (2007)

P.H. Regan, N.J. Thompson, A.B. Garnsworthy *et al.* [+14 others],
Isomer and In-Beam Spectroscopy of ^{91,92}Zr,
AIP Conference Proceedings 819, p35-39, (2006)

Bibliography

[1] Yu.Ts. Oganessian, V.K. Utyonkov, Yu.V. Lobanov, F.Sh. Abdullin, A.N. Polyakov, R.N. Sagaidak, I.V. Shirokovsky, Yu.S. Tsyganov, A.A. Voinov, G.G. Gulbekian, S.L. Bogomolov, B.N. Gikal, A.N. Mezentsev, S. Iliev, V.G. Subbotin, A.M. Sukhov, K. Subotic, V.I. Zagrebaev, G.K. Vostokin, M.G. Itkis, K.J. Moody, J.B. Patin, D.A. Shaughnessy, M.A. Stoyer, N.J. Stoyer, P.A. Wilk, J.M. Kenneally, J.H. Landrum, J.F. Wild and R.W. Lougheed, *Physics Review C*, **74**, 044602 (2006).

[2] R. McPherson, R.A. Esterlund, A.M. Poskanzer and P.L. Reeder, *Physics Review*, **140**, B1513 (1965).

[3] B. Jurado, H. Savjols, W. Mittig, N.A. Orr, P. Roussel-Chomaz, D. Baiborodin, W.N. Catford, M. Chartier, C.E. Demonchy, Z. Dlouhy, A. Gillibert, L. Giot, A. Khouaja, A. Lepine-Szily, S. Lukyanov, J. Mrazek, Y.E. Penionzhkevich, S. Pita, M. Rousseau and A.C. Villari, *Physics Letters B*, **649**, 43 (2007).

[4] A.H. Wapstra, G. Audi and C. Thibault, *Nuclear Physics A*, **729**, 129 (2003).

[5] R.B. Firestone, LBNL Isotopes Project, Nuclear Structure Systematics Home Page http://ie.lbl.gov/systematics.html, (2006).

[6] P.J. Woods and C.N. Davids, *Ann. Rev. of Nucl. and Part. Sci.*, **47**, 541 (1997).

[7] W. Nazarewicz, J. Dudek, R. Bengtsson, T. Bengtsson and I. Ragnarsson, *Nuclear Physics A*, **435**, 397 (1985).

[8] D. Bucurescu, C. Rossi Alvarez, C.A. Ur, N. Mărginean, P. Spolaore, D. Bazzacco, S. Lunardi, D.R. Napoli, M. Ionescu-Bujor, A. Iordachescu, C.M. Petrache, G. de Angelis, A. Gadea, D. Foltescu, F. Brandolini, G. Falconi, E. Farnea,

S.M. Lenzi, N.H. Medina, Z. Podolyák, M. De Poli, M.N. Rao and R. Venturelli, *Physics Review C*, **56**, 2497 (1997).

[9] C.D. O'Leary, M.A. Bentley, D.E. Appelbe, R.A. Bark, D.M. Cullen, S. Erturk, A. Maj, J.A. Sheikh and D.D. Warner, *Physics Letters B*, **459**, 73 (1999).

[10] S.K. Patra, B.K. Raj, M.S. Mehta and R.K. Gupta, *Physics Review C*, **65**, 054323 (2002).

[11] A. Petrovici, K.W. Schmid and A. Faessler, *Nuclear Physics A*, **605**, 290 (1996).

[12] D.H. Wilkinson, *Nature*, **172**, 576 (1953).

[13] D.D. Warner, M.A. Bentley and P. Van Isacker, *Nature Physics*, **2**, 311 (2006).

[14] A. de Shalit and H. Freshbach, *Theoretical Nuclear Physics, Vol.1, Nuclear Structure*, John Wiley & Sons Inc., (1974).

[15] R. Casten, *Nuclear Structure from a Simple Perspective (2nd Edition)*, Oxford University Press, (2000).

[16] K.S. Krane, *Introductory Nuclear Physics*, John Wiley & Sons, (1988).

[17] J.M. Freeman, J.H. Montague, G. Murray, R.E. White and W.E. Burcham, *Nuclear Physics*, **69**, 433 (1965).

[18] R. Grzywacz, C.H. Yu, Z. Janas, S.D. Paul, J.C. Batchelder, C.R. Bingham, T.N. Ginter, C.J. Gross, J. McConnell, M. Lipoglavsek, A. Piechaczek, D.C. Radford, J.J. Ressler, K. Rykaczewski, J. Shergur, W.B. Walters, E.F. Zganjar, C. Baktash, M.P. Carpenter, R.V.F. Janssens, C.E. Svensson, J.C. Waddington, D. Ward and E. Dragulescu, *Nuclear Physics A*, **682**, 41c (2001).

[19] J.C. Hardy and D.E. Alburger, *Physics Letters B*, **42**, 341 (1972).

[20] D.G. Jenkins, N.S. Kelsall, C.J. Lister, D.P. Balamuth, M.P. Carpenter, T.A. Sienko, S.M. Fischer, R.M. Clark, P. Fallon, A. Gorgen, A.O. Macchiavelli, C.E. Svensson, R. Wadsworth, W. Reviol, D.G. Sarantites, G.C. Ball, J. Rikovska Stone, O. Juillet, P. Van Isacker, A.V. Afanasjev and S. Frauendorf, *Physics Review C*, **65**, 064307 (2002).

[21] J.W. Nelson, J.D. Oberholtzer and H.S. Plendl, *Nuclear Physics*, **62**, 434 (1965).

[22] C.D. O'Leary, M.A. Bentley, S.M. Lenzi, G. Martinez-Pinedo, D.D. Warner, A.M. Bruce, J.A. Cameron, M.P. Carpenter, C.N. Davids, P. Fallon, L. Frankland, W. Gelletly, R.V.F. Janssens, D.T. Joss, C.J. Lister, P.H. Regan, P. Reiter, B. Rubio, D. Seweryniak, C.E. Svensson, S.M. Vincent and S.J. Williams, *Physics Letters B*, **525**, 49 (2002).

[23] C.D. O'Leary, C.E. Svensson, S.G. Frauendorf, A.V. Afanasjev , D.E. Appelbe, R.A.E. Austin, G.C. Ball, J.A. Cameron, R.M. Clark, M. Cromaz, P. Fallon, D.F. Hodgson, N.S. Kelsall, A.O. Macchiavelli, I. Ragnarsson, D. Sarantites, J.C. Waddington and R. Wadsworth, *Physics Review C*, **67**, 021301R (2003).

[24] D. Rudolph, C.J. Gross, J.A. Sheikh, D.D. Warner, I.G. Bearden, R.A. Cunningham, D. Foltescu, W. Gelletly, F. Hannachi, A. Harder, T.D. Johnson, A. Jungclaus, M.K. Kabadiyski, D. Kast, K.P. Lieb, H.A. Roth, T. Shizuma, J. Simpson, O. Skeppstedt, B.J. Varley and M. Weiszflog, *Physics Review Letters*, **76**, 376 (1996).

[25] G.T.A. Squier, W.E. Burcham, J.M. Freeman, R.J. Petty, S.D. Hoath and J.S. Ryder, *Nuclear Physics A*, **242**, 62 (1975).

[26] J. Uusitalo, D. Seweryniak, P.F. Mantica, J. Rikovska, D.S. Brenner, M. Huhta, J. Greene, J.J. Ressler, B. Tomlin, C.N. Davids, C.J. Lister and W.B. Walters, *Physics Review C*, **57**, 2259 (1998).

[27] S.M. Vincent, P.H. Regan, D.D. Warner, R.A. Bark, D. Blumenthal, M.P. Carpenter, C.N. Davids, W. Gelletly, R.V.F. Janssens, C.D. O'Leary, C.J. Lister, J. Simpson, D. Seweryniak, T. Saitoh, J. Schwartz, S. Tormanen, O. Juillet, F. Nowacki and P. Van Isacker, *Physics Letters B*, **437**, 264 (1998).

[28] D. Wegener, *Z. Physik*, **198**, 251 (1967).

[29] C. Longour, J. Garces Narro, B. Blank, M. Lewitowicz, Ch. Miehe, P.H. Regan, D. Applebe, L. Axelsson, A.M. Bruce, W.N. Catford, C. Chandler, R.M. Clark, D.M. Cullen, S. Czajkowski, J.M. Daugas, Ph. Dessagne, A. Fleury, L. Frankland, W. Gelletly, J. Giovinazzo, B. Greenhalgh, R. Grzywacz, M. Harder, K.L. Jones,

N. Kelsall, T. Kszczot, R.D. Page, C.J. Pearson, A.T. Reed, O. Sorlin and R. Wadsworth, *Physics Review Letters*, **81**, 3337 (1998).

[30] P.M. Walker and G. Dracoulis, *Nature*, **399**, 35 (1999).

[31] J.B. Cumming and D.E. Alburger, *Physics Review C*, **31**, 1494 (1985).

[32] T.K. Alexander and J.S. Forster, *Advanced Nuclear Physics*, **10**, 197 (1978).

[33] M. Moszynski and H. Mach, *Nuclear Instruments and Methods A*, **277**, 407 (1989).

[34] B. Blank, S. Andriamonje, S. Czajkowski, F. Davi, R. Del Moral, J.P. Dufour, A. Fleury, A. Musquere, M.S. Pravikoff, R. Grzywacz, Z. Janas, M. Pfützner, A. Grewe, A. Heinz, A. Junghans, M. Lewitowicz, J.E. Sauvestre and C. Donzaud, *Physics Review Letters*, **74**, 4611 (1995).

[35] A. Stolz, T. Faestermann, J. Friese, P. Kienle, H.-J. Korner, M. Munch, R. Schneider, E. Wefers, K. Zeitelhack, K. Summerer, H. Geissel, J. Gerl, G. Munzenberg, C. Schlegel, R.S. Simon, H. Weick, M. Hellström, M.N. Mineva and P. Thirolf, *Physics Review C*, **65**, 064603 (2002).

[36] R. Pfaff, D.J. Morrissey, W. Benenson, M. Fauerbach, M. Hellström, C.F. Powell, B.M. Sherrill, M. Steiner and J.A. Winger, *Physics Review C*, **53**, 1753 (1996).

[37] Z. Janas, C. Chandler, B. Blank, P.H. Regan, A.M. Bruce, W.N. Catford, N. Curtis, S. Czajkowski, Ph. Dessagne, A. Fleury, W. Gelletly, J. Giovinazzo, R. Grzywacz, M. Lewitowicz, C. Longour, C. Marchand, C. Miehe, N.A. Orr, R.D. Page, C.J. Pearson, M.S. Pravikoff, A.T. Reed, M.G. Saint-Laurent, J.A. Sheikh, S.M. Vincent, R. Wadsworth, D.D. Warner and J.S. Winfield, *Physics Review Letters*, **82**, 295 (1999).

[38] P. Möller, J.R. Nix, W.D. Myers and W.J. Swiatecki, *Atomic and Nuclear Data Tables*, **59**, 185 (1995).

[39] C. Chandler, P.H. Regan, B. Blank, C.J. Pearson, A.M. Bruce, W.N. Catford, N. Curtis, S. Czajkowski, Ph. Dessagne, A. Fleury, W. Gelletly, J. Giovinazzo, R. Grzywacz, Z. Janas, M. Lewitowicz, C. Marchand, Ch. Miehe, N.A. Orr,

R.D. Page, M.S. Pravikoff, A.T. Reed, M.G. Saint-Laurent, S.M. Vincent, R. Wadsworth, D.D. Warner, J.S. Winfield and F. Xu, *Physics Review C*, **61**, 044309 (2000).

[40] W. Heisenberg, *Z. Physik*, **43**, 172 (1927).

[41] J. Lilley, *Nuclear Physics; Principles and Applications*, John Wiley & Sons, (2001).

[42] P. Ring and P. Schuck, *The Nuclear Many-Body Problem*, Springer-Verlag, New York, (1980).

[43] F.D. Becchetti and G.W. Greenlees, *Physics Review*, **182**, 1190 (1969).

[44] G. Maruhn, *Nuclear Models*, Springer-Verlag, (1996).

[45] I. Talmi, *Simple Models of Complex Nuclei*, Harwood Academic Publishers, Switzerland, (1993).

[46] O. Mayer, *Physics Review*, **78**, 16 (1950).

[47] B.A. Brown, Lecture Notes in Nuclear Structure Physics, Michigan State University, (unpublished), (2005).

[48] R.D. Woods and D.S. Saxon, *Physics Review*, **95**, 577 (1954).

[49] O. Haxel, J.H.D. Jensen and H.E. Suess, *Z. Physik*, **128**, 295 (1950).

[50] C.J. Gallagher and S.A. Moszkowski, *Physics Review*, **111**, 1282 (1958).

[51] P. Smith, Private Communication, (2007).

[52] I. Ragnarsson, and S.G. Nilsson, *Shapes and Shells in Nuclear Structure*, Cambridge University Press, (1995).

[53] J. Rainwater, *Physics Review*, **79**, 432 (1950).

[54] D.L. Hill and J.A. Wheeler, *Physics Review*, **89**, 1102 (1953).

[55] G. Jones, PhD Thesis, University of Surrey, (unpublished), (2006).

[56] S.G. Nilsson, *Dan. Mat. Fys. Medd.*, **29**, 3 (1955).

[57] B. Singh, *Nuclear Data Sheets*, **97**, 241 (2002).

[58] J. Bardeen, L.N. Cooper and J.R. Schrieffer, *Physics Review*, **108**, 1175 (1957).

[59] J.R. Schrieffer, *Theory of Superconductivity, 3rd Edition*, Perseus Books, U.S., (1999).

[60] R.A. Broglia, *Annals of Physics*, **80**, 60 (1973).

[61] B.R. Mottleson and J.G. Valatin, *Physics Review Letters*, **5**, 511 (1960).

[62] K. Hara and Y. Sun, *International Journal of Modern Physics E*, **4**, 637 (1995).

[63] Y. Sun, *European Physics Journal A: Hadrons and Nuclei*, **20**, 133 (2004).

[64] Y. Sun and J.A. Sheikh, *Physics Review C*, **64**, 031302R (2001).

[65] Y. Sun, Private Communication, (2007).

[66] M. Dufour and A.P. Zuker, *Physics Review C*, **54**, 1641 (1996).

[67] F.R. Xu, *Physics Letters B*, **435**, 257 (1998).

[68] W.D. Myers and W.J. Swiatecki, *Annals of Physics*, **55**, 395 (1969).

[69] V.M. Strutinski, *Nuclear Physics A*, **95**, 420 (1967).

[70] W. Nazarewicz, M.A. Riley and J.D. Garret, *Nuclear Physics A*, **512**, 61 (1990).

[71] S. Bjørnholm and J. Lynn, *Reviews of Modern Physics*, **52**, 725 (1980).

[72] A.K. Kerman, *Annals of Physics*, **12**, 300 (1961).

[73] J.J. Ressler, R.F. Casten, N.V. Zamfir, C.W. Beausang, R.B. Cakirli, H. Ai, H. Amro, M.A. Caprio, A.A. Hecht, A. Heinz, S.D. Langdown, E.A. McCutchan, D.A. Meyer, C. Plettner, P.H. Regan, M.J.S. Sciacchitano and A.D. Yamamoto, *Physics Review C*, **69**, 034317 (2004).

[74] R. Vandenbosch, *Annual Review of Nuclear Science*, **27**, 1 (1977).

[75] G.D. Dracoulis, *Nuclear Physics A*, **752**, 213 (2005).

[76] P.M. Walker and G. Dracoulis, *Hyperfine Interactions*, **135**, 83 (2001).

[77] C.J. Lister, P.J. Ennis, A.A. Chishti, B.J. Varley, W. Gelletly, H.G. Price and A.N. James, *Physics Review C*, **42**, R1191 (1990).

[78] N. Mărginean, *European Physics Journal A: Hadrons and Nuclei*, **20**, 123 (2004).

[79] R. Wadsworth and P.J. Nolan, *Reports on Progress in Physics*, **65**, 1079 (2002).

[80] M. Belleguic, M.J. Lopez-Jimenez, M. Stanoiu, F. Azaiez, M.-G. Saint-Laurent, O. Sorlin, N.L. Achouri, J.-C. Angelique, C. Bourgeois, C. Borcea, J.-M. Daugas, C. Donzaud, F. De Oliveira-Santos, J. Duprat, S. Grevy, D. Guillemaud-Mueller, S. Leenhardt, M. Lewitowicz, Yu.-E. Penionzhkevich and Yu. Sobolev, *Nuclear Physics A*, **682**, 136 (2001).

[81] T. Enqvist, J. Benlliure, F. Farget, K.-H. Schmidt, P. Armbruster, M. Bernas, L. Tassan-Got, A. Boudard, R. Legrain, C. Volant, C. Bockstiegel, M. de Jong and J.P. Dufour, *Nuclear Physics A*, **658**, 47 (1999).

[82] T.J. Symons, Y.P. Viyogi, G.D. Westfall, P. Doll, D.E. Greiner, H. Faraggi, P.J. Lindstrom, D.K. Scott, H.J. Crawford and C. McParland, *Physics Review Letters*, **42**, 40 (1979).

[83] Y.P. Viyogi, T.J.M. Symons, P. Doll, D.E. Greiner, H.H. Heckman, D.L. Hendrie, P.J. Lindstrom, J. Mahoney, D.K. Scott, K. Van Bibber, G.D. Westfall, H. Wieman, H.J. Crawford, C. McParland and C.K. Gelbke, *Physics Review Letters*, **42**, 33 (1979).

[84] R. Broda, *European Physics Journal A: Hadrons and Nuclei*, **13**, 1 (2002).

[85] R. Broda, *Journal of Physics G*, **32**, R151 (2006).

[86] L.G. Moretto, *Reports on Progress in Physics*, **44**, 533 (1981).

[87] T. Bengtsson and I. Ragnarsson, *Nuclear Physics A*, **436**, 14 (1985).

[88] C. Plettner, H. Schnare, R. Schwengner, L. Kaubler, F. Donau, I. Ragnarsson, A.V. Afanasjev, A. Algora, G. de Angelis, A. Gadea, D.R. Napoli, J. Eberth, T. Steinhardt, O. Thelen, M. Hausmann, A. Muller, A. Jungclaus, K.P. Lieb, D.G. Jenkins, R. Wadsworth, A.N. Wilson and S. Frauendorf, *Physics Review C*, **62**, 014313 (2000).

[89] D. Cline, *Annual Review of Nuclear and Particle Science*, **36**, 683 (1986).

[90] W.N. Catford, R.C. Lemmon, C.N. Timis, M. Labiche, L. Caballero and R. Chapman, *AIP Conference Proceedings*, **704**, 185 (2003).

[91] M. Labiche, C.N. Timis, R.C. Lemmon, W.N. Catford, R. Chapman, N. Amzal, N.I. Ashwood, T.D. Baldwin, M. Burns, L. Caballero, M. Chartier, N. Curtis, G. de France, W. Gelletly, X. Liang, M. Freer, N.A. Orr, S.D. Pain, V.P.E. Pucknell, M. Rejmund, B. Rubio, H. Savajols, O. Sorlin, K. Spohr, Ch. Theisen and D.D. Warner, *Journal of Physics G*, **31**, S1691 (2005).

[92] M. Hencheck, R.N. Boyd, M. Hellström, D.J. Morrissey, M.J. Balbes, F.R. Chloupek, M. Fauerbach, C.A. Mitchell, R. Pfaff, C.F. Powell, G. Raimann, B.M. Sherrill, M. Steiner, J. Vandegriff and S.J. Yennello, *Physics Review C*, **50**, 2219 (1994).

[93] D.J. Morrissey, and the A1200 Group, *Nuclear Physics A*, **588**, c203 (1995).

[94] H. Geissel, G. Munzenberg and K. Riisager, *Annual Review of Nuclear and Particle Science*, **45**, 163 (1995).

[95] W.R. Phillips, *Reports on Progress in Physics*, **40**, 345 (1977).

[96] M. La Commara, K. Schmidt, H. Grawe, J. Döring, R. Borcea, S. Galanopoulos, M. Górska, S. Harissopulos, M. Hellström, Z. Janas, R. Kirchner, C. Mazzocchi, A.N. Ostrowski, C. Plettner, G. Rainovski and E. Roeckl, *Nuclear Physics A*, **708**, 167 (2002).

[97] I. Mukha, L. Batist, E. Roeckl, H. Grawe, J. Döring, A. Blazhev, C.R. Hoffman, Z. Janas, R. Kirchner, M. La Commara, S. Dean, C. Mazzocchi, C. Plettner, S.L. Tabor and M. Wiedeking, *Physics Review C*, **70**, 044311 (2004).

[98] I. Mukha, E. Roeckl, J. Döring, L. Batist, A. Blazhev, H. Grawe, C.R. Hoffman, M. Huyse, Z. Janas, R. Kirchner, M. La Commara, C. Mazzocchi, C. Plettner, S.L. Tabor, P. Van Duppen and M. Wiedeking, *Physics Review Letters*, **95**, 022501 (2005).

[99] C.N. Davids, B.B. Back, K. Bindra, D.J. Henderson, W. Kutschera, T. Lauritsen, Y. Nagame, P. Sugathan, A.V. Ramayya and W.B. Walters, *Nuclear Instruments and Methods B*, **70**, 358 (1992).

[100] D.G. Sarantites, P.-F. Hua, M. Devlin, L.G. Sobotka, J. Elson, J.T. Hood, D.R. LaFosse, J.E. Sarantites and M.R. Maier, *Nuclear Instruments and Methods A*, **381**, 418 (1996).

[101] U.C. Bergmann, H. O.U. Fynbo and O. Tengblad, *Nuclear Instruments and Methods A*, **515**, 657 (2003).

[102] D.G. Sarantites, W. Reviol, C.J. Chiara, R.J. Charity, L.G. Sobotka, M. Devlin, M. Furlotti, O.L. Pechenaya, J. Elson, P. Hausladen, S. Fischer, D. Balamuth and R.M. Clark, *Nuclear Instruments and Methods A*, **530**, 473 (2004).

[103] J. Hüfner, K.Schafer and B.Schurmann, *Physics Review C*, **12**, 1888 (1975).

[104] M. De Jong, A.V. Ignatyuk and K.-H. Schmidt, *Nuclear Physics A*, **613**, 435 (1997).

[105] K. Sümmerer and B. Blank, *Physics Review C*, **61**, 034607 (2000).

[106] D. Bazin, O. Tarasov, M. Lewitowicz and O. Sorlin, *Nuclear Instruments and Methods A*, **482**, 307 (2002).

[107] O.B. Tarasov and D. Bazin, *Nuclear Physics A*, **746**, 411 (2004).

[108] M. Górska, A. Banu, P. Bednarczyk, A. Bracco, A. Buerger, F. Camera, E. Caurier, P. Doornenbal, J. Gerl, H. Grawe, M. Honma, H. Huebel, A. Jungclaus, A. Maj, G. Neyens, F. Nowacki, T. Otsuka, M. Pfuetzner, S. Pietri, Zs. Podolyák, A. Poves, P.H. Regan, P. Reiter, D. Rudolph and H.J. Wollersheim, *Acta Physica Polonica B*, **38**, 1219 (2007).

[109] H. Geissel, P. Armbruster, K.H. Behr, A. Brunle, K. Burkard, M. Chen, H. Folger, B. Franczak, H. Keller, O. Klepper, B. Langenbeck, F. Nickel, E. Pfeng, M. Pfützner, E. Roeckl, K. Rykaczewski, I. Schall, D. Schardt, C. Scheidenberger, K.-H. Schmidt, A. Schroter, T. Schwab, K. Summerer, M. Weber, G. Munzenberg, T. Brohm, H.-G. Clerc, M. Fauerbach, J.-J. Gaimard, A. Grewe, E. Hanelt,

B. Knodler, M. Steiner, B. Voss, J. Weckenmann, C. Ziegler, A. Magel, H. Wollnik, J.P. Dufour, Y. Fujita, D.J. Vieira and B. Sherrill, *Nuclear Instruments and Methods B*, **70**, 286 (1992).

[110] A. Banu, J. Gerl, C. Fahlander, M. Górska, H. Grawe, T.R. Saito, H.-J. Wollersheim, E. Caurier, T. Engeland, A. Gniady, M. Hjorth-Jensen, F. Nowacki, T. Beck, F. Becker, P. Bednarczyk, M.A. Bentley, A. Burger, F. Cristancho, G. de Angelis, Zs. Dombradi, P. Doornenbal, H. Geissel, J. Grebosz, G. Hammond, M. Hellström, J. Jolie, I. Kojouharov, N. Kurz, R. Lozeva, S. Mandal, N. Mărginean, S. Muralithar, J. Nyberg, J. Pochodzalla, W. Prokopowicz, P. Reiter, D. Rudolph, C. Rusu, N. Saito, H. Schaffner, D. Sohler, H. Weick, C. Wheldon and M. Winkler, *Physics Review C*, **72**, 061305R (2005).

[111] A. Bürger and the RISING Collaboration, *Physics Letters B*, **622**, 29 (2005).

[112] H.J. Wollersheim, D.E. Appelbe, A. Banu, R. Bassini, T. Beck, F. Becker, P. Bednarczyk, K.-H. Behr, M.A. Bentley, G. Benzoni, C. Boiano, U. Bonnes, A. Bracco, S. Brambilla, A. Brunle, A. Burger, K. Burkard, P.A. Butler, F. Camera, D. Curien, J. Devin, P. Doornenbal, C. Fahlander, K. Fayz, H. Geissel, J. Gerl, M. Górska, H. Grawe, J. Grebosz, R. Griffiths, G. Hammond, M. Hellström, J. Hoffmann, H. Hubel, J. Jolie, J.V. Kalben, M. Kmiecik, I. Kojouharov, R. Kulessa, N. Kurz, I. Lazarus, J. Li, J. Leske, R. Lozeva, A. Maj, S. Mandal, W. Meczynski, B. Million, G. Munzenberg, S. Muralithar, M. Mutterer, P.J. Nolan, G. Neyens, J. Nyberg, W. Prokopowicz, V.F.E. Pucknell, P. Reiter, D. Rudolph, N. Saito, T.R. Saito, D. Seddon, H. Schaffner, J. Simpson, K.-H. Speidel, J. Styczen, K. Summerer, N. Warr, H. Weick, C. Wheldon, O. Wieland, M. Winkler and M. Zieblinski, *Nuclear Instruments and Methods A*, **537**, 637 (2005).

[113] G. Neyens, L. Atanasova, D.L. Balabanski, F. Becker, P. Bednarczyk, L. Cáceres, P. Doornenbal, J. Gerl, M. Górska, J. Grebosz, M. Hass, G. Ilie, N. Kurz, I. Kojouharov, R. Lozeva, A. Maj, M. Pfuetzner, S. Pietri, Zs. Podolyák, W. Prokopowicz, T.R. Saitoh, H. Schaffner, G. Simpson, N. Vermeulen, E. Werner-Malento, J. Walker, H.J. Wollersheim, D. Bazzacco, G. Benzoni, A. Blazhev, N. Blasi, A. Bracco, C. Brandau, F. Camera, S.K. Chamoli, S. Chmel, F.C.L. Crespi, J.M. Daugas, M. De Rydt, P. Detistov, C. Fahlander, E. Farnea, G. Georgiev,

K. Gladnishki, R. Hoischen, M. Ionescu-Bujor, A. Iordachescu, J. Jolie, A. Jungclaus, M. Kmiecik, A. Krasznahorkay, R. Kulessa, S. Lakshmi, G. Lo Bianco, S. Mallion, K. Mazurek, W. Meczynski, D. Montanari, S. Myalsky, O. Perru, D. Rudolph, G. Rusev, A. Saltarelli, R. Schwengner, J. Styczen, K. Turzo, J.J. Valiente-Dobon, O. Wieland and M. Zieblinski, *Annals of Physics*, **38**, 1237 (2007).

[114] S. Pietri, P.H. Regan, Zs. Podolyák, D. Rudolph, S. Steer, A.B. Garnsworthy, E. Werner-Malento, R. Hoischen, M. Górska, J. Gerl, H.-J. Wollersheim, I. Kojouharov, H. Schaffner, F. Becker, P. Bednarczyk, L. Cáceres, P. Doornenbal, H. Geissel, J. Grebosz, A. Kelic, N. Kurz, F. Montes, W. Prokopowicz, T. Saito, S. Tashenov, A. Heinz, M. Pfützner, T. Kurtukian-Nieto, G. Benzoni, M. Hellström, A. Jungclaus, J. Simpson, L.-L. Andersson, L. Atanasova, D. Balabanski, M.A. Bentley, B. Blank, A. Blazhev, C. Brandau, J.R. Brown, A.M. Bruce, F. Camera, W.N. Catford, I.J. Cullen, Zs. Dombradi, E. Estevez, C. Fahlander, W. Gelletly, G. Ilie, E.K. Johansson, J. Jolie, G.A. Jones, M. Kmiecik, F.G. Kondev, S. Lalkovski, Z. Liu, A. Maj, S. Myalski, T. Shizuma, A.J. Simons, S. Schwertel, P.M. Walker and O. Wieland, *Nuclear Instruments and Methods B*, **261**, 1079 (2007).

[115] S. Pietri, P.H. Regan, Zs. Podolyák, D. Rudolph, M. Górska, A. Jungclaus, M. Pfuetzner, A.B. Garnsworthy, S.J. Steer, L. Cáceres, E. Werner-Malento, R. Hoischen, J. Gerl, I. Kojouharov, H. Schaffner, H.J. Wollersheim, F. Becker, P. Bednarczyk, P. Doornenbal, H. Geissel, J. Grebosz, A. Kelic, N. Kurz, F. Montes, W. Prokopowicz, T. Saito, S. Tashenov, A. Heinz, T. Kurtukian-Nieto, G. Benzoni, M. Hellstroem, L.-L. Andersson, L. Atanasova, D.L. Balabanski, M.A. Bentley, B. Blank, A. Blazhev, C. Brandau, J.R. Brown, A.M. Bruce, F. Camera, W.N. Catford, I.J. Cullen, Zs. Dombradi, E. Estevez, C. Fahlander, W. Gelletly, G. Ilie, E.K. Johansson, J. Jolie, G.A. Jones, M. Kmiecik, F.G. Kondev, S. Lalkovski, Z. Liu, A. Maj, S. Myalski, T. Shizuma, A.J. Simons, S. Schwertel, P.M. Walker and O. Wieland, *Acta Physica Polonica B*, **38**, 1255 (2007).

[116] B. Voss, T. Brohm, H.-G. Clerc, A. Grewe, E. Hanelt, A. Heinz, M. de Jong, A. Junghans, W. Morawek, C. Rohl, S. Steinhauser, C. Ziegler, K.-H. Schmidt, K.-

H. Behr, H. Geissel, G. Munzenberg, F. Nickel, C. Scheidenberger, K. Summerer, A. Magel and M. Pfützner, *Nuclear Instruments and Methods A*, **364**, 150 (1995).

[117] M. Pfützner, H. Geissel, G. Munzenberg, F. Nickel, Ch. Scheidenberger, K.-H. Schmidt, K. Summerer, T. Brohm, B. Voss and H. Bichsel, *Nuclear Instruments and Methods B*, **86**, 213 (1994).

[118] H. Stelzer, *Nuclear Instruments and Methods A*, **310**, 103 (1991).

[119] D. Henzlová, PhD Thesis, Czech Technical University Prague, (unpublished), (2006).

[120] H. Bethe, *Annalen der Physik*, **397**, 325 (1930).

[121] G.F. Knoll, *Radiation Detection and Measurement, Third Edition*, John Wiley & Sons, (2000).

[122] K. Debertin and R.G. Helmer, *Gamma and X-ray Spectroscopy with Semiconductor Detectors*, North-Holland, Amsterdam, (1988).

[123] M. Wilhelm et al., *Nuclear Instruments and Methods A*, **381**, 462 (1996).

[124] P. Nolan, F.A. Beck, and D.B. Fossan, *Annual Review of Nuclear and Particle Science*, **44**, 561 (1994).

[125] A.B. Garnsworthy, P.H. Regan, S. Pietri, D. Rudolph, L. Cáceres, M. Górska, Zs. Podolyák, S.J. Steer, A. Heinz, F. Becker, P. Bednarczyk, P. Doornenbal, H. Geissel, J. Gerl, H. Grawe, J. Grebosz, A. Kelic, I. Kojouharov, N. Kurz, F. Montes, W. Prokopwicz, T. Saito, H. Schaffner, S. Tachenov, E. Werner-Malento, H.J. Wollersheim, G. Benzoni, B. Blank, C. Brandau, A.M. Bruc, F. Camera, W.N. Catford, I.J. Cullen, Zs. Dombradi, E. Estevez, W. Gelletly, R. Hoischen, G. Ilie, J. Jolie, G.A. Jones, A. Jungclaus, M. Kmiecik, F.G. Kondev, T. Kurtukian-Nieto, S. Lalkovski, Z. Liu, A. Maj, S. Myalski, M. Pfuetzner, T. Shizuma, A.J. Simons, S. Schwertel, P.M. Walker and O. Wieland, *Acta Physica Polonica B*, **38**, 1265 (2007).

[126] P.H. Regan, A.B. Garnsworthy, S. Pietri, L. Cáceres, M. Górska, D. Rudolph, Zs. Podolyák, S.J. Steer, R. Hoischen, J. Gerl, H.J. Wollersheim, J. Grebosz, H.

Schaffner, W. Prokopwicz, I. Kojouharov, F. Becker, P. Bednarczyk, P. Doornenball, H. Geissel, H. Grawe, A. Kelic, N. Kurz, F. Montes, T. Saito, S. Tashenov, E. Werner-Malento, g, A. Heinz, L. Atanasova, D. Balabanski, G. Benzoni, B. Blank, A. Blazhev, C. Brandau, A.M. Bruce, W.N. Catford, F. Camera, I.J. Cullen, M.E. Estevez, C. Fahlander, W. Gelletly, G. Ilie, A. Jungclaus, J. Jolie, T. Kurtukian-Nieto, Z. Liu, M. Kmiecik, A. Maj, S. Myalski, S. Schwertel, T. Shizuma, A.J. Simonsa, P.M. Walker and O. Wieland, *Nuclear Physics A*, **787**, 491c (2007).

[127] C. Scheidenberger, Th. Stöhlker, W.E. Meyerhof, H. Geissel, P.H. Mokler and B. Blank, *Nuclear Instruments and Methods B*, **142**, 441 (1998).

[128] H. Grawe and H. Haas, *Physics Letters B*, **120**, 63 (1983).

[129] B.A. Brown, O. Häusser, T. Faestermann, D. Ward, H.R. Andrews and D. Horn, *Nuclear Physics A*, **306**, 242 (1978).

[130] H. Grawe, H.H. Bertschat and H. Haas, *Hyperfine Interactions*, **15/16**, 65 (1983).

[131] P. Komninos, E. Nolte and P. Blasi, *Z. Physik*, **310**, 137 (1983).

[132] M. La Commara, K. Schmidt, H. Grawe, J. Döring, R. Borcea, S. Galanopoulos, M. Górska, S. Harissopulos, M. Hellström, Z. Janas, R. Kirchner, C. Mazzocchi, A.N. Ostrowski, C. Plettner, G. Rainovski and E. Roeckl, *Nuclear Physics A*, **708**, 167 (2002).

[133] C.M. Baglin, *Nuclear Data Sheets*, **80**, 1 (1997).

[134] D. Rudolph, Private Communication, (2006).

[135] A.B. Garnsworthy, P.H. Regan, S. Pietri, Y. Sun, F.R. Xu, D. Rudolph, M. Górska, L. Cáceres, Zs. Podolyák, S.J. Steer, A. Heinz, F. Becker, P. Bednarczyk, P. Doornenbal, H. Geissel, J. Gerl, H. Grawe, J. Grebosz, A. Kelic, I. Kojouharov, N. Kurz, F. Montes, W. Prokopwicz, T. Saito, H. Schaffner, S. Tachenov, E. Werner-Malento, H.J. Wollersheim, G. Benzoni, B. Blank, C. Brandau, A.M. Bruc, F. Camera, W.N. Catford, I.J. Cullen, Zs. Dombradi, E. Estevez, W. Gelletly, R. Hoischen, G. Ilie, J. Jolie, G.A. Jones, A. Jungclaus, M. Kmiecik, F.G. Kondev, T. Kurtukian-Nieto, S. Lalkovski, Z. Liu, A. Maj, S. Myalski, M.

Pfuetzner, T. Shizuma, A.J. Simons, S. Schwertel, P.M. Walker and O. Wieland, *Submitted to Phys. Rev. Letts.* (2007).

[136] L.S. Cáceres, M. Górska, A. Jungclaus, P.H. Regan, A.B. Garnsworthy, S. Pietri, Zs. Podolyák, D. Rudolph, S.J. Steer, H. Grawe, D.L. Balabanski, F. Becker, P. Bednarczyk, G. Benzoni, B. Blank, C. Brandau, A.M. Bruce, F. Camera, W.N. Catford, I.J. Cullen, Zs. Dombradi, P. Doornenbal, E. Estevez, H. Geissel, W. Gelletly, J. Gerl, J. Grebosz, A. Heinz, R. Hoischen, G. Ilie, J. Jolie, G.A. Jones, M. Kmiecik, I. Kojouharov, F.G. Kondev, T. Kurtukian-Nieto, N. Kurz, S. Lalkowski, L. Liu, A. Maj, S. Myalski, F. Montes, M. Pfüetzner, W. Prokopowicz, T. Saito, H. Schaffner, S. Schwertel, T. Shizuma, A.J. Simons, S. Tashenov, P.M. Walker, E. Werner-Malento, O. Wieland and H.J. Wollersheim, *Acta Physica Polonica B*, **38**, 1271 (2007).

[137] S. Myalski, M. Kmiecik, A. Maj, P.H. Regan, A.B. Garnsworthy, S. Pietri, D. Rudolph, Zs. Podolyák, S.J. Steer, F. Becker, P. Bednarczyk, J. Gerl, M. Górska, H. Grawe, I. Kojouharov, H. Schaffner, H.J. Wollersheim, W. Prokopowicz, J. Grebosz, G. Benzoni, B. Blank, C. Brandau, A.M. Bruce, L. Cáceres, F. Camera, W.N. Catford, I.J. Cullen, Zs. Dombradi, P. Doornenbal, E. Estevez, H. Geissel, W. Gelletly, A. Heinz, R. Hoischen, G. Ilie, G.A. Jones, A. Jungclaus, A. Kelic, F.G. Kondev, T. Kurtukian-Nieto, N. Kurz, S. Lalkovski, Z. Liu, F. Montes, M. Pfuetzner, T. Saito, T. Shizuma, A.J. Simons, S. Schwertel, S. Tachenov, P.M. Walker, E. Werner-Malento and O. Wieland, *Acta Physica Polonica B*, **38**, 1277 (2007).

[138] P.H. Regan, A. B. Garnsworthy, S. J. Steer, S. Pietri, Zs. Podolyák, D. Rudolph, M. Górska, L. Cáceres, E. Werner-Malento, J. Gerl, H.J. Wollersheim, F. Becker, P. Bednarczyk, P.D. Doornenbal, H. Geissel, H. Grawe, J. Grebosz, R. Hoischen, A. Kelic, I. Kojouharov, N. Kurz, F. Montes, W. Prokopowicz, T. Saito, H. Schaffner, S. Tashenov, A. Heinz, M. Pfützner, T. Kurtukian-Nieto, G. Benzoni, M. Hellström, A. Jungclaus, L.-L. Andersson, L. Atanasova, D.L. Balabanski, M.A. Bentley, B. Blank, A. Blazhev, C. Brandau, J. Brown, A.M. Bruce, F. Camera, W.N. Catford, I.J. Cullen, Zs. Dombradi, E. Estevez, C. Fahlander, W. Gelletly, G. Ilie, E.K. Johansson, J. Jolie, G. A. Jones, M. Kmiecik, F.G. Kondev,

S. Lalkovski, Z. Liu, A. Maj, S. Myalski, S. Schwertel, T. Shizuma, A.J. Simons, P.M. Walker, and O. Wieland, *AIP Conference Proceedings*, **899**, 19 (2007).

[139] D. Rudolph, C. Baktash, C.J. Gross, W. Satula, R. Wyss, I. Birriel, M. Devlin, H.-Q. Jin, D.R. LaFosse, F. Lerma, J.X. Saladin, D.G. Sarantites, G.N. Sylvan, S.L. Tabor, D.F. Winchell, V.Q. Wood and C.H. Yu, *Physics Review C*, **56**, 98 (1997).

[140] M. Pfützner, P.H. Regan, P.M. Walker, M. Caamano, J. Gerl, M. Hellström, P. Mayet, K.-H. Schmidt, Zs. Podolyák, M.N. Mineva, A. Aprahamian, J. Benlliure, A.M. Bruce, P.A. Butler, D. Cortina Gil, D.M. Cullen, J. Döring, T. Enqvist, C. Fox, J. Garces Narro, H. Geissel, W. Gelletly, J. Giovinazzo, M. Górska, H. Grawe, R. Grzywacz, A. Kleinbohl, W. Korten, M. Lewitowicz, R. Lucas, H. Mach, C.D. O'Leary, F. De Oliveira, C.J. Pearson, F. Rejmund, M. Rejmund, M. Sawicka, H. Schaffner, Ch. Schlegel, K. Schmidt, Ch. Theisen, F. Vives, D.D. Warner, C. Wheldon, H.J. Wollersheim and S. Wooding, *Physics Review C*, **65**, 064604 (2002).

[141] H. Grawe, Private Communication, (2006).

[142] F. Rosel, H.M. Friess, K. Alder and H.C. Pauli, *Atomic and Nuclear Data Tables*, **21**, 291 (1978).

[143] S.D. Paul, H.C. Jain and J.A. Sheikh, *Physics Review C*, **55**, 1563 (1997).

[144] C.J. Gross, W. Gelletly, M.A. Bentley, H.G. Price, J. Simpson, B.J. Varley, J.L. Durell, O. Skeppstedt and S. Rastikerdar, *Physics Review C*, **43**, R5 (1991).

[145] S.M. Fischer *et al.*, *in press in Phys. Rev. C* (2007).

[146] C.J. Gross, K.P. Lieb, D. Rudolph, M.A. Bentley, W. Gelletly, H.G. Price, J. Simpson, D.J. Blumenthal, P.J. Ennis, C.J. Lister, Ch. Winter, J.L. Durell, B.J. Varley, O. Skeppstedt and S. Rastikerdar, *Nuclear Physics A*, **535**, 203 (1991).

[147] N. Mărginean, D. Bucurescu, C.A. Ur, D. Bazzacco, S.M. Lenzi, S. Lunardi, C. Rossi Alvarez, M. Ionescu-Bujor, A. Iordachescu, G. de Angelis, M. De Poli, E. Farnea, A. Gadea, D.R. Napoli, P. Spolaore and A. Buscemi, *European Physics Journal A: Hadrons and Nuclei*, **4**, 311 (1999).

[148] P.H. Regan, C. Chandler, C.J. Pearson, B. Blank, R. Grzywacz, M. Lewitowicz, A.M. Bruce, W.N. Catford, N. Curtis, S. Czajkowski, P. Dessagne, A. Fleury, W. Gelletly, J. Giovinazzo, Z. Janas, C. Longour, C. Marchand, C. Miehe, N.A. Orr, R.D. Page, M.S. Pravikoff, A.T. Reed, M.G. Saint-Laurent, S.M. Vincent, R. Wadsworth, D.D. Warner and J.S. Winfield, *Acta Physica Polonica B*, **79**, 432 (1997).

[149] D. Rudolph, C.J. Gross, Y.A. Akovali, C. Baktash, J. Döring, F.E. Durham, P.-F. Hua, G.D. Johns, M. Korolija, D.R. LaFosse, I.Y. Lee, A.O. Macchiavelli, W. Rathbun, D.G. Sarantites, D.W. Stracener, S.L. Tabor, A.V. Afanasjev and I. Ragnarsson, *Physics Review C*, **54**, 117 (1996).

[150] S.M. Fischer, C.J. Lister, M.P. Carpenter, N.J. Hammond, R.V.F. Janssens, E.F. Moore, G. Mukherjee, D. Seweryniak, S. Sinha, S.J. Freeman, J. Carney, D.P. Balamuth and Y. Sun, *Physics Review C*, **75**, 064310 (2007).

[151] D. Rudolph, F. Cristancho, C.J. Gross, A. Jungclaus, K.P. Lieb, M.A. Bentley, W. Gelletly, J. Simpson, H. Grawe, J. Heese, K.-H. Maier, J. Eberth, S. Skoda, J.L. Durell, B.J. Varley, D.J. Blumenthal, C.J. Lister and S. Rastikerdar, *Journal of Physics G*, **17**, L113 (1991).

[152] P.M. Endt, *Atomic and Nuclear Data Tables*, **23**, 547 (1979).

[153] A. Odahara, Y. Gono, S. Mitarai, T. Shizuma, E. Ideguchi, J. Mukai, H. Tomura, B.J. Min, S. Suematsu, T. Kuroyanagi, K. Heiguchi, T. Komatsubara and K. Furuno, *Z. Physik*, **354**, 231 (2004).

[154] S. Hofmann, A. Willmeroth and R. Vianden, *Z. Physik*, **A325**, 37 (1986).

[155] S. Raman, C.W. Nestor Jr. and P. Tikkanen, *Atomic and Nuclear Data Tables*, **78**, 1 (2001).

[156] B.S. Nara Singh, A.N. Steer, D.G. Jenkins, R. Wadsworth, M.A. Bentley, P.J. Davies, R. Glover, N.S. Pattabiraman, C.J. Lister, T. Grahn, P.T. Greenlees, P. Jones, R. Julin, S. Juutinen, M. Leino, M. Nyman, J. Pakarinen, P. Rahkila, J. Saren, C. Scholey, J. Sorri, J. Uusitalo, P.A. Butler, M. Dimmock, D.T. Joss, J. Thomson, B. Cederwall, B. Hadinia, M. Sandzelius, *Physics Review C*, **75**, 061301 (2007).

[157] T. Faestermann *et al.*, *European Physics Journal A: Hadrons and Nuclei*, **15**, 185 (2002).

[158] S. Dean, M. Górska, F. Aksouh, H. de Witte, M. Facina, M. Huyse, O. Ivanov, K. Krouglov, Yu. Kudryavtsev, I. Mukha, D. Smirnov, J.-C. Thomas, K. Van de Vel, J. Van de Walle, P. Van Duppen and J. Van Roosbroeck, *European Physics Journal A: Hadrons and Nuclei*, **21**, 243 (2004).

[159] C.M. Baglin, *Nuclear Data Sheets*, **91**, 423 (2003).

[160] D. Abriola and A.A. Sonzogni, *Nuclear Data Sheets*, **107**, 2423 (2006).

[161] G. Mukherjee and A.A. Sonzogni, *Nuclear Data Sheets*, **105**, 419 (2005).

[162] E. Browne, *Nuclear Data Sheets*, **82**, 379 (1997).

[163] B. Singh, *Nuclear Data Sheets*, **94**, 1 (2001).

[164] B. Singh, *Nuclear Data Sheets*, **105**, 223 (2005).

[165] J. K. Tuli, *Nuclear Data Sheets*, **98**, 209 (2003).

[166] K.A. Gladnishki, Zs. Podolyák, P.H. Regan, J. Gerl, M. Hellström, Y. Kopatch, S. Mandal, M. Górska, R.D. Page, H.-J. Wollersheim, A. Banu, G. Benzoni, H. Boardman, M. La Commara, J. Ekman, C. Fahlander, H. Geissel, H. Grawe, E. Kaza, A. Korgul, M. Matos, M.N. Mineva, C.J. Pearson, C. Plettner, D. Rudolph, Ch. Scheidenberger, K.-H. Schmidt, V. Shishkin, D. Sohler, K. Summerer, J.J. Valiente-Dobon, P.M. Walker, H. Weick, M. Winkler and O. Yordanov, *Physics Review C*, **69**, 024617 (2004).

[167] Zs. Podolyák, J. Gerl, M. Hellström, F. Becker, K.A. Gladnishki, M. Górska, A. Kelic, Y. Kopatch, S. Mandal, P.H. Regan, K.-H. Schmidt, P.M. Walker, H.-J. Wollersheim, A. Banu, G. Benzoni, H. Boardman, E. Casarejos, J. Ekman, H. Geissel, H. Grawe, D. Hohn, I. Kojouharov, J. Leske, R. Lozeva, M.N. Mineva, G. Neyens, R.D. Page, C.J. Pearson, M. Portillo, D. Rudolph, N. Saito, H. Schaffner, D. Sohler, K. Summerer, J.J. Valiente-Dobon, C. Wheldon, H. Weick and M. Winkler, *Physics Letters B*, **632**, 203 (2006).